

Cosmic evolution of active galactic nuclei detected in the radio waveband

Šlaus, Bruno

Doctoral thesis / Doktorski rad

2023

Degree Grantor / Ustanova koja je dodijelila akademski / stručni stupanj: **University of Zagreb, Faculty of Science / Sveučilište u Zagrebu, Prirodoslovno-matematički fakultet**

Permanent link / Trajna poveznica: <https://um.nsk.hr/um:nbn:hr:217:195629>

Rights / Prava: [In copyright](#) / [Zaštićeno autorskim pravom.](#)

Download date / Datum preuzimanja: **2024-06-29**



Repository / Repozitorij:

[Repository of the Faculty of Science - University of Zagreb](#)





University of Zagreb
Faculty of Science
Department of Physics

Bruno Šlaus

**Cosmic evolution of active galactic nuclei
detected in the radio waveband**

DOCTORAL THESIS

Zagreb, 2023



University of Zagreb
Faculty of Science
Department of Physics

Bruno Šlaus

**Cosmic evolution of active galactic nuclei
detected in the radio waveband**

DOCTORAL THESIS

Supervisors:

prof. dr. sc. Vernesa Smolčić

dr. sc. Vibor Jelić

Zagreb, 2023



Sveučilište u Zagrebu
Prirodoslovno-matematički fakultet
Fizički odsjek

Bruno Šlaus

Kozmička evolucija aktivnih galaktičkih jezgri detektiranih u radiopodručju

DOKTORSKI RAD

Mentori:

prof. dr. sc. Vernesa Smolčić

dr. sc. Vibor Jelić

Zagreb, 2023

Supervisor information

Prof. dr. sc. Vernesa Smolčić is a world-renowned astrophysicist and full professor at the Department of Physics, Faculty of Science, University of Zagreb. Prof. Smolčić did her studies in Croatia, the USA, Germany and Australia, and after nine years of work and training at the leading universities in the world, she returned to Croatia. Her research focuses on the formation and development of galaxies, she studies active galactic nuclei, radio galaxies and extragalactic star formation. She is a member of numerous international collaborations, and in some of them she holds leadership positions, such as in the Cosmic Evolution Survey (COSMOS) and The Ultimate XMM Extragalactic Survey. She has published over 140 scientific papers and received numerous awards for her work, such as the Ernst Patzer Award, Zagreb Woman of the Year 2014, Recognition of the Faculty Council of the Faculty of Science for significant scientific achievement and contribution to the reputation of the Faculty of Science, COSMO Scientist of the Year 2015, State Award for Science for 2017, Award of the Croatian Academy of Sciences and Arts for the highest scientific and artistic achievements in the Republic of Croatia for 2019 in the field of mathematical, physical and chemical sciences, and was included in the list of most successful people of generation 2013 by Forbes magazine. In addition to the prestigious ERC Starting Grant for the project “Constraining Stellar Mass and Supermassive Black Hole Growth through Cosmic Times: Paving the Way for the Next Generation Sky Surveys”, she has led numerous scientific projects.

Dr. sc. Vibor Jelić is a senior research associate and a head of the Laboratory for Astroparticle Physics and Astrophysics (Division of Experimental Physics) at the Ruđer Bošković Institute in Zagreb, Croatia. He is also affiliated with the University of Zagreb as an associate professor in astronomy and astrophysics at the Faculty of Science (Department of Physics). He received his PhD from the University of Groningen in 2010, and subsequently was a postdoctoral researcher at the Netherlands Institute for Radio Astronomy (ASTRON) and the Kapteyn Astronomical Institute, University of Groningen. His scientific interests are understanding the interplay between the interstellar medium and magnetic fields in the Milky Way and detecting the cosmological 21 cm emission from the Cosmic Dawn and the Epoch of Reionization. His re-

search combines radio (polarimetric) observations with numerical simulations and observations at other wavelengths.

Acknowledgements

I thank Vernesa Smolčić for being my mentor during the creation of this thesis. Without her, this work would not have been possible. I thank Vibor Jelić and Željko Ivezić for all the help they provided. I also thank the entire Faculty of physics in Zagreb, and especially Matko Milin, for creating an environment where such work was possible. I thank my family for supporting me during the years it took me to complete this thesis.

Abstract

A major topic in the field of astrophysics is understanding the evolution of the Universe through cosmic time. Throughout the evolution of the Universe and galaxies, among the most interesting objects are galaxies containing active, super-massive black holes in their galactic centers, called active galactic nuclei (AGN). We model the evolution of AGN by constructing their radio luminosity functions. We use radio surveys of varying area and depth, namely the deep COSMOS survey of 1,916 AGN sources, the wide shallow 3CRR, 7C and 6CE surveys, containing together 356 AGNs, and the intermediate XXL-North and South fields consisting of 899 and 1,484 AGN sources, respectively. Together, these surveys constrained the luminosity functions at high redshifts and over a wide range of luminosities (up to $z \approx 3$ and $\log(L_{1.4 \text{ GHz}}/\text{WHz}^{-1}) \in [22, 29]$). We performed the cross-correlation between the XXL-North catalogue, observed at 610 MHz with the Giant Metrewave Radio Telescope (GMRT), and the corresponding multi-wavelength catalogue, via a likelihood ratio method, based on their positions and optical properties. Using solely the 1150 AGN from the XXL-North field we constructed the 1.4 GHz luminosity functions of the sample, using the non-parametric maximum volume method. The full data set was used to model the 1.4 GHz luminosity functions via parametric methods within the Bayesian framework, which allowed us to perform model selection between a set of different models. We show that the luminosity-dependent density evolution (LDDE) model fits the data best. We determine the number density, luminosity density and kinetic luminosity density as a function of redshift, and discuss the evolution of AGN sub-populations, divided by stellar mass. Altogether our results point to a picture where the evolution of AGN depends on luminosity, and require more complex models, either via AGN sub-populations where the total AGN sample is divided into sub-samples, or via luminosity-dependent functions.

Keywords: galaxies, active galactic nuclei, evolution of galaxies, radio continuum observations, luminosity functions, parametric methods of luminosity functions modeling

Prošireni sažetak

Važna tema unutar područja astrofizike je evolucija Svemira kroz kozmičko vrijeme. Od posebnog interesa pritom su galaksije koje u svome središtu sadrže crnu rupu na koju dolazi do akrecije materijala. Takve objekte nazivamo aktivnim galaktičkim jezgrama. Unutar ove disertacije proučava se evolucija aktivnih galaktičkih jezgri konstrukcijom funkcija luminoziteta u radio području spektra. Cjelokupni uzorak na kojemu vršimo analizu dolazi od više različitih studija. Studije su pritom promatrale različite dijelove neba, uz različite površine opažanja i različite dubine opažanja. Pod dubinom opažanja podrazumijeva se osjetljivost promatranja na dolazeću gustoću fluksa. Definicija fluksa u astrofizici je snaga koja dolazi na detektor po jedinici površine detektora. Mjerna jedinica je Wm^{-2} . Flux po jedinici frekvencije, naziva se gustoća fluksa. Kako su dalji objekti generalno manje sjajni, slijedi da osjetljivost određuje do koje dubine, odnosno do kojih crvenih pomaka, studija seže. Pritom se pod crveni pomak podrazumijeva mjera udaljenosti astronomskih objekata parametrizirana preko pomaka u frekvenciji ka crvenome, koja je posljedica ekspanzije Svemira¹. Ukupna snaga koju emitira izvor naziva se luminozitet. Izvori velikog luminoziteta, dolaze pak od studija velike površine opažanja, jer su ti izvori statistički rijetki u Svemiru. Kako su jako luminozitetni izvori sjajni, takve studije mogu imati malenu dubinu. U ovoj tezi koristimo duboko COSMOS istraživanje, koje sadrži 1,916 aktivnih galaktičkih jezgri. Od plitkih polja velike površine koristimo 3CRR, 7C i 6CE istraživanja, koja skupa sadrže 356 aktivnih galaktičkih jezgri. Kako bismo spojili plitka i duboka istraživanja, koristimo još i polja srednje dubine. To su XXL-North i South polja, koja sadrže 899 i 1,484 aktivnih galaktičkih jezgri, respektivno. Zajedno sva istraživanja sadrže stoga uzorak od 4,655 aktivnih galaktičkih jezgri. Ovakav uzorak omogućio nam je da odredimo funkcije luminoziteta na širokom rasponu crvenih pomaka i luminoziteta (do $z \approx 3$ i $\log(L/\text{WHz}^{-1}) \in [22, 29]$).

Ključne riječi: galaksije, aktivne galaktičke jezgre, evolucija galaksija, opažanja u radio području, funkcije luminoziteta, parametarske metode modeliranja funkcija luminoziteta

¹Crveni pomak z definiran je preko emitirane i opažene frekvencije f kao: $1 + z = \frac{f_{\text{emit}}}{f_{\text{op}}}$

Aktivne galaktičke jezgre

Vjeruje se da većina galaksija sadržava u svome centru crnu rupu. Ako pri akreciji materije na centralnu crnu rupu dolazi do zračenja energije, tada govorimo o aktivnim galaktičkim jezgrama. Povijesno, model aktivnih galaktičkih jezgri bio je uveden kao način objašnjavanja velikog broja opservacija vrlo sjajnih kompaktnih objekata. Ukratko, opažanja provedena prošloga stoljeća, dovela su do klasifikacije niza objekata zasebnim imenima, od kojih spominjemo: Tip 1 Seyfert galaksije, Tip 2 Seyfert galaksije, Radio glasne kvazare², Radio tihe kvazare, Blazare, LINER-galaksije³, i tako dalje. Puna tablica klasifikacije može se pronaći u Padovani et al. (2017). Među opažanjima su postojale sličnosti. Prvo, luminozitet ovih izvora bio je velik, te su samim time bili opaženi i na velikim crvenim pomacima. Drugo, zračenje, koje se protezalo duž cijelog elektromagnetskog spektra, dolazilo je iz kompaktnoga područja (\sim mpc). Sličnosti su navele na stvaranje unificiranog modela aktivnih galaktičkih jezgri.

Prvi, jednostavniji, unificirani model aktivnih galaktičkih jezgri pretpostavlja da su sva gore navedena opažanja posljedica jednoga fizikalnoga objekta: aktivne galaktičke jezgre. Morfolologija aktivne galaktičke jezgre pritom je opisana u Slici 1.1. Razlike u opažanjima u ovoj interpretaciji dolaze od razlika u inklinaciji opažanja i luminoziteta samoga izvora. Ovakav jednostavan model bio je nedavno proširen kako bi bolje opisao realnosti opažanja aktivnih galaktičkih jezgri (Heckman & Best 2014). Naime uočeno je da neki izvori posjeduju radio mlazove a neki ne, te nadalje da postoji evolucija aktivnih galaktičkih jezgri kroz kozmičko vrijeme. Novi model pretpostavlja bimodalnost aktivnih galaktičkih jezgri na radijativno efikasne i radijativno ne-efikasne aktivne galaktičke jezgre. Razlika među ovim sub-kategorijama dolazi od razlike u akreciji materijala na centralnu crnu rupu. Radijativno efikasne jezgre vrše akreciju hladne materije putem akrecijskoga diska, dok ne-efikasne jezgre vrše akreciju putem geometrijski širokog, ali optički prozirnog upada materije.

Aktivne galaktičke jezgre vezane su za cjelokupnu galaksiju u kojoj se nalaze putem procesa povratne sprege. Ukratko, pri upadu materijala na centralnu crnu rupu, dolazi do oslobađanja energije, bilo putem radijacije, ili mehanički putem radio mlazova. To dovodi do toga da plin prisutan u galaksiji biva otpuhan van galaksije ili u krajnjem slučaju da taj plin nije u stanju ohladiti se. Efektivno time biva smanjen materijal koji upada u centralnu crnu rupu, i istovremeno biva smanjen materijal potreban za stvaranje zvijezda u galaksiji. Efekt povratne sprege stoga dovodi da stvaranje zvijezdi u galaksiji i porast mase centralne crne rupe biva usporen ili potpuno zaustavljen (e.g. Harrison 2017). Iako detalji povratne sprege bivaju diskutirani u struci, njihovo postojanje je uvelike prihvaćeno. Dokazi mogu biti indirektni putem korelacija

²Od engleskoga quasi-stellar object (QSO).

³Od engleskoga low-ionization nuclear emission-line region.

između mase centralne crne rupe i svojstva galaksije (e.g. Magorrian et al. 1998) ili direktno opaženi, poput galaktičkih vjetrova (e.g. Tombesi et al. 2015). Nadalje, povratna sprega koristi se u simulacijama evolucije galaksija.

Evolucija galaksija opisuje se unutar hijerarhijskog modela. Nakon stvaranje prvih galaksija one rastu putem unosa materijala i međusobnog stapanja. Stapanje galaksija dovodi pritom i do rasta centralne crne rupe. Ovako postavljena evolucija galaksija na prvi pogled biva u srazu s opažanjima koja pokazuju da su masivnije crne rupe nastale ranije od manje masivnih. Prividni sraz objašnjava se upravo povratnom spregom aktivne galaktičke jezgre. Naime, kako galaksija prima materijal koji hrani centralnu crnu rupu, tako dolazi do faze aktivnosti galaktičke jezgre. Materijal biva otpuhan iz galaksije te ona iz plave galaksije koja stvara zvijezde, prelazi u crvenu galaksiju koja je većinom mirna. Pritom staje i rast crne rupe. Ovako postavljena fizikalna slika vodi nas do činjenice da aktivne galaktičke jezgre evoluiraju kroz kozmičko vrijeme te da, nadalje, dvije sub-kategorije aktivnih galaktičkih jezgri, radijativno efikasne i ne-efikasne jezgre, mogu biti shvaćene kao dva evolucijska stadija aktivnih galaktičkih jezgri. Radijativno efikasne jezgre pritom se nalaze u plavim galaksijama, a radijativno ne-efikasne u crvenim.

Evolucija aktivnih galaktičkih jezgri opaženih u radio području proučavana je u literaturi (e.g. Willott et al. 2001, Smolčić et al. 2009). Koncentrirajući se na fizikalnu sliku, pronađena je razlika u evoluciji aktivnih galaktičkih jezgri koja ovisi o njihovom luminozitetu. Ovi rezultati su konzistentni sa slikom aktivnih galaktičkih jezgri koje podrazumijevaju njihovu bimodalnost. Visoko luminozitetni izvori odgovarali bi pritom radijativno efikasnim jezgrama, a nisko luminozitetni izvori ne-efikasnim. U ovome radu bavimo se proučavanjem evolucije aktivnih galaktičkih jezgri. Evoluciju istražujemo putem konstrukcije funkcija luminoziteta, koje prikazuju raspodjelu prostorne gustoće izvora po luminozitetu, za određeni crveni pomak. Funkcije određujemo parametarskim metodama, čime smo u stanju odrediti analitički model promjene gustoće aktivnih galaktičkih jezgri kroz kozmičko vrijeme.

Funkcije luminoziteta XXL-North polja

Posebna pažnja bila je posvećena podacima koji dolaze iz XXL-North polja. Pritom je spajanje radio kataloga s katalogom crvenih pomaka provedeno unutar ovog rada putem metode koja uzima u obzir i poziciju i magnitudu izvora. Radio podaci dolaze od opažanja putem "Giant Metrewave Radio Telescope" teleskopa, te su provedeni na 610 MHz. Ukupni radio katalog podijeljen je na dva dijela radi razlika u opažanjima. Unutarnji dio polja postigao je dubinu od $200 \mu\text{Jy beam}^{-1}$, a vanjski $45 \mu\text{Jy beam}^{-1}$. Izvori su određeni putem "Source Peeling and Atmospheric Modeling (SPAM)" programa (Intema et al. 2017). Spektralni izvori određeni su

putem "NRAO Very Large Array Sky Survey" istraživanja. Ukupni katalog sadržavao je 5434 izvora. Crveni pomaci dolaze iz kataloga opaženog na raznim valnim duljinama (Fotopoulou et al. 2016). Kako bismo koristili polje uniformne dubine i gustoće uzeli smo podskup izvora opažen Spitzer IRAC Channel 1 kamerom, na 3.6. μm .

Pri spajanju kataloga pažnja je prvo posvećena eliminiranju astrometrijskog pomaka između dva kataloga, te pronalasku izvora od više komponenti. Izvori od više komponenti odnose se na pojedine izvore, krivo upisane u katalog kao više izvora, radi prostorno proširene radio emisije i kompleksnije morfologije (npr. izvori koji posjeduju radio mlazove). Ovi izvori spojeni su ručno u jedinstvene izvore korištenjem "Multi-Catalog Visual Cross-Matching (MCVCM)" programskog paketa. Spajanje kataloga provedeno je putem metode vjerojatnosti opisane u Ciliegi et al. (2018). Ukratko, pripadne identifikacije radio izvora unutar kataloga crvenih pomaka, određene su putem njihove pozicije i putem njihove magnitude. Ova metoda rezultirala je identifikacijom 2467 izvora.

Prvi rezultati vezani uz evoluciju radio opaženih aktivnih galaktičkih jezgri, dobiveni su korištenjem zasebno XXL-North podataka. Funkcije luminoziteta konstruirane su ne-parametarskom metodom maksimalnih volumena (Schmidt 1968). Pritom smo prvo odredili podskup izvora koji odgovaraju aktivnim galaktičkim jezgrama, te kvantificirali korekcije koje su nužne kako bi se ispravile greške koje dolaze od šuma u opažanju i od gubitka izvora pri spajanju kataloga, čime je u uzorku preostalo 1150 izvora. Rezultirajuće funkcije luminoziteta prikazane su na Slici 4.4. Usporedba s funkcijama luminoziteta iz literature i modelom iz Willott et al. (2001), vodi na činjenicu da su naše funkcije luminoziteta konzistentne s fizikalnom slikom koja pretpostavlja bimodalnost aktivnih galaktičkih jezgri. Drugim riječima, evolucija je ovisila o luminozitetu, gdje je visoko luminozitetni dio uzorka evoluirao brže.

Funkcije luminoziteta kompozitnog polja

Evolucija aktivnih galaktičkih jezgri proučavana je dalje korištenjem cijeloga kompozitnoga polja, sačinjenog od COSMOS, XXL-North i South the 3CRR, 6CE i 7C polja. Detalji polja važni za kreaciju funkcija luminoziteta dani su u Tablici 1. Modeliranje funkcija luminoziteta provedeno je parametarskom metodom unutar Bayes-ovog formalizma. Primjena ove metode na određivanje funkcija luminoziteta može se pronaći u Marshall et al. (1983). Ukratko, pretpostavljajući razne oblike analitičkih funkcija luminoziteta, bili smo u stanju odrediti raspodjele vjerojatnosti parametara modela. Pored toga, ova metoda daje nam mogućnost usporedbe među modelima čime smo bili u stanju odrediti model koji najbolje opisuje evoluciju radio opaženih aktivnih galaktičkih jezgri. Usporedba modela provedena je usporedbom marginalnih

Tablica 1: Polja korištena za određivanje funkcija luminoziteta. Broj izvora i srednji spektralni indeksi se odnose na podskup aktivnih galaktičkih jezgri.

| Polje | Površina [deg ²] | Frekvencija opažanja [MHz] | Dubina na 1400 MHz [mJy beam ⁻¹] | Broj iz- vora | Srednji spek- tralni indeks |
|-------------------|---------------------------------|----------------------------------|--|------------------|--------------------------------|
| 7C | 72.22 | 151 | 105 | 128 | -0.64 ± 0.27 |
| 6CE | 338.13 | 151 | 421 | 58 | -0.51 ± 0.32 |
| 3CRR | 13886.3 | 178 | 2,609 | 170 | -0.67 ± 0.24 |
| XXL-North (Inner) | 6.3 | 610 | 1.0 | 292 | -0.42 ± 0.49 |
| XXL-North (Outer) | 14.2 | 610 | 1.0 | 607 | -0.48 ± 0.57 |
| XXL-South | 25 | 2100 | 1.0 | 1484 | -0.63 ± 0.37 |
| COSMOS | 2 | 3000 | 1.15 · 10 ⁻² | 1916 | -0.80 ± 0.44 |

vjerojatnosti te aproksimativnim metodama "Akaike information criterion (AIC)" i "Bayesian information criterion (BIC)".

Prije korištenja metodologije na pravim podacima, testirali smo ih na simuliranim podacima. Pritom su katalogi simuliranih podataka stvoreni krećući od pretpostavljenog oblika funkcije luminoziteta. Sposobnost metodologije da re-kreira početnu funkciju luminoziteta davala je uvid u robusnost metoda. Testovi su provedeni na većem broju simuliranih kataloga, uz razne pretpostavljene funkcije luminoziteta. Rezultati su uvijek bili zadovoljavajući. Primjer testiranja metode dan je na Slikama 5.2 i 5.3. Slike prikazuju funkcije luminoziteta i pripadne raspodjele vjerojatnosti parametara za testirani model.

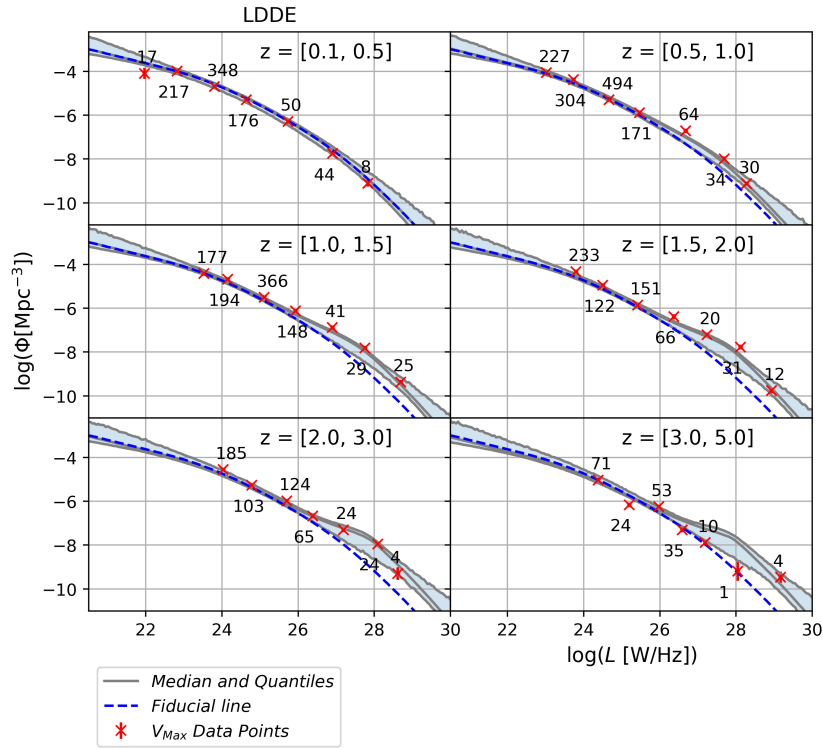
Metodologija je potom provedena na pravim podacima. Pritom je testiran veći broj modela funkcija luminoziteta, prikazan u Tablici 5.1. Sve metode usporedbe među modelima vodile su na to da je najbolji model onaj koji pretpostavlja da evolucija aktivnih galaktičkih jezgri ovisi o luminozitetu (takozvani "Luminosity-dependent density evolution", odnosno LDDE, model). Model je definiran kao (Fotopoulou et al. 2016):

$$\Phi(L, z) = \Phi_0 \times \frac{(1+z_c)^{p_1} + (1+z_c)^{p_2}}{\left(\frac{1+z_c}{1+z}\right)^{p_1} + \left(\frac{1+z_c}{1+z}\right)^{p_2}} \quad (1)$$

gdje vrijedi:

$$z_c = \begin{cases} z_c^* & , L > L_a \\ z_c^* \cdot \left(\frac{L}{L_a}\right)^a & , L \leq L_a \end{cases} \quad (2)$$

Pritom je L_a luminozitet na kojem dolazi do promjene u evoluciji, a z_c crveni pomak pri kojem se evolucija mijenja. Parametri $p_{1,2}$ određuju evoluciju. Rezultirajuće raspodjele parametara



Slika 1: Rezultirajuće funkcije luminoziteta uz pretpostavku LDDE modela. Sive linije predstavljaju median i 90% kvantile, izračunate biranjem 5000 nasumičnih uzoraka iz raspodjele vjerojatnosti parametara. Crvene točke predstavljaju ne-parametarsku metodu maksimalnih volumena. Plava crtkana linija predstavlja lokalnu funkciju luminoziteta danu kao usporedbu za više crvene pomake.

moгу se vidjeti u Tablici 6.7 i Slici 6.7. Funkcije luminoziteta prikazujemo i na Slici 1.

Fizikalna interpretacija

LDDE model funkcije luminoziteta imao je posljedice na fizikalnu sliku aktivnih galaktičkih jezgri. Model je smatran dobro određen na crvenim pomacima do $z \approx 3$ i luminozitetima $\log(L/\text{WHz}^{-1}) \in [22, 29]$. Proučili smo gustoću izvora te luminozitetnu gustoću izvora kao funkciju crvenog pomaka. Rezultati su dani na Slikama 7.1 i 7.2. Ukratko, radi korištenja LDDE modela, dolazi do zaravnavanja ovih funkcija koje nije prisutno pri korištenju jednostavnijih modela. Odredili smo nadalje gustoću kinetičkog luminoziteta, veličine koja određuje količinu energije koja se mehanički prenese okolini putem radio mlazova. Slika ove funkcije i usporedbe s modelima dana je na Slici 7.3. Također, kako bismo testirali ovisnost evolucije o

zvjezdanoj masi galaksija, podijelili smo uzorak na podskupove po zvjezdanoj masi. Pronađena je razlika u evoluciji među podskupovima.

Sveukupno, rezultati se daju interpretirati unutar cjelokupne fizikalne slike evolucije aktivnih galaktičkih jezgri i samih galaksija. Kao što smo naveli, evolucija galaksija opisana je hijerarhijskim modelom, gdje galaksije evoluiraju međusobnim stapanjem. Činjenica da veće crne rupe nastaju ranije objašnjava se procesom povratne sprege između galaktičke jezgre i same galaksije. Pri upadu materijala na centralnu crnu rupu dolazi do otpuhivanja plina iz galaksije čime se zaustavlja rast crne rupe i formacija zvijezda. Galaksija prelazi iz plave u crvenu "mrtvu" galaksiju. Ovako opisana fizikalna slika podrazumijeva da fizika aktivnih galaktičkih jezgri ovisi o luminozitetu. Naš model evolucije u skladu je stoga s ovako postavljenom slikom. Također, iz činjenice što su jednostavniji modeli evolucije koji pretpostavljaju konstantu promjenu u broju ili luminozitetu izvora, odbačeni unutar ovoga rada, slijedi da je fizika akrecije materije na crnu rupu kompleksan proces koji zahtjeva kompliciranije modele.

Nadalje, iako naš LDDE model podrazumijeva kontinuiranu razliku u evoluciji kao funkciju luminoziteta, to ne isključuje mogućnost sub-populacija aktivnih galaktičkih jezgri. Naime, ako se sub-populacije biraju na bilo koji drugi način osim prema luminozitetu, slijedi da različiti omjeri tih populacija mogu biti na različitim luminozitetima. Kontinuirano mijenjanje evolucije u ovisnosti o luminozitetu bi tada slijedilo kao prirodna posljedica. Sveukupno, model aktivnih galaktičkih jezgri koji podrazumijeva bimodalnost između radijativno efikasnih i ne-efikasnih jezgri, i dalje je konzistentan s našim rezultatima.

Sve u svemu, naši rezultati spadaju u širi trend u literaturi koji nalazi razliku u evoluciji aktivnih galaktičkih jezgri kao funkcije luminoziteta (e.g. Smolčić et al. 2009, Willott et al. 2001, Rigby et al. 2015). Oni spadaju, također, među rezultate koji pronalaze potrebu za povratnom spregom između aktivne galaktičke jezgre i same galaksije, bilo direktnim opažanjima (e.g. Tombesi et al. 2015) ili teorijski, putem modela.

Contents

| | | |
|----------|--|-----------|
| 1 | Introduction | 1 |
| 1.1 | Unified model of AGN | 1 |
| 1.2 | AGN Bimodality | 4 |
| 1.3 | AGN Feedback | 6 |
| 1.4 | Luminosity functions | 11 |
| 1.5 | Evolutionary trends in radio-detected AGNs | 13 |
| 1.6 | Hierarchical model and downsizing | 14 |
| 1.7 | Radio emission of galaxies | 15 |
| 1.7.1 | Blackbody radiation | 16 |
| 1.7.2 | Free-free emission | 16 |
| 1.7.3 | Synchrotron emission | 17 |
| 1.7.4 | Complete spectrum | 18 |
| 1.8 | Thesis outline | 19 |
| 2 | Data | 22 |
| 2.1 | 3CRR, 7C and 6CE fields | 23 |
| 2.2 | COSMOS field | 24 |
| 2.3 | XXL-South field | 25 |
| 2.4 | XXL-North field | 25 |
| 2.5 | AGN subsamples | 26 |
| 2.6 | Composite survey | 27 |
| 3 | XXL-North multiwavelength source matching | 29 |
| 3.1 | Radio data | 29 |
| 3.2 | Multi-wavelength data | 30 |
| 3.3 | Astrometric correction | 31 |
| 3.4 | Multi component sources | 34 |
| 3.5 | Likelihood ratio cross-correlation | 34 |
| 3.5.1 | Deriving $f(r)$ | 36 |
| 3.5.2 | Deriving $n(m)$ | 37 |
| 3.5.3 | Deriving $q(m)$ | 37 |
| 3.6 | The blocking effect | 38 |
| 3.7 | Results of the cross-correlation | 41 |

| | | |
|----------|--|-----------|
| 4 | XXL-North LFs | 42 |
| 4.1 | Missing counterparts | 42 |
| 4.2 | AGN sample | 43 |
| 4.3 | XXL-North LFs creation | 46 |
| 4.4 | Corrections | 47 |
| 4.5 | Bin selection | 48 |
| 4.6 | LFs of the XXL-North field | 48 |
| 4.7 | Comparison with the literature | 49 |
| 4.8 | Physical interpretation of the XXL-North LFs | 52 |
| 5 | Bayesian LF modeling | 54 |
| 5.1 | Bayesian modeling of LFs | 54 |
| 5.2 | Likelihood function | 55 |
| 5.3 | Model comparison within the Bayesian framework | 56 |
| 5.4 | LF models | 58 |
| 5.4.1 | Local LF | 58 |
| 5.4.2 | LF evolution | 59 |
| 5.4.3 | Bimodal evolution model | 60 |
| 5.5 | Maximum volumes on composite fields | 61 |
| 5.6 | Results on simulated data sets | 61 |
| 6 | Luminosity functions of the composite survey | 65 |
| 6.1 | Model comparison | 65 |
| 6.2 | Non-optimal LF models | 66 |
| 6.2.1 | Pure density evolution | 67 |
| 6.2.2 | Pure luminosity evolution | 67 |
| 6.2.3 | PDE and PLE mixture | 67 |
| 6.2.4 | Redshift dependent evolution | 68 |
| 6.2.5 | Bimodal evolution | 69 |
| 6.3 | Luminosity-dependent evolution | 71 |
| 6.4 | Additional checks | 73 |
| 6.5 | Comparison with the literature | 76 |
| 6.6 | Non-parametric LFs | 77 |
| 7 | Discussion | 80 |
| 7.1 | Number and luminosity density | 80 |
| 7.2 | Kinetic luminosity | 82 |
| 7.3 | Source counts | 85 |
| 7.4 | Stellar mass dependent difference in evolution | 88 |
| 7.5 | Evolution of AGN sub-populations in the literature | 89 |
| 7.6 | LDDE model within the picture of AGN bimodality | 91 |
| 7.7 | LDDE model, Downsizing and Feedback | 92 |

| | |
|--|------------|
| 8 Thesis summary and outlook | 94 |
| 8.1 Summary of this Thesis | 94 |
| 8.1.1 XXL-North LFs | 94 |
| 8.1.2 Composite field LFs | 95 |
| 8.1.3 Implications of the LDDE model | 95 |
| 8.1.4 Outlook | 96 |
| References | 97 |
| Curriculum vitae | 104 |

List of Figures

| | | |
|-----|---|----|
| 1 | Rezultirajuće funkcije luminoziteta uz pretpostavku LDDE modela. Sive linije predstavljaju median i 90% kvantile, izračunate biranjem 5000 nasumičnih uzoraka iz raspodjele vjerojatnosti parametara. Crvene točke predstavljaju ne-parametarsku metodu maksimalnih volumena. Plava crtkana linija predstavlja lokalnu funkciju luminoziteta danu kao usporedbu za više crvene pomake. . . . | vi |
| 1.1 | The unified model of AGN. The morphology of the model, described in detail in the text, is denoted in the figure. Here SMBH stands for supermassive black hole, while BLR and NLR denote the broad and narrow line regions respectively. The way the morphology influences the observations is also denoted in the figure, showing how the inclination changes what the observer would see. The figure also shows the AGN dichotomy between radio loud and quiet AGN, but this already leads to AGN bimodality, described in the next section. Modified from Urry & Padovani (1995). | 3 |
| 1.2 | The schematic representation of AGN bimodality. The two types of AGN are shown in the figure. Left is the radiative mode AGN. The morphology of these objects follows the morphology of the simpler AGN unified model found in Fig. 1.1. In red it is also denoted how different inclinations of observations result in inner parts of AGNs being or not being obscured. On the right the radiatively inefficient AGN is shown. The accretion occurs via geometrically thick accretion flow, as described in the text. Taken from Heckman & Best (2014). | 6 |
| 1.3 | The graph detailing the evolution of galaxies. The complete sample of galaxies, given in gray, are plotted in the graph showing their stellar mass vs specific star formation rate (sSFR), or star formation rate divided by stellar mass. The green lines represent the growth of blue galaxies and their quenching. The quenching moves them from the star-forming main sequence of the graph (blue galaxies), towards the red sequence (red galaxies). The contours denote the AGN volume densities. The blue contours correspond to luminous AGN selected via bolometric luminosity, or roughly the radiative mode AGNs, while the red contours correspond to less luminous AGN, or the jet mode AGN. The graph shows that different type of AGN are hosted in different types of galaxies. Taken from Heckman & Best (2014). | 7 |

- 1.4 A schematic picture showing the effect of AGN feedback on galactic gas reservoir and the effect on star formation and black hole growth. The arrows denote the way certain processes affect the available fuel. It is important to notice the crossed grey and back arrows denoting that there exist an interplay between the AGN and the host galaxy. The lowest part of the figure sketch how these effects impact the mass of the black hole and the stellar mass of the host galaxy. Taken from Harrison (2017). 9
- 1.5 The current state of AGN discussion presented schematically. On the left is pictured the current picture about the shape and scale of AGN outflows. The middle part of the figure shows the effects of the feedback on star formation, both positive and negative, and the powering mechanisms. On the right is the way that the outflows affect different phases of galaxy gas. Taken from Husemann & Harrison (2018). 10
- 1.6 The star formation estimates compiled by Hopkins (2004) and Bouwens et al. (2012) given via orange and blue data points, compared to the black hole accretion rate, multiplied by 5000 for comparison. Taken from Kormendy & Ho (2013). 11
- 1.7 A typical Schechter function and the two main modes of LF evolution. The x-axis shows magnitude, which is proportional to log-luminosity. In the left a LF with no evolution is shown in red. The part of the LF corresponding to a power-law slope and exponential cut-off are denoted via text in the figure. The magnitude of the "knee" is denoted as M^* , while α denotes the faint-end slope steepness. The middle panel of the figure shows the evolution in luminosity (PLE model) as a function of redshift $E(z)$. The red line denotes the local LF, Φ_0 , while the black dashed lines denote the evolved LF for both positive and negative evolution. The panel on the right is the same as the middle panel but for evolution in density (PDE model). Factors β and γ are the evolution parameters, taken here to be constants. The evolution of LF in the figure depends on redshift, but the plots would look qualitatively identical for constant evolution. Taken from Johnston (2011a). 12
- 1.8 Spectrum of a population of electrons arising from a superposition of individual spectra. Spectrum of a single electron is pictured in the upper right corner of the figure (notice the log-scale). Taken from Carroll & Ostlie (2014). 19
- 1.9 The radio and infrared part of the spectrum of M82, a starburst galaxy. The horizontal dashed line denotes the free-free emission. The dot-dashed line at low frequencies denotes the synchrotron radiation. The dotted line at higher frequencies corresponds to the thermal emission from dust. Together they form the radio spectrum of the galaxy (full line). The figure shows the emission from theory as well as real observational data. Taken from Condon & Ransom (2016) 20

| | | |
|-----|---|----|
| 2.1 | The areas and detection limits of the fields used in this work, which together form the composite survey. The detection limits were shifted to a frequency of 1.4 GHz for easier comparison, assuming a power law radio spectrum. The detection limits of the XXL-North and South surveys correspond to the pure AGN sample selected via a threshold in flux, as described in Sect. 2.5. | 23 |
| 2.2 | The redshift-luminosity plot of the complete composite sample, of radio AGNs used in this work. The names of the fields are denoted in the legend. | 28 |
| 3.1 | Overlap of Spitzer IRAC 3.6 μm coverage with the the XXL-North field. The gray map corresponds to the GMRT 610 MHz mosaic, while the red region denotes the area covered by IRAC data. The sources in the radio catalogue are denoted by green circles and black crosses. Sources marked by green symbols correspond to the noisy edges, removed from further consideration, as described in the text. Note that the Spitzer IRAC 3.6 μm data do not cover the northern part of the central XXL-North field. However, the number of radio sources there is lower. | 31 |
| 3.2 | Comparison between the spectroscopic (z_{spec}) and the photometric (z_{phot}) redshifts for 528 sources with good quality spectra. For the definition of accuracy σ and the percentage of catastrophic outliers η , see the text. The bottom panel shows the renormalized accuracy, defined as denoted on the y-axis of the bottom panel. The solid red line shows the one-to-one relationship, while the dashed and dotted lines correspond to $z_{\text{phot}} = 0.05 \cdot (1 + z_{\text{spec}})$ and $z_{\text{phot}} = 0.15 \cdot (1 + z_{\text{spec}})$, respectively. | 32 |
| 3.3 | Positional offsets between the GMRT and IRAC surveys for the outer part of the XXL-North field. The mean offset is denoted by a red star. The histograms in the bottom panels represent the distribution of offsets in the <i>RA</i> and <i>DEC</i> directions. The inner part of the XXL-North field produces a similar plot. The mean offsets for the two parts of the field are given in relations 3.1- 3.4. | 33 |
| 3.4 | Example of a multi-component source inspected visually via the MCVCM program. The radio contours, chosen as $2^n \times \text{RMS}$, $n = 1, 2, 3, \dots$, are overlaid on top of the IRAC image. The radio lobes and cores and the IRAC counterpart are selected manually. The dark green rhomboid denotes the radio core position, and the light green squares denote the center of the radio lobes. The black crosshair denotes the IRAC counterpart. | 35 |
| 3.5 | Magnitude distribution of sources during the cross-correlation. The black, blue, and red lines denote the total, background, and real sources, respectively, as described in the text. The two upper histograms (panels <i>a</i> and <i>b</i> , for the inner and outer part of the field, respectively) correspond to the match where the blocking effect is present. Correction for blocking effects mitigates the issue of negative counts. The two bottom histograms (panels <i>c</i> and <i>d</i> , for the inner and outer part of the field, respectively) are the magnitude distributions after the blocking effect has been accounted for. | 39 |

| | | |
|-----|---|----|
| 3.6 | Visual representation of the blocking effect. The red circle represents the radius around the bright counterpart source (denoted as a white blob) used for calculating $total(m)$. The background sources are represented by stars. The yellow stars are detected, while the blue remain undetected due to being blocked by the bright source. The $total(m)$ magnitude distribution is therefore underestimated, as described in the text. Taken from Ciliegi et al. (2018). | 40 |
| 4.1 | Upper panel: Redshift histograms of the COSMOS2015 catalogue with only the radio cut (dashed gray line) and the histogram with an additional cut in the infrared flux corresponding to the IRAC detection limit of our survey (black line). Bottom panel: Ratio of these two histograms and the corresponding standard deviation. A cubic interpolation has been performed on both the data points and the error bars. | 44 |
| 4.2 | Top panel: Euclidean-normalized and completeness-corrected source counts for different galaxy populations at 1.4 GHz reproduced from Smolčić et al. (2017), as described in the text. Symbols are indicated in the legend. The vertical gray lines correspond to the 7σ detection limits of the inner and outer part of the XXL-North GMRT survey recalculated from 610 MHz by presuming a power law for the radio emission and a spectral index of -0.7 . Middle panel: Fraction of the radio-excess population. Lower panel: Cumulative fraction of the radio-excess population summed from higher fluxes towards lower. The red dot-dashed line denotes the adopted flux threshold described in the text. | 45 |
| 4.3 | Visual representation of the bins used in the creation of the LFs. The gray dots represent the sources. The black lines correspond to the bin limits in redshift and luminosity. The absence of low-luminosity bins with only few sources is clearly visible. On the high-luminosity end the number of sources per bin decreases, but this effect is a consequence of the intrinsic lower density of high-luminosity sources and cannot be easily corrected. | 49 |
| 4.4 | LFs of this work along with previous ones at 1.4 GHz, as denoted in the legend. The dashed lines represent the bimodal model discussed in the text. This model consists of a high- and a low-luminosity end with different functional dependencies. It can be seen that at higher luminosities, the high-luminosity end of the model traces the data points well. | 50 |
| 5.1 | Schematic representation of the division of the $L - z$ space into sub-spaces as described in the text. The black lines denote the cells $dzdL$, while the red dashed line represents the detection limit of the survey. | 57 |
| 5.2 | LFs created from a simulated catalogue. The green dashed line denotes the starting LF, while the grey lines denote the re-estimated LFs median and 90% quantiles. The Red crosses denote the non-parametric method of maximum volumes. | 63 |

| | | |
|-----|---|----|
| 5.3 | Corner plot showing the posterior distributions of the model parameters in blue. The black lines denote the assumed values used to create the starting LF from which the simulated data set was created. The numbers above the probabilities, denoting the retrieved parameter values are also given in Tab. 5.2. | 64 |
| 6.1 | The PDE model of evolution (relation 5.15), using a Schechter local LF (5.14), modeled using the COSMOS, XXL, 3CRR, 7C and 6CE surveys, obtained by two complementary methods: Bayesian modeling and the method of maximum volumes. Grey lines denote the median and 90% quantiles of the parametric Bayesian inference. The crosses denote the non-parametric method of maximum volumes, together with the corresponding error-bars. The uncertainties were derived assuming a Poisson errors. The blue dashed fiducial line denotes the LF determined in the first redshift bin. | 68 |
| 6.2 | The PLE model of evolution (relation 5.16), using a Schechter local LF (5.14), modeled using the COSMOS, XXL, 3CRR, 7C and 6CE surveys. The notation follows Fig. 6.1. | 70 |
| 6.3 | The Sad02 model of evolution (relation 5.17), using a Schechter local LF (5.14), modeled using the COSMOS, XXL, 3CRR, 7C and 6CE surveys. The notation follows Fig. 6.1. | 71 |
| 6.4 | The evolution model from Novak et al. (2017) (relation 5.18), using a Schechter local LF (relation 5.14), modeled using the COSMOS, XXL, 3CRR, 7C and 6CE surveys. The notation follows Fig. 6.1. | 72 |
| 6.5 | The evolution model from Willott et al. (2001), using the corresponding local LF (relations 5.21 - 5.23), modeled using the COSMOS, XXL, 3CRR, 7C and 6CE surveys. The notation follows Fig. 6.1. | 73 |
| 6.6 | The LDDE model of evolution (relation 5.19) using a Schechter local LF (relation 5.14), modeled using the COSMOS, XXL, 3CRR, 7C and 6CE surveys, obtained by two complementary methods: Bayesian modeling and the method of maximum volumes. Grey lines denote the median and 90% quantiles of the parametric Bayesian inference. These values were obtained by randomly drawing samples from the posterior. The crosses denote the non-parametric method of maximum volumes, together with the corresponding error-bars. The uncertainties were derived assuming Poisson errors. We also show the number of sources creating each data-point. The blue dashed fiducial line denotes the LF determined in the first redshift bin. | 74 |
| 6.7 | The Corner-plot showing the posterior distribution of each parameter of the LDDE model. The resulting samples and weights taken from the posterior were further smoothed as described in Speagle (2020) to obtain the plotted probability density functions. | 75 |
| 6.8 | Comparison of our LDDE model with the models from literature for PDE and PLE evolution models, as denoted above the figures. The used surveys are denoted in the legend. The results of this work, represented by 90% quantiles are given in pink. The Willott LF shown is the one derived by Willott et al. (2001). | 78 |

- 6.9 The non-parametric LFs determined in different redshift bins via method of maximum volumes, as described in the text (Sect. 5.5), shown overlaid on top of each other, in order to display their evolution. The evolution is stronger for high luminosity sources. The last redshift bin is created using a smaller subsample of sources and is, as described in the text, less credible. 79
- 7.1 *Upper left panel:* Number density calculated at 1.4 GHz, for a set of different luminosity ranges of same width, as denoted in the legend above the figure. The black dots represent the maximum value of each line. *Upper right panel:* Number density at 1.4 GHz calculated for a set of progressively increasing luminosity ranges, as denoted in the legend above the figure. *Lower panel:* Number density at 1.4 GHz as a function of redshift for a set of different surveys, denoted in the legend. The data-points denote the high-redshift quasar surveys as described in the text. The uncertainties in this work are calculated from the resulting samples within the parametric Bayesian method as 90% quantiles. The uncertainties of the literature values are determined as maximum uncertainties obtained by shifting the LF parameters, as described in the text. The shaded area in the plots denote higher redshifts, where the LF models are less constrained. The high-redshift quasar density from Gloude-mans et al. (2021) is a lower limit as the luminosity range of the LF used in the calculation was smaller. 83
- 7.2 *Upper left panel:* Luminosity density at 1.4 GHz calculated for a set of different luminosity ranges of same width, as denoted in the legend above the figure. The black dots represent the maximum value of each line. *Upper right panel:* Luminosity density at 1.4 GHz calculated for a set of progressively increasing luminosity ranges, as denoted in the legend above the figure. *Lower panel:* Luminosity density at 1.4 GHz as a function of redshift for a set of different surveys, denoted in the legend. The data-points denote the high-redshift quasar surveys as described in the text. The uncertainties in the figure follow those in Fig. 7.1. The shaded area in the plots denote higher redshifts, where the LF models are less constrained. 84
- 7.3 Kinetic luminosity density as a function of redshift given in grey. The uncertainties are calculated from the resulting samples of the parametric method as 90% quantiles. Black red and blue lines correspond to the predictions from GALFORM. The black line is the total density, while the red and blue lines denote the hot-halo and starburst modes, respectively. The orange dashed line represents the SAGE model. 86

- 7.4 The source counts model together with data points obtained directly from the catalogues. The green dashed line denotes the model obtained from LFs constrained within this work. The errors were determined by selecting 500 samples from the posterior. The red, blue and black lines denote models from Novak et al. (2018) obtained from LFs for AGN, SFG and the total population respectively. Data-points represent the source counts obtained from the catalogues as denoted in the legend. All the catalogues are the same as described in Sect. 2.6 except the ones denoted as Vernstrom+14, which were taken from another study by Vernstrom et al. (2014). COSMOS SFG are sources from the COSMOS catalogue not selected by the radio excess threshold described in Sect. 2.6. The outlier data points are the effect of finite detection limits. 87
- 7.5 The calibration of mass-to-light correlation between the absolute K-band magnitude and stellar mass obtained from the COSMOS2015 catalogue for the subset of AGN sources. The assumed functional form of the correlation is $M^* = a(z)K + b(z)$ as described in the text. *Bottom*: The dependence of stellar mass M^* on K-band magnitude. The blue line shows the linear regression fit performed for each redshift bin independently. The range of each redshift bin is given above the corresponding plot, as well as the resulting correlation parameters. *Top*: The resulting correlation parameters as a function of redshift. The red line shows the linear regression performed on these values in order to determine the redshift dependence of the parameters. 90
- 7.6 LFs for the high and low mass sub-sample. The uncertainty plotted in the figure is the 68.2 quantile. The model of evolution is the PDE model. The redshift of each subplot is given in the figure. 90

List of Tables

| | | |
|-----|--|----|
| 1 | Polja korištena za određivanje funkcija luminoziteta. Broj izvora i srednji spektralni indeksi se odnose na podskup aktivnih galaktičkih jezgri. | v |
| 1.1 | The AGN types determined via observational characteristics. Modified from Carroll & Ostlie (2014). | 2 |
| 2.1 | The surveys used in the estimation of the LFs. | 28 |
| 4.1 | Number of sources, and corresponding area, after each step performed during the analysis and LF creation, as described in the text. The steps are performed progressively, or in other words, each step also includes the previous ones. . . | 46 |
| 5.1 | LF models used in this work, corresponding list of free parameters, and their number N_{Par} | 58 |
| 5.2 | Assumed and retrieved parameters resulting from the modeling of LFs on simulated data. As described in the text, a mock catalogue was created using assumed LF models. This catalogue was then used to model the LFs in order to test the validity of the modeling methodology. | 62 |
| 6.1 | Comparison of the best-fitting LDDE model with other models using three different methods, comparing their marginal likelihoods, and the approximate AIC and BIC methods, as described in the text. The difference in log-marginal-likelihoods is multiplied by two for easier comparison. | 66 |
| 6.2 | Parameters of the PDE model. The standard deviation, provided by the Dynesty package, is asymmetric. These numbers represent the mean values and deviations determined from the posterior distribution. | 67 |
| 6.3 | Parameters of the PLE model. The mean values and deviations were determined from the posterior distribution. | 69 |
| 6.4 | Parameters of the Sadler+02 model. The mean values and deviations were determined from the posterior distribution. | 69 |
| 6.5 | Parameters of the Novak+18 model. The mean values and deviations were determined from the posterior distribution. | 69 |
| 6.6 | Parameters of the Willott+01 model. The mean values and deviations were determined from the posterior distribution. | 70 |
| 6.7 | Parameters of the best fitting LDDE model. The model is provided in the text in relations (5.19 and 5.20). | 72 |

Chapter 1

Introduction

It is widely believed today that most galaxies have a black hole present in their center (Beckman, V. and Shrader, C. 2012). When matter falls onto the central black hole, in a process called black hole accretion, it results in electromagnetic radiation being emitted. A simple limit imposed on the maximum possible luminosity, or total power emitted by the source, arising from gravitational force, is called the Eddington luminosity, L_{Edd} (Rybicki & Lightman 2008). It is also common to define the Eddington ratio as the bolometric luminosity of the source divided by the Eddington luminosity, $\lambda_{Edd} = L_{Bol}/L_{Edd}$, where $L_{Edd} = 1.5 \cdot 10^{38} M_{BH}/M_{\odot} \text{ erg s}^{-1}$. Astronomical sources where the central black hole accretes matter, and radiates luminosity, are called active galactic nuclei (AGN). More formally, following Netzer (2015), we define AGN as objects containing a supermassive black hole of mass $> 10^5 M_{\odot}$, accreting matter and emitting radiation at $\lambda_{Edd} > 10^{-5}$. We now describe the historical events leading to the discovery of AGNs and the morphology of AGN in Sect. 1.1. We then describe the bimodality of AGN, and the way they affect the evolution of galaxies as a whole, in Sect. 1.2 and 1.3. In Sect. 1.5 we describe the observational trends in radio AGN evolution. We present the complete physical picture of AGN evolution which represents the current state of knowledge found in the literature in Sect 1.6. Discussion of radio emission from galaxies is briefly outlined in Sect. 1.7.

1.1 Unified model of AGN

During the last century, a wide set of strongly emitting sources have been discovered, constituting a whole 'bestiary' of astronomical objects. An expansive list of these object can be found in Padovani et al. (2017). Here, we list the few most important ones, namely: Type 1 Seyfert, Type 2 Seyfert galaxies, Radio loud quasars ¹, Radio quiet quasars, Broad line radio galaxies, Narrow

¹Quasars or quasi-stellar objects, QSOs

line radio galaxies, Blazars and LINERs (abbreviated from low-ionization nuclear emission-line region). The observational characteristics of these objects are summarised in Table 1.1. Across them a few similarities were observed (Padovani et al. 2017). Firstly, they exhibited very high luminosities, and as such were visible at high redshifts. By redshifts, z , we mean a measure of distance in astronomy parametrised by a shift in observed frequency towards the red part of the spectrum due to the expansion of the Universe. It is defined via observed and emitted frequencies of a source, as:

$$1 + z = \frac{f_{emit}}{f_{obs}} \quad (1.1)$$

Since the speed of light is finite, it is also a measure of cosmic time. Secondly, the observed emission of these sources was spread over a wide spectrum of frequencies. Furthermore, from their variability, it was inferred that the emitting regions were small (\sim mpc) for most frequencies.

Table 1.1: The AGN types determined via observational characteristics. Modified from Carroll & Ostlie (2014).

| Type | Characteristics |
|----------------------------|--|
| Type 1 Seyfert | Both narrow and broad lines, X-ray emission, weak in radio, found in spiral galaxies, variable |
| Type 2 Seyfert | Narrow emission lines, weak radio and X-ray emission, found in spiral galaxies, not variable |
| Radio loud quasars | Both narrow and broad lines, strong emission in radio, variable |
| Radio quiet quasars | Both narrow and broad lines, weak emission in radio, variable |
| Broad line radio galaxies | Both narrow and broad lines, strong emission in radio, found in elliptical galaxies, variable |
| Narrow line radio galaxies | Narrow emission lines, strong emission in radio, found in elliptical galaxies, not variable |
| Blazars | Almost no emission lines, strong emission in radio, found mostly in elliptical galaxies, very variable |
| LINERs | Similar to low-luminosity Seyfert 2 galaxies |

By the term "unified model of AGN" we mean a physical picture where all of these observed

objects are explained by small number of physical parameters (Netzer 2015). The simpler and older version of the unified model (Antonucci 1993, Urry & Padovani) describes all the observations via a single physical object, an AGN model of morphology shown in Fig. 1.1. The different detected objects are then a consequence of observations and source luminosity.

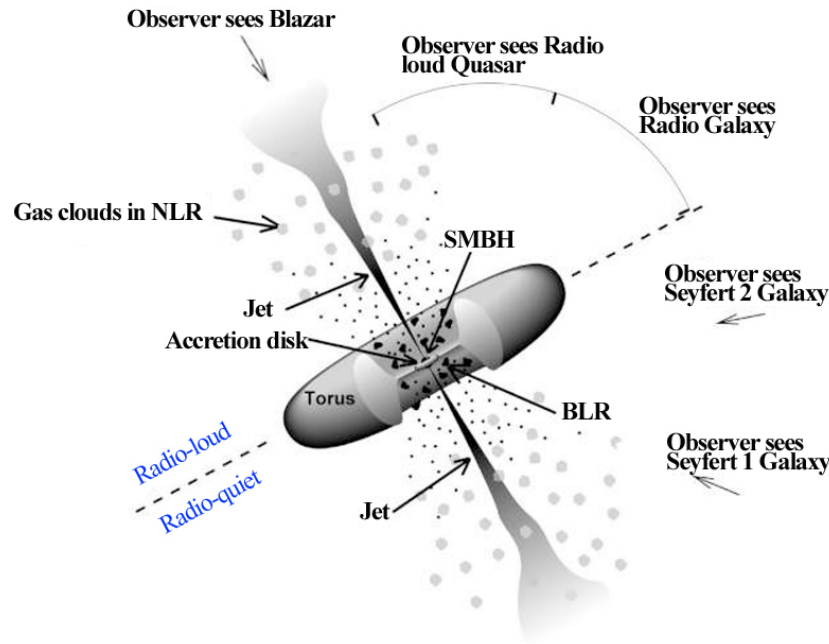


Figure 1.1: The unified model of AGN. The morphology of the model, described in detail in the text, is denoted in the figure. Here SMBH stands for supermassive black hole, while BLR and NLR denote the broad and narrow line regions respectively. The way the morphology influences the observations is also denoted in the figure, showing how the inclination changes what the observer would see. The figure also shows the AGN dichotomy between radio loud and quiet AGN, but this already leads to AGN bimodality, described in the next section. Modified from Urry & Padovani (1995).

We now describe the morphology of the AGN model in more detail. In the very centre of the AGN, at $10^{-7} - 10^{-3}$ pc, there exists a supermassive black hole (SMBH). The properties of the black hole are its mass and spin (Padovani et al. 2017). The mass of the black hole is especially important as it changes the Eddington limit of the AGN. Therefore more massive black holes can result in more luminous AGNs. The AGN emits radiation due to the matter falling onto the central black hole. Matter falls onto the black hole in a sub-pc ($10^{-7} - 1$ pc) rotating accretion disk. The in-falling matter in the disk loses its angular momentum via friction, radiating energy brightly at UV (and from optical to X-ray) frequencies (Urry & Padovani 1995, Padovani et al. 2017). The frequencies likely change with radii of the accretion disk (Padovani et al. 2017), where matter closest to the black hole radiates energy in X-ray, via inverse Compton scattering from a relativistic electron cloud above the accretion disk, called the corona (Urry &

Padovani 1995, Uttley et al. 2014). Further outwards from the black hole, the disk is surrounded axisymmetrically at $0.1 - 10$ pc by the dusty torus. The two main effects of the torus are emission in the infrared part of the spectrum, originating from the warm dust, and the obscuring effect, where the torus obscures the inner parts of the AGN (Padovani et al. 2017). Closer to the black hole, perpendicular to the plane of the disk and torus, at $0.01 - 1$ pc, is the broad line region (BLR). This region consists of high density, dust-free gas, moving at high velocities. The name originates from the fact that the spectral lines are Doppler broadened. At larger distances from the black hole, at $10 - 1000$ pc is the narrow line region (NLR). This region contains ionised gas at lower velocities, containing dust. Perpendicular to the torus there can also exist radio jets ($10^{-7} - 10^6$ pc). These are two sided, highly collimated outflows, spanning large distances from the central black hole (Heckman & Best 2014). Jets dominate AGN emission in γ -rays and radio, and can also emit X-rays (Padovani et al. 2017).

According to the simpler unified model, the different objects detected observationally are a consequence of only two parameters: source inclination relative to the observer and source luminosity. Depending on the inclination of observations, different classifications emerge, as shown in Fig. 1.1. For example, observing the AGN with line of sight parallel to the dusty torus can obscure the broad emission lines originating from the broad line region. More recent evidence, however, suggest that this simple model is not sufficient. For example, the strength of radio jets varies from source to source (Padovani et al. 2017). Furthermore, AGN activity varies in time. In other words, an evolution of AGN properties through cosmic time exists, which needs to be explained (Padovani et al. 2017). A more recent AGN unification model divides them into two groups: "radiative mode AGNs" and "jet mode AGNs" (Heckman & Best 2014). We discuss this model in detail in the next section.

1.2 AGN Bimodality

The simple unification model described in the last section was recently expanded in order to better describe the observational and evolutionary differences observed for AGN. This newer AGN model assumes there are two categories of AGN (e.g. Heckman & Best 2014 for a review). The first of these converts the potential energy of the in-falling gas efficiently and emits energy primarily via electromagnetic radiation. Returning to the AGN classes listed in Tab. 1.1, they would correspond to Seyfert galaxies or quasars. These objects are referred to as radiatively efficient AGN or radiative mode AGNs, mentioned in the last section. The second category of AGN produce less energy, mostly in the form of kinetic jets. They are referred to as radiatively inefficient AGNs or jet mode AGNs (Heckman & Best 2014). Returning to Tab. 1.1 they would

correspond to radio galaxies.

The two categories of AGN are explained within this model via two different types of black hole accretion. The radiatively efficient population accretes cold matter onto the central black hole at high Eddington ratios, λ_{Edd} , above a limit of 1% to 10% (Heckman & Best 2014, Smolčić et al. 2017a, Padovani et al. 2017). The matter falls onto the central black hole in an optically thick geometrically thin accretion disk flow (Shakura & Sunyaev 1973, Heckman & Best 2014). The morphology of this type of AGN is shown schematically in the left side of Fig. 1.2. This morphology follows the one described in the last section for the unified model. The radiatively inefficient population accretes hot intergalactic medium at lower Eddington ratios, of typically $\lambda_{Edd} \lesssim 1\%$ (Heckman & Best 2014). The matter falls onto the central black hole via a geometrically thick optically thin accretion flow (Narayan et al. 1998). The defining property of these AGNs are the launching of jets, although a smaller fraction of radiative mode AGNs can also produce jets, especially those with large black hole masses (Heckman & Best 2014). The jets emit strong radio emission via synchrotron radiation. The morphology of this type of AGN is shown schematically in the right side of Fig. 1.2. Although an accretion disk can still be present, it is truncated and the bulk of the accretion occurs by a geometrically-thick advection-dominated accretion flow, or ADAF (Heckman & Best 2014).

The "radiative mode" AGN are a small fraction of the galaxy population (< few percent) and are luminous in X-ray, optical, infrared and sometimes also via strong radio emission (Heckman & Best 2014, Netzer 2015). They are more common in galaxies with ongoing star formation and younger stellar populations. "Jet mode" AGN are luminous in radio, and are found in the most massive systems $M > 10^{11} M_{\odot}$, where the stellar populations are older (Harrison 2017). Since different modes of AGN accretion are situated in different types of galaxies, it would follow that an interplay between the AGN and the host galaxy must take place. This interplay is currently a very lively topic in the literature, and is called AGN feedback. We describe it in detail in the next section.

The bimodality of galaxies into blue galaxies with ongoing star formation, and red galaxies with little star formation is a well established fact (e.g. Strateva et al. 2001, Kauffmann et al. 2003). Blue galaxies have smaller stellar masses, and correspond to late Hubble type galaxies i.e. spiral galaxies. The red galaxies have larger stellar masses and correspond to early Hubble type galaxies i.e. elliptical galaxies. The two types of galaxies are commonly explained via an evolutionary model where the blue galaxies increase their mass via gas accretion and mergers, until the star formation is quenched and they turn into the red population (e.g. Lilly et al. 2013). This is shown in Fig. 1.3 where the two types of galaxies are plotted in a graph of star formation vs stellar mass. The process that quenches the star formation and turns the galaxies "red and

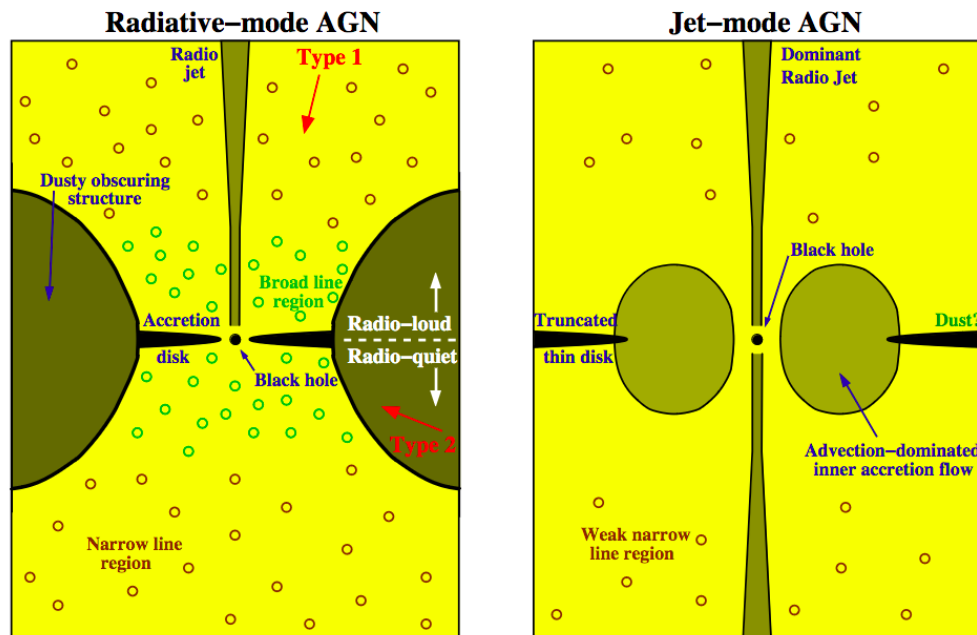


Figure 1.2: The schematic representation of AGN bimodality. The two types of AGN are shown in the figure. Left is the radiative mode AGN. The morphology of these objects follows the morphology of the simpler AGN unified model found in Fig. 1.1. In red it is also denoted how different inclinations of observations result in inner parts of AGNs being or not being obscured. On the right the radiatively inefficient AGN is shown. The accretion occurs via geometrically thick accretion flow, as described in the text. Taken from Heckman & Best (2014).

dead" is still a matter of some debate. It is usually accepted that the host galaxy needs an additional process to take place in order to quench the star formation. This is then attributed to processes such as galaxy collisions, mergers, ram-pressure, or the influence of AGN over the host galaxy. Returning to the bimodal model of AGN, the two modes of accretion, found in two types of galaxies, therefore may represent two distinct evolutionary phases of AGN evolution. This is also shown in Fig. 1.3, where the two AGN types are shown to correspond to the two types of host galaxies. The model of galaxy evolution is discussed further in Sect. 1.6.

1.3 AGN Feedback

It is now widely accepted that the physics and evolution of AGNs is tightly connected with the evolution of their host galaxy. This process of mutual influence between the central black hole and the rest of the galaxy is called AGN feedback (e.g., Harrison et al. 2018). The main idea is outlined as follows. The accretion of matter onto the central black hole causes a large release of

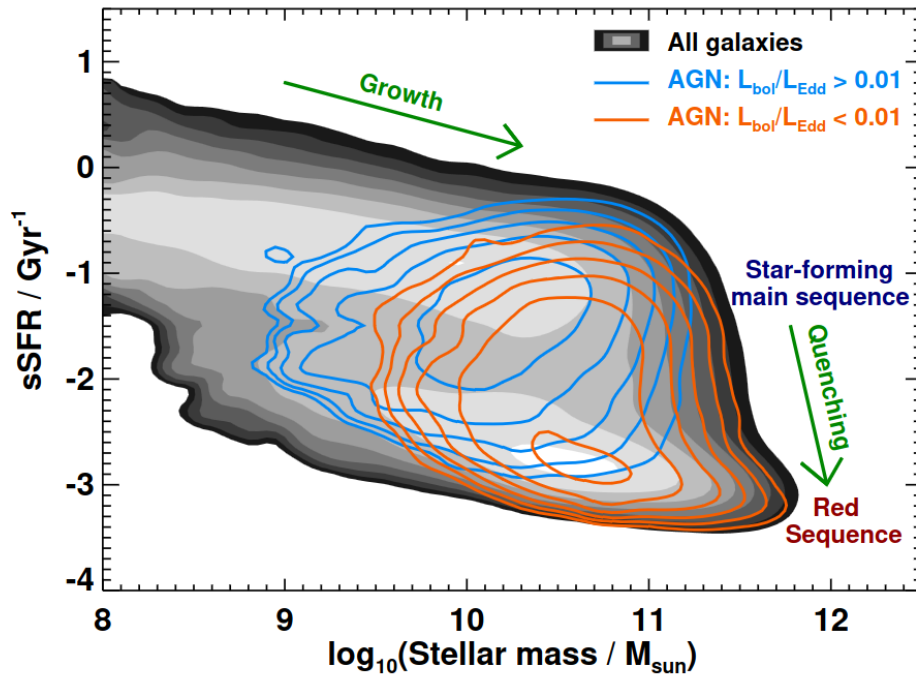


Figure 1.3: The graph detailing the evolution of galaxies. The complete sample of galaxies, given in gray, are plotted in the graph showing their stellar mass vs specific star formation rate (sSFR), or star formation rate divided by stellar mass. The green lines represent the growth of blue galaxies and their quenching. The quenching moves them from the star-forming main sequence of the graph (blue galaxies), towards the red sequence (red galaxies). The contours denote the AGN volume densities. The blue contours correspond to luminous AGN selected via bolometric luminosity, or roughly the radiative mode AGNs, while the red contours correspond to less luminous AGN, or the jet mode AGN. The graph shows that different type of AGN are hosted in different types of galaxies. Taken from Heckman & Best (2014).

energy, outward from the black hole, emitted across the electromagnetic spectrum (Husemann & Harrison 2018), and via radio jets. The radio jets heat the surrounding material mechanically, preventing gas cooling, while the electromagnetic radiation creates winds, causing in turn an outflow of gas from the host galaxy. Although this gas outflow can also be caused by stellar feedback², it is out-shined by AGN feedback when it exists (Wylezalek & Morganti 2018). The gas outflow impacts both the growth of the central black hole in the nucleus of the galaxy, and the star formation rate of the host galaxy, since both of these processes are fuelled by the same gas reservoir of the host galaxy (Harrison 2017). By the term gas reservoir, we mean the quantity of gas that is able to cool down, and thus feeds star formation and black hole

²Such as: stellar outflows and winds, supernova (SN) remnants, planetary nebulae (PN), cosmic rays or photo-ionization

growth. Both star formation and AGN feedback reduce this fuel quantity via radiation, winds and jets (Harrison 2017). Since AGN feedback is proportional to the mass accretion onto the central black hole, there emerges therefore a self-regulating process or an interplay between the gas inflow and feedback. This interplay is sketched in Fig. 1.4. The physical picture is further complicated by the fact that, due to the shocks, heat or jet kinematic disturbances, AGN feedback can both reduce and enhance the star formation of the galaxy (Harrison 2017). The enhancement of star formation in outflows could be due to the increase in gas density, and has been detected via observations (Maiolino et al. 2017). The main effect of feedback, though, is thought to be the reduction of star formation. The evolution of AGN through cosmic time is therefore obviously connected with the evolution of their respective host galaxy. The process turning blue galaxies into red galaxies with little star formation, discussed in the last section, is within this picture therefore attributed to AGN feedback.

Furthermore, in groups and clusters of galaxies, the gas is hot and radiates in X-ray. The fact that it cools slower than expected is known as the ‘cooling flow’ problem (e.g. Cattaneo et al. 2009), and can be explained also via AGN feedback. More specifically, it can be explained via radio jets creating cavities and shocks in the inter-cluster medium, and therefore acting as a heating mechanism (Cattaneo et al. 2009).

In AGN, the outflows are driven by two main mechanisms: outflow by radiation from the AGN and outflow from mechanical effects of radio jets (Wylezalek & Morganti 2018, Harrison 2017). Although more collimated, and as such thought to penetrate the host galaxy with more ease, radio jets have recently been shown in simulations to affect the host galaxy in significant ways (Wylezalek & Morganti 2018), especially in the more dense environments (Harrison 2017). The radiative mode is also called “quasar” or “wind” mode and is associated with high Eddington ratios (> 0.01), while the mechanical mode is called “radio” or “jet” mode and is associated with low Eddington ratios (Harrison 2017). This bimodality in feedback mechanisms is connected to the bimodality of AGN, already discussed in Sect. 1.2. The details concerning the outflow mechanism, however, require further study. The current discussion regarding the outflows is summarised in Fig. 1.5. In short, the size and geometry of outflows, the outflow mechanism and the effect on different phases of gas in the host galaxy is still a point of discussion (e.g. Liu et al. 2013, Harrison et al. 2014, McCourt et al. 2015, Rupke et al. 2017, Cicone et al. 2018, Cresci & Maiolino 2018, Richings & Faucher-Giguère 2018, Rose et al. 2018). Furthermore, the duration during which the black hole is active, and the repeating pattern of such episodes, may vary across galaxies (Wylezalek & Morganti 2018). Estimates were made via tracing AGN activity signatures, dubbed ‘AGN archaeology’, and have estimated the episodes ranging from longer $10^7 - 10^8$ yr to shorter $10^4 - 10^5$ yr, and even a possibility of extremely

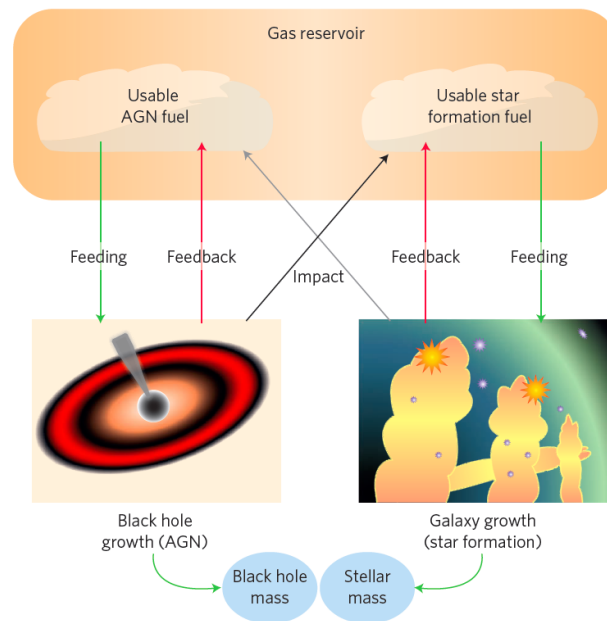


Figure 1.4: A schematic picture showing the effect of AGN feedback on galactic gas reservoir and the effect on star formation and black hole growth. The arrows denote the way certain processes affect the available fuel. It is important to notice the crossed grey and back arrows denoting that there exist an interplay between the AGN and the host galaxy. The lowest part of the figure sketch how these effects impact the mass of the black hole and the stellar mass of the host galaxy. Taken from Harrison (2017).

short (\sim yr) activity (Morganti 2017). The question of how long the episodes of outflow last, are connected to the questions on long-term effects on the host galaxy (Harrison 2017), or in other words, whether the AGN feedback always quenches the star formation of the host galaxy, or acts in a way that only reduces it.

Since only a small portion of energy released by the AGN is enough to regulate black hole growth and star formation (Harrison 2017), it seems like a likely way to explain observed trends of galaxy evolution. The existence of feedback must however be backed by observations. From a more observation-oriented angle, there are several ways to deduce the existence of AGN feedback. One, indirect, way of deducing the interplay between the nucleus and the rest of the galaxy is to observe the correlations between the masses of the central supermassive black hole and the properties of the host galaxies, for instance, the stellar velocity dispersion, the stellar mass of the bulge, or the bulge luminosity (Magorrian et al. 1998, Ferrarese & Merritt 2000, Gebhardt et al. 2000, Graham et al. 2011, Sani et al. 2011, Beifiori et al. 2012, McConnell & Ma 2013). A more direct imprint of AGN feedback can be seen in galactic winds (e.g., Nesvadba et al. 2008, Feruglio et al. 2010, Veilleux et al. 2013, Tombesi et al. 2015) and X-ray cavities in groups and clusters of galaxies (Clarke et al. 1997, Rafferty et al. 2006, McNamara

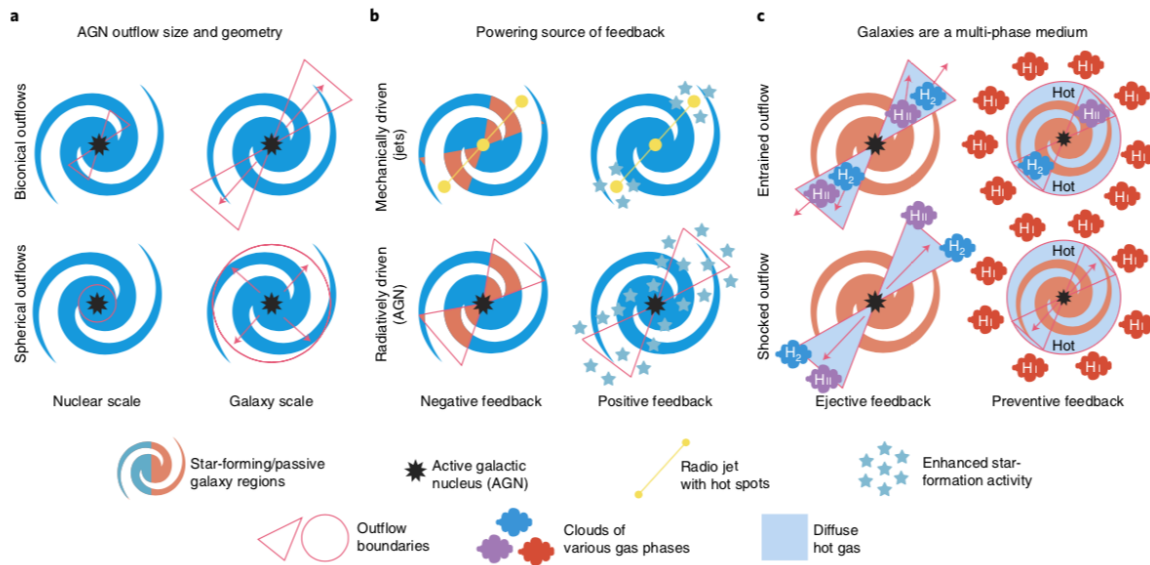


Figure 1.5: The current state of AGN discussion presented schematically. On the left is pictured the current picture about the shape and scale of AGN outflows. The middle part of the figure shows the effects of the feedback on star formation, both positive and negative, and the powering mechanisms. On the right is the way that the outflows affect different phases of galaxy gas. Taken from Husemann & Harrison (2018).

& Nulsen 2007, Fabian 2012, Nawaz et al. 2014, Kolokythas et al. 2015). By galactic winds we mean a centrally driven large scale outflows arising from the centre of the galaxy, which in turn impact its gas supply. They were observed for both radio quiet Seyfert galaxies (Tombesi et al. 2015), some high redshift quasars (Chartas et al. 2014, Gofford et al. 2014) and also in quiescent galaxies with low-luminosity AGN (Cheung et al. 2016). In nearby massive galaxies, the feedback mechanism has been shown observationally to regulate the star formation of the host galaxy, where it was observed that star formation histories of the galaxies, inferred from integrated optical spectra, depend on the mass of the central supermassive black hole (Martín-Navarro et al. 2018). The star formation was quenched earlier in galaxies hosting more massive black holes. Generally speaking, the star formation histories and black hole growth in the Universe are similar through cosmic time. This is illustrated in Fig. 1.6, showing observational estimates of star formation rate and black hole growth as a function of redshift. The matching shape of these curves is another piece of evidence pointing towards AGN feedback.

Lastly, AGN feedback has become an essential element of state-of-the-art models of galaxy evolution (e.g., Croton et al. 2016, Harrison et al. 2018). In these simulations feedback is required to regulate star formation, and failing to implement it causes the simulations to estimate the number and properties of massive galaxies in the local universe wrong (Martín-Navarro et al.

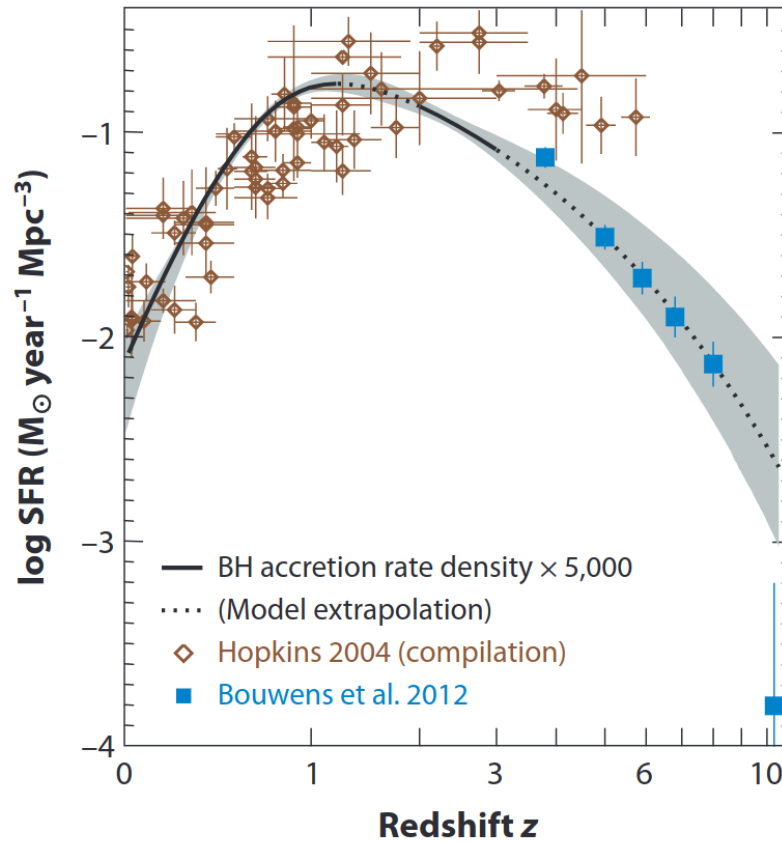


Figure 1.6: The star formation estimates compiled by Hopkins (2004) and Bouwens et al. (2012) given via orange and blue data points, compared to the black hole accretion rate, multiplied by 5000 for comparison. Taken from Kormendy & Ho (2013).

2018). Altogether, a physical picture emerges where there exists an interplay between the black hole in the center of the galaxy and the properties of the host galaxy itself. In other words the evolution of galaxies through cosmic time is connected to the evolution of AGNs, and studying the AGN evolution has important implications for galaxy evolution as a whole.

1.4 Luminosity functions

A method to determine the space density of AGN and to quantify their evolution through cosmic time is to construct the luminosity functions (LFs) of the observed AGN sample. The LFs are a distribution that shows the space density of astronomical sources as a function of their luminosity. The change of LFs through cosmic time is parameterised via their change in redshift. The LFs are therefore functions of both luminosity and redshift $\Phi(L, z)$ and their unit is

usually given in Mpc^{-1} . The shape of the local LF (i.e. at $z \approx 0$) is parameterised via a function possessing a knee, either a power-law with an exponential cut-off, called the Schechter function (e.g. Sadler et al. 2002), or a double power-law function (e.g. Dunlop & Peacock 1990). The schematic sketch of a typical LF is given in Fig. 1.7.

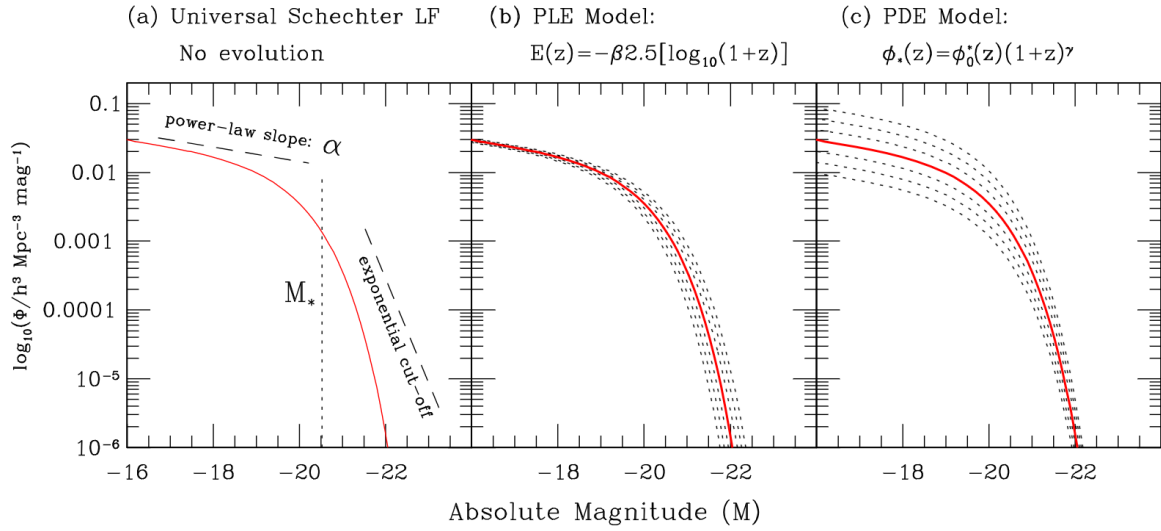


Figure 1.7: A typical Schechter function and the two main modes of LF evolution. The x-axis shows magnitude, which is proportional to \log -luminosity. In the left a LF with no evolution is shown in red. The part of the LF corresponding to a power-law slope and exponential cut-off are denoted via text in the figure. The magnitude of the "knee" is denoted as M^* , while α denotes the faint-end slope steepness. The middle panel of the figure shows the evolution in luminosity (PLE model) as a function of redshift $E(z)$. The red line denotes the local LF, Φ_0 , while the black dashed lines denote the evolved LF for both positive and negative evolution. The panel on the right is the same as the middle panel but for evolution in density (PDE model). Factors β and γ are the evolution parameters, taken here to be constants. The evolution of LF in the figure depends on redshift, but the plots would look qualitatively identical for constant evolution. Taken from Johnston (2011a).

As already stated, tracing the change of AGN LFs with redshift provides insight into the evolution of AGN. The two main modes of evolution are the evolution in density (called pure density evolution or PDE), where the number of AGN changes with redshift, and the evolution in luminosity (called pure luminosity evolution or PLE), where the luminosity of sources changes. Often, it is also common to assume a superposition of these two modes. A wide set of more complex models is found throughout the literature, where the evolution parameters depend on either redshift or luminosity. It is also possible to assume different evolution for sub-populations of AGN. We list and discuss a large number of these models in Sect. 5.4.2.

In practice the LFs can be constructed via parametric or non-parametric methods. The

parametric methods assume a specific functional form of the LF, $\Phi(L, z)$, while non-parametric methods require no such assumptions. It follows that non-parametric methods trace the LFs more directly but fail to provide an analytical form for AGN density and evolution. The most widely used non-parametric method is the method of maximum volumes by Schmidt (1968), designed to eliminate the bias arising from a finite sensitivity of astronomical observations. We describe this method in detail in Sect. 5.5. A review of LF estimation methods can be found in Johnston (2011a).

1.5 Evolutionary trends in radio-detected AGNs

Since this thesis is concerned with radio observations, or more specifically, with AGN observed in the radio part of the spectrum, we limit our discussions now to radio-detected AGNs. A wealth of surveys investigating the evolution of radio AGNs is present in the literature (e.g. Waddington et al. 2001, Willott et al. 2001, Clewley & Jarvis 2004, Sadler et al. 2007, Smolčić et al. 2009, Donoso et al. 2009, Padovani et al. 2015, Pracy et al. 2016, Padovani et al. 2017, Butler et al. 2019, Ocran et al. 2021). The evolution of radio-detected AGNs in these surveys was estimated by constructing the LFs of the radio-detected samples. Some of the surveys limit the LF creation only to non-parametric methods (e.g. Waddington et al. 2001, Sadler et al. 2007, Donoso et al. 2009, Rigby et al. 2015), but it is also common to model the evolution of radio-detected AGNs via analytical functions. Most commonly, the evolutionary model assumed is the PDE or PLE model, introduced in the last section (e.g. Pracy et al. 2016, Ocran et al. 2021). More complex models of LFs have also been used. For example, these are redshift-dependent evolutionary models (Novak et al. 2017, Ceraj et al. 2018), and a bimodal model, assuming different shapes and evolutions for AGNs with high and low luminosity (Willott et al. 2001).

Of special interest is the tendency throughout the literature to examine specific sub-populations of radio-AGNs, as a possible difference in evolution between these sub-populations could provide further insight into the details of the processes taking place within them. The exact classification, however, varies across the literature. One possible subdivision is via relative excess of radio emission, compared to the emission in the optical part of the spectrum, into radio loud (RL) and radio quiet (RQ) AGN (e.g., Padovani et al. 2015, Ocran et al. 2021). Another possibility is the division via emission lines in the optical spectrum into high or low excitation radio galaxies (HERGs and LERGs, respectively; e.g., Pracy et al. 2016, Butler et al. 2019). A combination of X-ray and mid-infrared criteria and broadband spectral energy distribution fitting was used by Delvecchio et al. (2017) and Smolčić et al. (2017) to divide the sample into moderate-to-high radiative luminosity AGNs (HLAGNs) and low-to-moderate radiative lumi-

osity AGNs (MLAGNs). Division via luminosity into high and low luminosity sources is also common (e.g. Rigby et al. 2015). A more complete review of AGN classification is found in Padovani et al. (2017).

The results of these surveys tend to find a difference in evolution between the sub-populations. When the sample is divided into high and low luminosity sources (Waddington et al. 2001, Clewley & Jarvis 2004, Sadler et al. 2007, Smolčić et al. 2009, Donoso et al. 2009, McAlpine & Jarvis 2011, Padovani et al. 2017) the resulting trend is that there exists a difference in the evolution of high- and low-luminosity sources, where the high-luminosity sources are the ones that evolve faster. Studies of RL and RQ AGNs find that the RL sub-populations evolves more strongly (Ocran et al. 2021). A study by Pracy et al. (2016) found that the HERG population of AGNs evolved more strongly than the LERG population. Studies of the HERG and LERG radio LFs in the local universe found that LERGs are the dominant population at luminosities below $L_{1.4 \text{ GHz}} \approx 10^{26} \text{ W Hz}^{-1}$, while HERGs dominate at the highest luminosities (Pracy et al. 2016, Best & Heckman 2012).

The above described AGN classifications are, however, not uncorrelated. Although the classification is not exactly one-to-one, the data always seem to lean towards a bimodal evolution of radio AGN where the sources with higher luminosities evolve faster. More specifically, the space density of the high-luminosity AGN population, with luminosities larger than $\log(L/\text{WHz}^{-1}) \approx 24$, shows a strong evolution from present time, up to redshift $z \approx 2$. After this redshift a cut-off in density is observed (Dunlop & Peacock 1990, Willott et al. 2001, Pracy et al. 2016). The low-luminosity AGN exhibit little evolution, and the cut-off if it exists occurs at larger redshifts (Clewley & Jarvis 2004, Smolčić et al. 2009). Taken together, the trend seen in surveys is therefore that there is a difference in AGN evolution, which is a function of their luminosity. How this fits into the physical picture of galaxy evolution and AGN feedback is described in the next section.

1.6 Hierarchical model and downsizing

Having introduced the required concepts regarding galaxy evolution, AGN evolution and AGN feedback, we now try to sketch a more complete physical picture, corresponding to the current state of knowledge in the literature. The evolution of galaxies is explained via the hierarchical model. In short, after the big bang, or the beginning of our Universe, the first inhomogeneities formed into clumps, where the first galaxies were formed, growing via gas accretion and forming stars. This continued until the gravitational heating stopped the gas accretion (Cattaneo et al. 2009), after which the galaxies grew via mergers, transforming in the process from disks

to ellipticals (Cattaneo et al. 2009). It would also follow that larger black holes are also the product of merging.

By cosmic downsizing, on the other hand, we denote an idea that the more massive black holes form earlier than the less massive ones (e.g., Rigby et al. 2015). It also denotes the fact that most star formation today and most AGN growth occurs in galaxies with lower mass (Kormendy & Ho 2013). This idea is, at first glance, inconsistent with the hierarchical model, where larger black holes form via merging, but the inconsistency can be explained by the AGN feedback mechanism. More specifically, due to feedback there occurs a switch in the mode of accretion between the efficient cold gas accretion to inefficient hot gas accretion, where inefficient accretion starts to dominate at low redshifts (e.g., Heckman & Best 2014, Rigby et al. 2015). As the galaxies merge, the inflow of new gas onto the black hole causes the AGN to respond by releasing energy outward from the centre. This causes galactic winds which can lead to the gas being stripped away from the galaxy. What then occurs is the quenching of star formation of a galaxy, as it becomes a red elliptical (Cattaneo et al. 2009). After turning into red galaxies, the AGN can still operate in what is dubbed 'maintenance mode', adjusting the cooling of gas by a continuous or episodic activity (Cattaneo et al. 2009). This feedback that occurs after the quenching phase is required in order to remove or heat the gas resulting from additional mergers or from stellar injection of matter into the interstellar medium (Cheung et al. 2016). We also note that this does not mean that the star formation rates of the most luminous AGN are the lowest. The quenching can instead be a cumulative effect of previous AGN episodes, with details depending on the timescales of these episodes (Harrison 2017).

The term "downsizing" is also used when describing radio-detected AGN LF evolution. The term then describes the observed tendency for low-luminosity sources to evolve less rapidly than high-luminosity sources (Padovani et al. 2017). As described in the last section, it has been shown that the space density of the high-luminosity population of radio-AGN evolves strongly with redshift up to $z \approx 2$. (Dunlop & Peacock 1990, Willott et al. 2001, Pracy et al. 2016), while the low-luminosity population exhibits little evolution (Clewley & Jarvis 2004, Smolčić et al. 2009). The different evolutions may be related to the different accretion modes. The low luminosity sources would here represent the jet-mode AGNs evolving slowly, if at all, after the star formation quenching, via 'maintenance mode' AGN feedback.

1.7 Radio emission of galaxies

Since the main focus of this work is centred around radio observations, we summarize briefly the mechanisms of radio emission in galaxies. Of most interest here are those processes important

for AGN radio emission, but a broader picture is first presented. Generally speaking, a point charge moving with a nonzero acceleration radiates energy. The total radiated power can be calculated as (Griffiths 2017):

$$P = \int \mathbf{S} \cdot d\mathbf{a} = \frac{\mu_0 q^2 a^2}{6\pi c} \quad (1.2)$$

where q is the particle charge, a the acceleration, c the speed of light and μ_0 the vacuum magnetic permeability. This expression is called the Larmor formula (Griffiths 2017, Condon & Ransom 2016). The formula was derived for non-relativistic particles and does not apply directly to a quantum system (Condon & Ransom 2016). While dealing with radio emission in astrophysics, however, it is usually sufficient to remain within classical electrodynamics (Burke et al. 2019). We now list different emission mechanisms in radio astronomy in order to obtain a fuller picture of radio emission.

1.7.1 Blackbody radiation

An idealised object whose surface absorbs all incoming radiation, called a blackbody, emits radiation depending on its temperature following the Planck distribution (Burke et al. 2019). In radio astronomy it is also usually sufficient to use the Rayleigh-Jeans approximation (given that the frequencies are not too large $h\nu \ll kT$):

$$I_\nu = \frac{2kT\nu^2}{c^2} = \frac{2kT}{\lambda^2} \quad (1.3)$$

The direct proportionality with temperature T is the reason that the spectral brightness is often specified via the Rayleigh-Jeans brightness temperature, even when the approximation is not strictly valid. In practice, this expression can be used when the astronomical object absorbs radiation efficiently.

1.7.2 Free-free emission

Free-free emission (or bremsstrahlung radiation; Burke et al. 2019) is the broadband emission that arises from the acceleration of a charge in the Coulomb field of another charge (Rybicki & Lightman 2008). The name "free-free emission" comes from the fact that one particle is not captured by the other, or in other words, it is free before the collision, and free after the collision (Condon & Ransom 2016). In practice, we assume that the emission arises from electrons accelerated by an ion. In other words, we assume that the radiation arising from ion acceleration, and from electron-electron collisions can be neglected, which is a sound assumption (see

Condon & Ransom 2016 for details). The emission from an electron-ion interaction happens as a pulse, where the electron accelerates approaching the ion and then decelerates as it leaves it. The energy radiated from a single electron-ion interaction, can be calculated from the Larmor formula. In practice, however, we are not dealing with single particle collisions but with a whole population of particles. Depending on the details of the population the resulting spectra differ. If we assume that the population of particles is in thermal equilibrium, we obtain the following equation for the total emission (Rybicki & Lightman 2008, Condon & Ransom 2016):

$$\epsilon_{\nu} = \frac{dE}{dV dt d\nu} = 6.8 \cdot 10^{-38} Z^2 n_e n_i T^{\frac{-1}{2}} e^{\frac{-h\nu}{kT}} g_{ff} \quad (1.4)$$

where n_e, n_i are the number density of electrons and ions, respectively, T the temperature, Z the atomic number, ν the frequency, k the Boltzmann constant and h the Planck constant. We have also introduced $g_{ff}(T, \nu)$, the velocity-averaged gaunt factor which is the quantum corrections to the classical formulas. A good order-of-magnitude approximation is to put $g = 1$ (Rybicki & Lightman 2008). A further complication to this formula arises from the fact that the same population of particles causes absorption. The absorption coefficient depends on the frequency of radiation as $\propto 1/\nu^2$ (Rybicki & Lightman 2008). It follows that at low frequencies the emitting plasma is optically thick and the spectrum is the thermal Rayleigh-Jeans spectrum ($I \propto \nu^2$). At high frequencies the plasma becomes optically thin, and the spectrum of free-free radiation becomes approximately flat. In astronomical sources, the free-free emission arises from the H-II regions, or the places where the interstellar hydrogen is ionized.

1.7.3 Synchrotron emission

Synchrotron emission (or magnetobremstrahlung) is strong broad-bandwidth radiation that arises from electrons accelerated in magnetic fields (Burke et al. 2019). The name originates from synchrotrons, where the effect was important, and it is reserved for ultrarelativistic electrons, as opposed to gyro radiation for $v \ll c$ or cyclotron radiation for mildly relativistic particles (Condon & Ransom 2016). Inside magnetic fields, the particle moves along a helical path with constant speed. Relativistic effects need to be taken into account. Firstly, the radiated power is boosted in the observers frame. Secondly, there exist the effect of relativistic beaming. The relativistic beaming is a consequence of relativistic velocity transformations or relativistic aberration. The emission shape of the Larmor formula is stretched into a narrow beam with opening angle $\approx 1/\gamma$ (Burke et al. 2019). As the electron gyrates, the synchrotron emission is therefore observed as a series of short spikes or pulses. The duration of these pulses is again modified by $1/\gamma^2$ due to relativistic transformations. The spectrum for single particle emission

is the Fourier transform of these pulses. For a single electron we would obtain a spectrum shown in Fig. 1.8 (Condon & Ransom 2016, Carroll & Ostlie 2014). In practice, again, we are not dealing with a single particle but a whole population. For most synchrotron sources we assume a power-law energy spectrum for the electron population, which is, furthermore, homogeneous and isotropic:

$$n(E)dE \propto E^{-\delta}dE \quad (1.5)$$

The peak of emission for a single electron occurs at $\nu \approx \nu_{crit} \propto E^2$. Since we have a whole population of electrons at different energies, we simplify the discussion by assuming that each electron emits radiation at a single frequency (Condon & Ransom 2016), or in other words, sum the individual electron contributions ignoring the details of the individual spectra. This is illustrated in Figure 1.8. All in all, it can be shown that if the energy distribution of the electrons follows a power law, the resulting spectrum is also a power law (Rybicki & Lightman 2008, Carroll & Ostlie 2014, Wilson et al. 2008):

$$F \propto \nu^\alpha \quad (1.6)$$

The factor α is called the spectral index and is connected to δ in the energy distribution as (Condon & Ransom 2016):

$$\alpha = -\frac{\delta - 1}{2} \quad (1.7)$$

Lastly, we include the effects of self-absorption, or the fact that the same plasma that emits radiation also absorbs it. It can be shown that at low frequencies the spectrum of a homogeneous source becomes (Condon & Ransom 2016):

$$F \propto \nu^{5/2} \quad (1.8)$$

In astrophysics synchrotron emission is present in many places. Most notably, and most importantly for this work, it is responsible for most of the radio emission from AGN. It is also present in star-forming galaxies (dominating at frequencies below ≈ 30 GHz).

1.7.4 Complete spectrum

Each of the above described emission mechanisms are combined into a single picture, as shown in Fig. 1.9. As seen from the figure each process is dominant at different wavelengths. For AGN the dominant contribution to radio emission is the synchrotron emission. Throughout this thesis we therefore assume that the radio emission is given by a power law as in relation (1.6). This

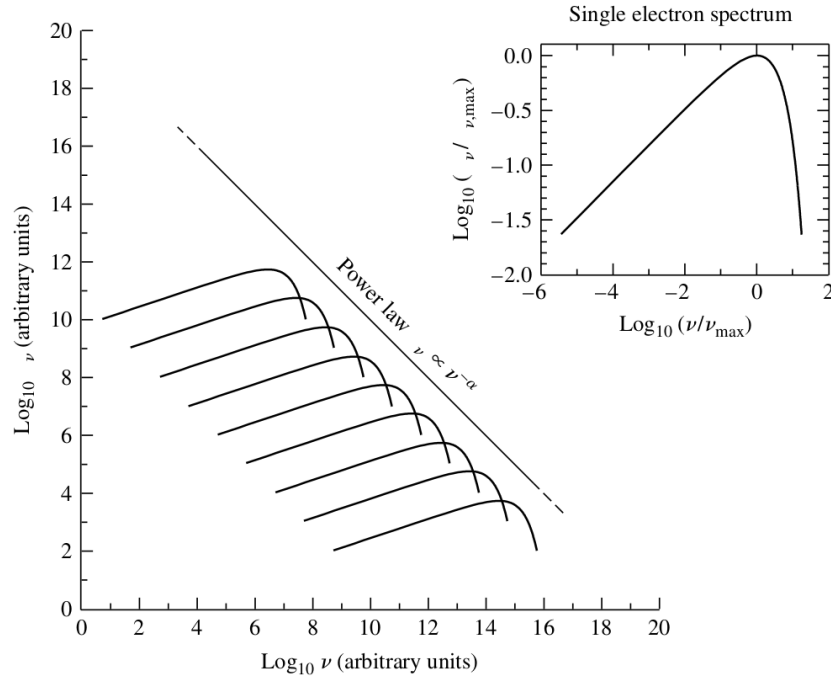


Figure 1.8: Spectrum of a population of electrons arising from a superposition of individual spectra. Spectrum of a single electron is pictured in the upper right corner of the figure (notice the log-scale). Taken from Carroll & Ostlie (2014).

simplifies things greatly as shifting the radio emission from one frequency to another becomes simple, assuming the spectral index is determined. Furthermore, owing to this simple power-law of emission, the spectral indices are possible to determine using observations at different radio frequencies.

1.8 Thesis outline

The picture outlined in the introductions shows the connection between the AGN evolution and the theory of galactic evolution as a whole. We also showed that there are various models of fitting the LFs. The better constraint on the AGN LF curves would lead to clearer understanding of the AGN population evolution, for which many attempts were made. The prime goal of this thesis was to compare different LF fitting models on the data observed by various surveys, thus potentially better constraining our models of evolution of the AGN populations. In this thesis, we explore the evolution of AGN detected in the radio part of the spectrum. The LFs are determined both via parametric and non-parametric methods, using data from multiple

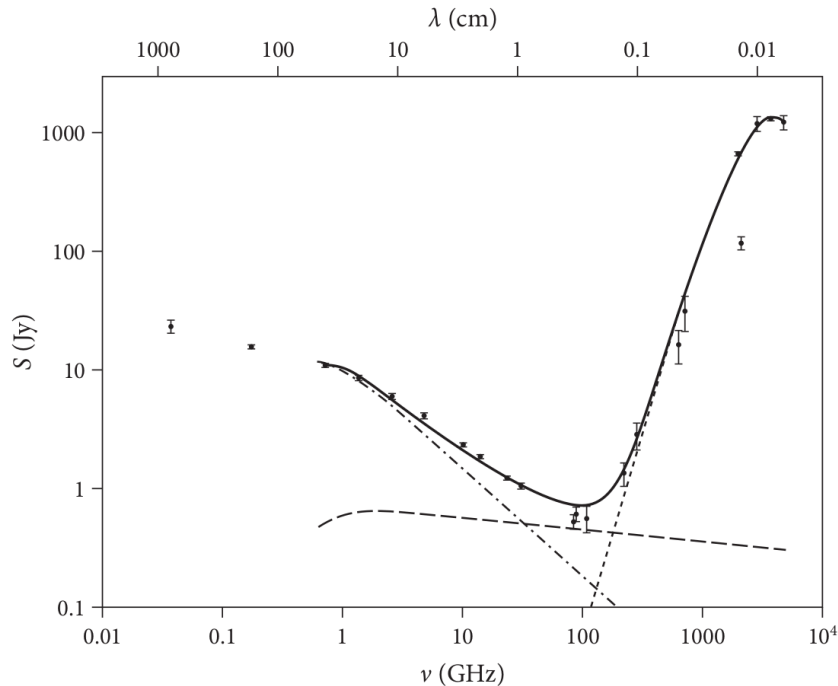


Figure 1.9: The radio and infrared part of the spectrum of M82, a starburst galaxy. The horizontal dashed line denotes the free-free emission. The dot-dashed line at low frequencies denotes the synchrotron radiation. The dotted line at higher frequencies corresponds to the thermal emission from dust. Together they form the radio spectrum of the galaxy (full line). The figure shows the emission from theory as well as real observational data. Taken from Condon & Ransom (2016)

surveys, spanning for the first time such a large interval in redshifts (up to $z \sim 3.5$) and luminosities ($\log(L/\text{WHz}^{-1}) \in [22, 29]$). The surveys used were the 7C, 6CE and 3CRR surveys from Willott et al. (2001), the XXL North and South fields (Butler et al. 2018a, Smolčić et al. 2018) and the COSMOS field (Smolčić et al. 2017a). The surveys are described in detail in Ch. 2.

The outline of the thesis is as follows. In Ch. 2 we describe the complete set of surveys used to constrain the LFs. In Ch. 3 and 4 we concentrate on the XXL-North field. As the cross-correlation process, or the identification between the radio and multi-wavelength data, was performed as part of this thesis, we describe it in detail in this section. We also construct the LFs using only the XXL-North field and discuss the results. In Ch. 5 and 6 we return to the complete composite survey and create the LFs using all the available catalogues. The LFs are determined parametrically within the Bayesian framework. This resulted in an analytical function being determined that describes the density and evolution of the AGN data set best. The implication of the best fitting model on the physical picture and the discussion of our

results within the literature is given in Ch. 7. The summary of the thesis and the outlook is given in Ch. 8.

Throughout this thesis we use a cosmology defined with $H_0 = 70 \text{ kms}^{-1}\text{Mpc}^{-1}$, $\Omega_m = 0.3$, and $\Omega_\Lambda = 0.7$. The spectral index, α , was defined using the convention in which the radio emission is described as a power law, $S_\nu \propto \nu^\alpha$, where ν denotes the frequency, while S_ν is the flux density. Here flux denotes the power detected per unit area of the detector. Flux density is flux per unit frequency.

The results of this Thesis are published in the following papers:

1. **B. Šlaus**, V. Smolčić , M. Novak, S. Fotopoulou, P. Ciliegi, N. Jurlin, L. Ceraj, K. Tisanić, M. Birkinshaw, M. Bremer, L. Chiappetti, C. Horellou, M. Huynh, H. Intema, K. Kolokythas, M. Pierre, S. Raychaudhury, H. Rottgering, 2020, A&A, 638, A46, (XXL Paper XLI), *The XXL Survey. XLI. Radio AGN luminosity functions based on the GMRT 610 MHz continuum observations*,

2. **B. Šlaus** V. Smolčić , Ž. Ivezić , S. Fotopoulou, C. J. Willott, P. Pendo , submitted to A&A, *The XXL survey LII : The evolution of radio AGN luminosity function determined via parametric methods from GMRT, ATCA, VLA and Cambridge interferometer observations*.

Chapter 2

Data

In order to constrain the LFs over a large interval of luminosities and redshifts it is necessary to use surveys of varying area and depth. By survey area we mean the span of the sky covered by the survey. By depth we mean the sensitivity of the survey to incoming flux. Since faraway objects are generally fainter, it follows that the sensitivity of the survey determines how far in redshift the observed objects will reach, or the depth of the survey. Deep surveys of smaller area, are used to constrain the LFs at high redshifts, but lack a large enough quantity of high luminosity sources, due to the fact that high luminosity sources are statistically rare in the Universe. In order to observe them in significant numbers, it is necessary to use surveys with a large observational area. These surveys can, on the other hand, be shallow, since the large luminosity of these sources makes them easier to detect. In this work we use the deep VLA-COSMOS 3 GHz Large Project survey (Smolčić et al. 2017a) and the shallow 7C, 6CE and 3CRR surveys (taken from Willott et al. 2001). In order to bridge the gap between these two extremes we also used surveys of intermediate area and depth, namely the XXL North and South fields (Smolčić et al. 2018, Butler et al. 2018a). The areas and detection limits of these surveys are shown in Fig. 2.1, and listed in Tab. 2.1. We describe them in more detail in the following sections. Sect. 2.1 describes the shallow 7C, 6CE and 3CRR fields, while Sect. 2.2 describes the deep COSMOS field. The intermediate XXL South and North fields are presented in Sect. 2.3 and 2.4. A sub-sample of AGNs is selected in Sect. 2.5, and the complete data set is summarised in Sect. 2.6. The process of observing these fields and creating the corresponding source catalogues was not performed as a part of this work. We therefore refer the reader to the relevant publications for details and present the data sets by describing their properties relevant for this work.

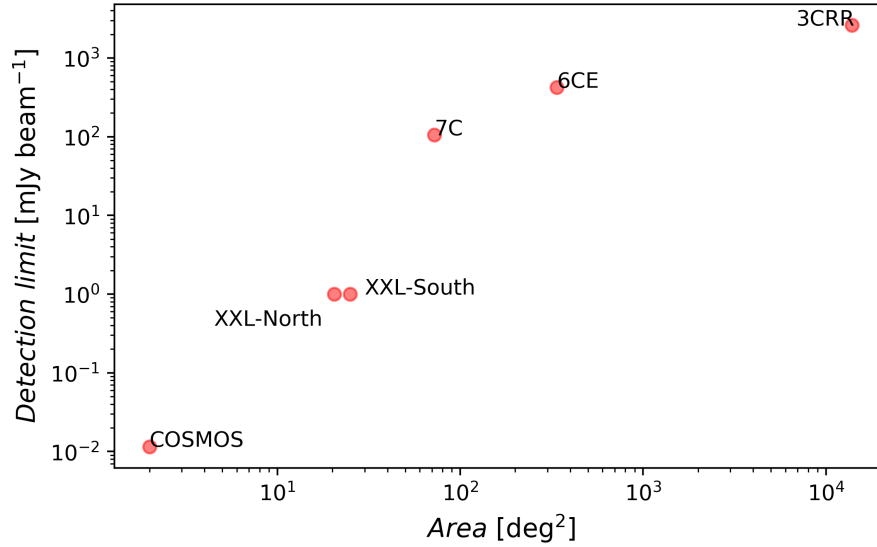


Figure 2.1: The areas and detection limits of the fields used in this work, which together form the composite survey. The detection limits were shifted to a frequency of 1.4 GHz for easier comparison, assuming a power law radio spectrum. The detection limits of the XXL-North and South surveys correspond to the pure AGN sample selected via a threshold in flux, as described in Sect. 2.5.

2.1 3CRR, 7C and 6CE fields

The three shallow surveys, with a large observational area, used in this work were the 7C, 6CE and 3CRR fields (obtained from C. Willott, private communication). The observations were performed with the Cambridge Low-Frequency Synthesis Telescope and the Cambridge Interferometer. A brief summary of each survey is given below and the details are available in Willott et al. (2001) and references therein.

The 7C field consists of three distinct regions: 7C-I, 7C-II and 7C-III, spanning a total area of 72.22 deg^2 (i.e. 0.022 sr). The observations were performed at 151 MHz and the detection limit equalled 0.5 Jy, resulting in a catalogue containing 128 sources. The redshifts of the sources were determined from follow-up optical and near-infrared observations, most of them being determined spectroscopically ($\approx 85\%$) and the remaining photometrically. The spectral indices were obtained from multifrequency radio data for 7C-I, 7C-II, and 38 MHz 8C data for 7C-III (Lacy et al. 1999). The mean spectral index of all the sources in the survey equalled $\alpha \approx -0.64$.

The 6CE survey was observed at 151 MHz and covered an area of 338.13 deg^2 (0.103 sr).

The flux limit of the survey was between flux densities of $2 \text{ Jy} < S_{151 \text{ MHz}} < 3.93 \text{ Jy}$ (Rawlings et al. 2001). The number of sources equalled 59. The redshifts of 56 of these sources were determined spectroscopically. The spectral indices were determined by a polynomial fit to the multi-frequency data (Rawlings et al. 2001) with the mean value being $\alpha \approx -0.51$. More details on the catalogue can be found in Rawlings et al. (2001).

The 3CRR survey was observed at 178 MHz and spans an area of 13886.3 deg^2 (4.23 sr). The detection limit was 10.9 Jy and the catalogue contained 173 sources. All of these sources have spectroscopic redshift information available. The spectral index was calculated at rest frame 151 MHz and had a mean value of $\alpha \approx -0.67$.

In order to make these catalogues consistent with the others used in this work we calculated the 1.4 GHz rest-frame radio luminosities for these surveys from flux, redshift and spectral index values given in the corresponding catalogues, using a newer cosmology, defined in Ch. 1 ($H_0 = 70 \text{ kms}^{-1}\text{Mpc}^{-1}$, $\Omega_m = 0.3$, and $\Omega_\Lambda = 0.7$), via relation:

$$L = \frac{4\pi S D_L^2}{(1+z)^{1+\alpha}} \quad (2.1)$$

where D_L is the luminosity distance.

2.2 COSMOS field

The VLA-COSMOS 3 GHz Large Project (Smolčić et al. 2017a) was the deepest survey used in this work, with a detection limit at 5σ of $11.5 \mu\text{Jy beam}^{-1}$. The area of the survey equalled 2 deg^2 . We are referring here to the area covered also by the multiwavelength data, required in order to estimate the redshifts of the radio detected sources.

The matching of the radio catalogue with a multiwavelength catalogue, described in Smolčić et al. (2017), resulted in $\approx 93\%$ of the sources obtaining a counterpart (8035/8696 in the unmasked part of the field). From these sources, 7778 of them have a redshift estimate, 2740 being spectroscopic ($\approx 34\%$), and the remaining 5123 photometric. The details of the redshift estimation can be found in Delvecchio et al. (2017) and Smolčić et al. (2017). The mean spectral index of the survey was $\alpha = -0.73$. The spectral indices were obtained from cross-correlation with the 1.4 GHz Joint catalogue from Schinnerer et al. (2010). The details can be found in Smolčić et al. (2017a).

2.3 XXL-South field

One of the two intermediate surveys used in this work in order to bridge the gap between the deep and shallow surveys was the XXL-South field. The observations were performed with the Australia Telescope Compact Array (ATCA), at the frequency of 2.1 GHz (Butler et al. 2018a). The observations had a detection limit of $\approx 41 \mu\text{Jy beam}^{-1}$. The radio catalogue contains 6287 sources.

The radio catalogue was cross-correlated with a multi-wavelength catalogue containing data from near-infrared and optical up to X-ray data (see Fotopoulou et al. 2016). The matching of sources was performed via a likelihood technique described in Ciliegi et al. (2018). This resulted in 4770 sources having counterparts in the optical/NIR part of the spectra, of which 414 of them were also detected in the X-ray band. Furthermore, 12 of these sources were classified as stars, and were removed from the final catalogue, consisting of 4758 sources (Butler et al. 2018b). The catalogue contained 1110 spectroscopic redshifts and 3648 photometric redshifts. Generally, the photometric redshifts, obtained without measuring the spectra of the sources and identifying the emission lines, but instead relying on the brightness of a source observed through different filters and concentrating on broader features of the spectral energy distribution, is less reliable. It is however, easier to obtain, and usually sufficiently accurate. The details concerning the accuracy of the photometric redshifts and the overall redshift distribution of the sample can be found in Butler et al. (2018b).

The spectral indices were determined by using the additional Sydney University Molonglo Sky Survey (SUMSS) at 843 MHz (Bock et al. 1999) observing sources with peak flux density of 6 mJy. The median spectral index of the radio catalogue was estimated at $\alpha \approx -0.75$, where the bias arising from the high detection limit of the SUMSS survey was taken into account. The median spectral index of the final catalogue after cross-correlation with the multiwavelength catalogue is flatter and equals -0.45 (Butler et al. 2018b).

2.4 XXL-North field

The second intermediate field used in this work is the XXL-North field. Since the identification of source counterparts from the multi-wavelength catalogue was performed as a part of this thesis, we return to this data set in Ch. 3. The radio observations were performed at 610 MHz with the Giant Metrewave Radio Telescope (GMRT). The complete area of the field equalled 30.4 deg^2 , where the inner 11.9 deg^2 come from an earlier study by Tasse et al. (2007) and were re-reduced when the remainder of the survey was observed. The mean rms of the inner part

of the field is $200 \mu\text{Jy beam}^{-1}$, and of the outer $45 \mu\text{Jy beam}^{-1}$. The catalogue contains 5434 sources above a threshold of signal-to-noise ratio of $S/N \geq 7$.

The spectral indices of the sources were determined by using the NRAO Very Large Array Sky Survey (NVSS) at 1400 MHz (Condon et al. 1998). The details of this process are described in Smolčić et al. (2018). For the inner part of the field the mean spectral index equaled -0.65 , and for the outer it was -0.75 . Furthermore the catalogue contained 157 multi-component sources. We describe the methodology of selecting these sources in greater detail in Sect. 3.4, as it was performed within this thesis. The redshift information for this sample was obtained via cross-correlation with a multiwavelength catalogue from Fotopoulou et al. (2016). In order to use a catalogue of uniform depth we used only the subsample of the multiwavelength catalogue observed in the Spitzer Infrared Array Camera (IRAC) Channel 1 band at $3.6 \mu\text{m}$ (PI M. Bremer, limiting magnitude of 21.5 AB). The redshifts of the sources were calculated photometrically using the full multi-wavelength data. The process of cross-correlation is described in detail in Ch. 3. The IRAC survey did not cover the entire XXL-North radio field but roughly 80% of the field. We, furthermore removed the edges of the radio field which were considered to have too high noise. The area of the inner part of the field thus equalled 6.3 deg^2 , and the area of the outer part 14.2 deg^2 .

2.5 AGN subsamples

Since we are interested in constraining the LFs of AGNs, it was important to select a pure AGN sub-sample of our data set. Since the detection limits of the shallow 7C, 6CE and 3CRR fields were very high, it was safe to assume they consist purely of AGN, based on the source counts from Smolčić et al. (2017a), as later discussed in Sect. 4.2. For other fields of the composite survey, a further selection process was required.

A pure AGN sample of the XXL-North survey was obtained using the source counts from Smolčić et al. (2017a), by imposing a threshold in flux $> 1 \text{ mJy}$, imposed at 1400 MHz. Since at fluxes higher than the threshold the sample consists of purely AGN this is a conservative approach in obtaining an AGN sub sample. This process is described in detail in Sect. 4.2. Although sources with low flux are thus removed from further analysis this is not a problem since the XXL-North field is not the deepest field used in the composite survey. The fainter part of the complete sample, needed to model the LFs, was constrained with the deep COSMOS survey. By imposing a conservative threshold on the XXL-North survey we decided to prioritize the purity of this sample. The number of sources in the pure AGN catalogue was 292 for the inner part of the field, and 607 for the outer. The mean spectral index of the pure AGN sample

equalled -0.42 and -0.48 for the inner and outer parts of the field respectively.

For the XXL-South survey an analogous procedure was performed as for the XXL-North field. Although the classification of sources into AGNs and star forming galaxies (SFGs) is available in Butler et al. (2018b), we again decided to use a conservative threshold of > 1 mJy, since the fainter sources were constrained by the deep COSMOS survey. This resulted in an AGN sub-sample of 1484 sources. The mean spectral index of the AGN sub sample was -0.63 .

For the deep COSMOS field a different approach was needed in order to preserve the faint sources of the sample, since this survey was instrumental in constraining the faint end of the LFs. Following Smolčić et al. (2017) and Delvecchio et al. (2017), the AGN were selected by a ratio of radio emission compared to the star formation rate in the given galaxy, selecting sources that exhibit excess radio emission relative to that expected from the galaxy's star formation rate. The star formation rate was obtained from the infrared emission, computed via SED fitting, as described by Delvecchio et al. (2017). The number of sources in the pure AGN sub sample was 1916. The mean spectral index equalled -0.80 .

2.6 Composite survey

The aforementioned surveys were used together to constrain the LFs as a composite survey of varying area and depth. The summary of the complete sample can be found in Table 2.1. Together the composite survey reaches both high redshifts and luminosities as shown in the luminosity-redshift plot shown in Figure 2.2.

All of the radio catalogues used in this work (i.e. 7C, 6CE, 3CRR, XXL-North, XXL-South, COSMOS) are observed at radio wavelengths. However, the exact frequency varied across surveys. In order to make the data sets more coherent we recalculated all the fluxes to a common frequency of 1400 MHz assuming a standard power law shape of radio emission flux $S_\nu \propto \nu^\alpha$. The value of the spectral index is taken from the corresponding catalogue when it exists, or set to the mean value of that catalogue, as provided by the corresponding publications.

Table 2.1: The surveys used in the estimation of the LFs.

| Survey | Area[deg ²] | Original frequency [MHz] | Detection limit at 1400 MHz [mJy beam ⁻¹] | Number of sources (AGN) | Mean α (AGN) |
|-------------------|-------------------------|--------------------------|---|-------------------------|---------------------|
| 7C | 72.22 | 151 | 105 | 128 | -0.64 ± 0.27 |
| 6CE | 338.13 | 151 | 421 | 58 | -0.51 ± 0.32 |
| 3CRR | 13886.3 | 178 | 2,609 | 170 | -0.67 ± 0.24 |
| XXL-North (Inner) | 6.3 | 610 | 1.0 | 292 | -0.42 ± 0.49 |
| XXL-North (Outer) | 14.2 | 610 | 1.0 | 607 | -0.48 ± 0.57 |
| XXL-South | 25 | 2100 | 1.0 | 1484 | -0.63 ± 0.37 |
| COSMOS | 2 | 3000 | $1.15 \cdot 10^{-2}$ | 1916 | -0.80 ± 0.44 |

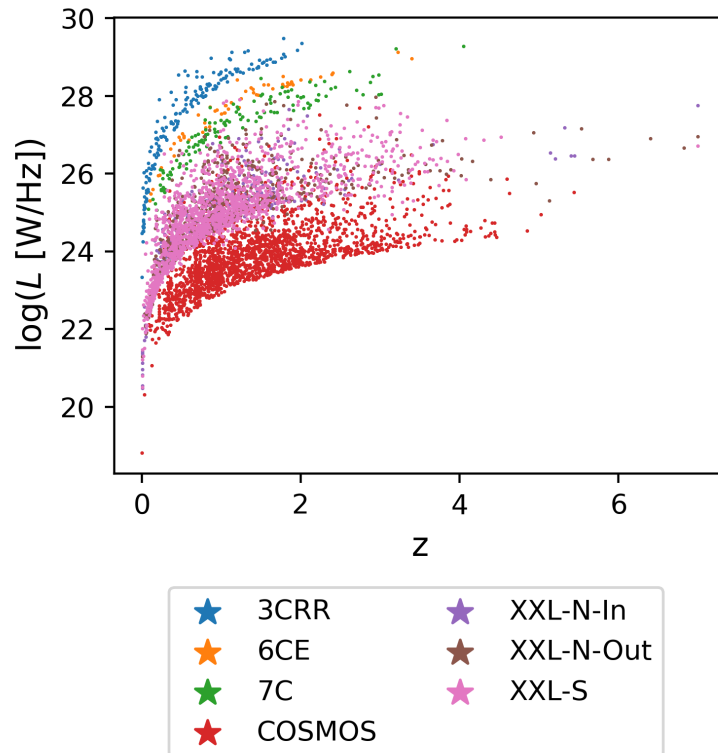


Figure 2.2: The redshift-luminosity plot of the complete composite sample, of radio AGNs used in this work. The names of the fields are denoted in the legend.

Chapter 3

XXL-North multiwavelength source matching

We now detail the cross-correlation between the radio XXL-North catalogue and the corresponding multi-wavelength data. We first describe in more detail the radio observations and the multi-wavelength data in Sect. 3.1 and 3.2, respectively. We then concentrate on the process of cross-correlation which was performed via a likelihood ratio method, incorporating both the positional and optical properties of the sources. First in Sect. 3.4, special care was also taken to assess the existence of multi component sources. The details of the cross-correlation are described in Sect. 3.5. The results of the cross-correlation is presented in Sect. 3.7. The work presented in this chapter was published in Smolčić et al. (2018) and Šlaus et al. (2020).

3.1 Radio data

The XXL-North field was observed in radio wavelengths with the GMRT, at the frequency of 610 MHz. The observations consisted of a mosaic of 79 pointings, spanning together an area of 30.4 deg^2 . The radio observations of the XXL-North field were divided into two distinct areas. The inner 36 pointings, or the XMM-Large Scale Structure, XMM-LSS field, were obtained from an earlier study by Tasse et al. (2007), and re-reduced by Smolčić et al. (2018). The inner part of the field has an area of 11.9 deg^2 and the mean rms of these observations was $200 \mu\text{Jy beam}^{-1}$. The outer parts of the field, spanning an area of 18.5 deg^2 , were observed by Smolčić et al. (2018). The mean rms of these observations was $45 \mu\text{Jy beam}^{-1}$. The FWHM of the synthesized beam across the entire field was 6.5 arcsec. Since the noise at the edges of the radio map was deemed too high (as defined in Smolčić et al. 2018), we removed them from further considerations. After this, the area of the inner part of the field equalled 6.3 deg^2 , and

the outer 14.2 deg².

The data reduction and imaging were performed by the Source Peeling and Atmospheric Modeling (SPAM) pipeline (Intema et al. 2009, Intema et al. 2017) and the source extraction was performed with the PyBDSF¹ software (Mohan & Rafferty 2015). Imposing a signal to noise ratio of $S/N \geq 7$, the radio catalogue consisted of 5434 sources. Of these sources some were components of multi-component sources. The identification of these sources is described in detail in Section 3.4 (and Šlaus et al. 2020). The spectral indices were estimated using the NVSS survey (Condon et al. 1998).

3.2 Multi-wavelength data

Apart from the aforementioned radio observations, the XXL-North field was observed in a wide range of other frequencies, spanning from radio to X-ray frequencies. In order to obtain a catalogue of uniform density and depth, in this work we used only the sub-sample of the catalogue which has identifications in the Spitzer IRAC Channel 1 band at 3.6 μm with a limiting magnitude of 21.5 AB.

It should be noted that the Spitzer IRAC 3.6 μm map does not cover the radio map completely. The overlap of the two maps can be seen in Figure 3.1. The area of the radio map covered by IRAC data is 8.0 deg.² (roughly 67%) for the inner part of the radio mosaic and 16.7 deg.² (i.e., roughly 90%) for the outer parts. This amounts to roughly 80% for the complete XXL-North field.

The redshifts of the sources come from the full multi-wavelength catalog, and were determined photometrically, as described in detail in Fotopoulou et al. (2016) and Fotopoulou & Paltani (2018). The accuracy of the photometrically determined redshifts z_{phot} was assessed by cross-correlation with the Sloan Digital Sky Survey Data Release 14 (SDSS DR14) and the database of spectroscopic follow-up redshift observations of the XXL survey (Adami et al. 2018), finding altogether 528 good quality spectra within 1 arcsec from the the GMRT counterpart. Based on comparison with this spectroscopic sample z_{spec} , the accuracy of the photometric redshifts reaches $\sigma_{NMAD} = 0.05$ with $\eta = 9.5\%$ catastrophic outliers. Here, the accuracy is defined as $\sigma = 1.48 \frac{|z_{phot} - z_{spec}|}{1 + z_{spec}}$ and the number of catastrophic outliers is the fraction of sources with $N[\frac{|z_{phot} - z_{spec}|}{1 + z_{spec}}] > 0.15$. The plot comparing spectroscopic and photometric redshifts can be seen in Figure 3.2.

¹<https://www.astron.nl/citt/pybdsf/>

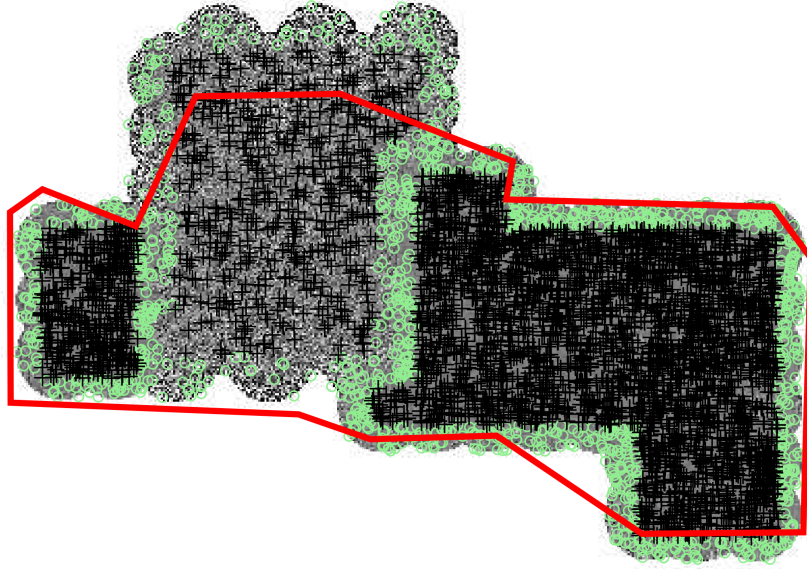


Figure 3.1: Overlap of Spitzer IRAC 3.6 μm coverage with the the XXL-North field. The gray map corresponds to the GMRT 610 MHz mosaic, while the red region denotes the area covered by IRAC data. The sources in the radio catalogue are denoted by green circles and black crosses. Sources marked by green symbols correspond to the noisy edges, removed from further consideration, as described in the text. Note that the Spitzer IRAC 3.6 μm data do not cover the northern part of the central XXL-North field. However, the number of radio sources there is lower.

3.3 Astrometric correction

Since the radio observations and multiwavelength catalogue arise from different observations, there can be a systematic offset between the positions of sources. Prior to performing the cross-correlation, this offset was assessed. A simple match between the two surveys was performed, based solely on the positions of the sources, selecting sources whose positional offset is 1 arcsec or less. Here we choose a conservative separation threshold since we are not interested in the completeness of the resulting sample, but only its purity. In order to further minimise the number of spurious counterparts we limited the GMRT radio sample to only unresolved sources with signal-to-noise ratio of $S/N > 10$. The resulting matches were thus considered very reliable. The mean positional offset between the GMRT and the IRAC positions of the

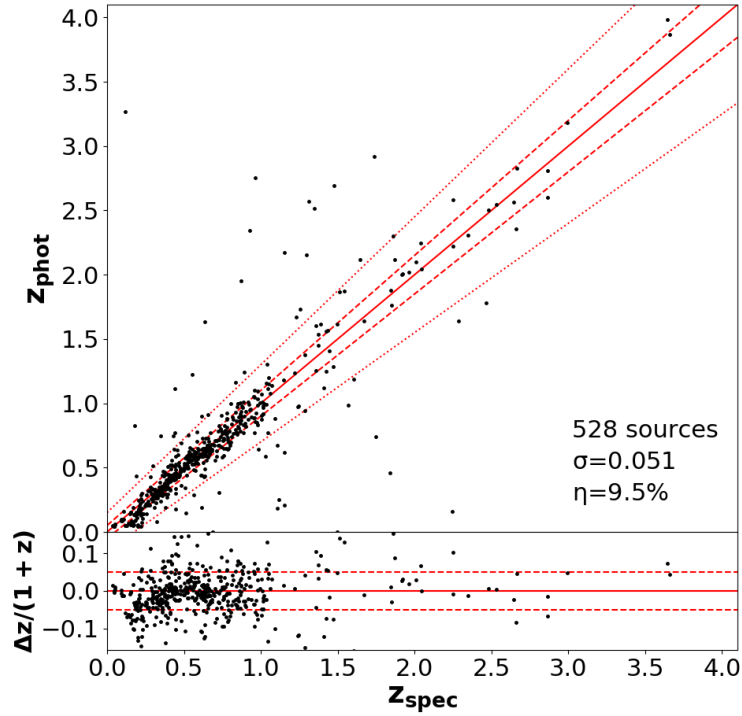


Figure 3.2: Comparison between the spectroscopic (z_{spec}) and the photometric (z_{phot}) redshifts for 528 sources with good quality spectra. For the definition of accuracy σ and the percentage of catastrophic outliers η , see the text. The bottom panel shows the renormalized accuracy, defined as denoted on the y-axis of the bottom panel. The solid red line shows the one-to-one relationship, while the dashed and dotted lines correspond to $z_{\text{phot}} = 0.05 \cdot (1 + z_{\text{spec}})$ and $z_{\text{phot}} = 0.15 \cdot (1 + z_{\text{spec}})$, respectively.

matched sources, in the RA and DEC coordinates were

$$\overline{\Delta RA} = (0.02 \pm 0.03) \text{ arcsec}, \quad (3.1)$$

$$\overline{\Delta DEC} = (0.07 \pm 0.02) \text{ arcsec} \quad (3.2)$$

for the inner (XMM-LSS) part of the GMRT mosaic, and

$$\overline{\Delta RA} = (0.104 \pm 0.008) \text{ arcsec}, \quad (3.3)$$

$$\overline{\Delta DEC} = (0.02 \pm 0.01) \text{ arcsec} \quad (3.4)$$

for the outer part. The offset was eliminated by correcting the relative separation of sources during the cross-correlation. The plot showing the offset in source positions for the outer part of the field can be seen in Figure 3.3.

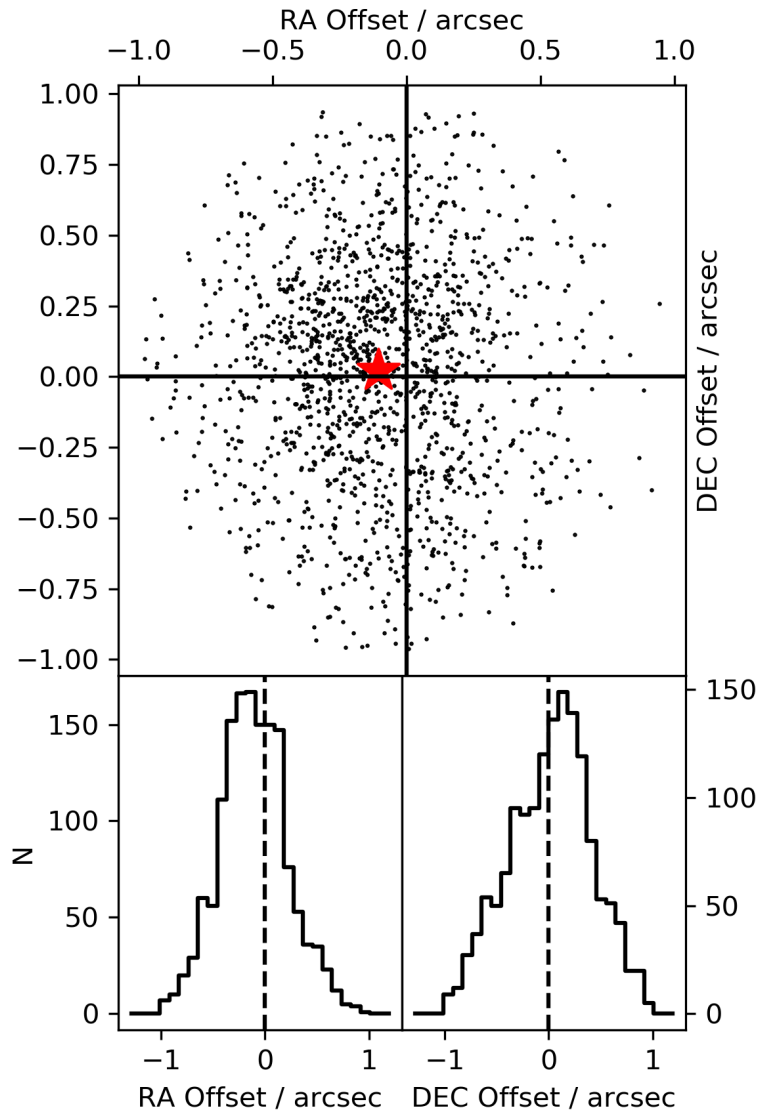


Figure 3.3: Positional offsets between the GMRT and IRAC surveys for the outer part of the XXL-North field. The mean offset is denoted by a red star. The histograms in the bottom panels represent the distribution of offsets in the RA and DEC directions. The inner part of the XXL-North field produces a similar plot. The mean offsets for the two parts of the field are given in relations 3.1- 3.4.

3.4 Multi component sources

Due to the limit in surface brightness sensitivity of radio surveys, if a source exhibits complex morphologies it may be catalogued incorrectly as multiple distinct objects, instead of a single object (Schinnerer et al. 2004, Schinnerer et al. 2007, Smolčić et al. 2017a). This effect will lead to obvious errors during the cross-correlation of the radio catalogue with the multi-wavelength data. In order to eliminate this error, these components must be joined into a single object. Following Tasse et al. (2006) a pre-selection of possible multi-component sources was performed by using their relative position. Sources whose separations were less or equal to 60 arcsec were considered to possibly be components of multi-component sources. Furthermore, invoking the size-flux relation (Bondi et al. 2003), where larger sources emit more flux, an additional flux limit was introduced for the outer parts of the XXL-North field, where only sources of $S_{610 \text{ MHz}} > 1.4 \text{ mJy}$ were considered. These pre-selected sources were then further inspected visually.

The process of visual inspection was performed by using the publicly available Multi-Catalog Visual Cross-Matching (MCVCM) package². The program produces IRAC 3.6 μm cut-outs of each investigated radio source overlaid with radio contours. The radio lobes and cores, as well as the infrared counterpart were then selected manually. An example of the figures produced by the MCVCM program can be seen in Figure 3.4. The visual classification resulted in 381 components being classified as belonging to multi-component sources. The components were joined into single sources by having their radio fluxes summed and their positions taken to be that of the IRAC (infrared detected) centroid source. This resulted in 157 multi-component sources. Since these sources were matched with the multi-wavelength catalogue manually, they were excluded from further matching via the likelihood ratio method, described in the following sections. The pre-selection process, although generally reliable, missed six conspicuous multi-component sources due to the excessive size of these objects (more than 60 arcsec), which were visible clearly from the radio map. They were therefore re-matched manually, using again the MCVCM program.

3.5 Likelihood ratio cross-correlation

In order to perform a cross-correlation between the GMRT XXL-North 610 MHz radio catalogue and the IRAC survey sources, we used a method that takes into account both the source positions and their magnitudes. Namely we used the likelihood ratio (*LR*) method (Sutherland

²<https://github.com/kasekun/MCVCM>

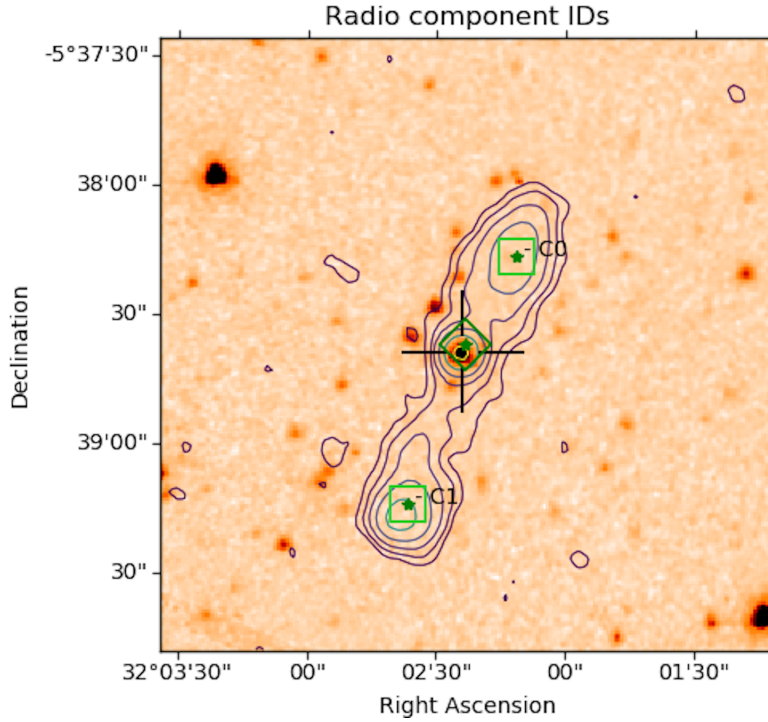


Figure 3.4: Example of a multi-component source inspected visually via the MCVCM program. The radio contours, chosen as $2^n \times \text{RMS}$, $n = 1, 2, 3, \dots$, are overlaid on top of the IRAC image. The radio lobes and cores and the IRAC counterpart are selected manually. The dark green rhomboid denotes the radio core position, and the light green squares denote the center of the radio lobes. The black crosshair denotes the IRAC counterpart.

& Saunders 1992; see also de Ruiter et al. 1977, Ciliegi et al. 2003, Brusa et al. 2007, Mainieri et al. 2008, Smith et al. 2011, Bonzini et al. 2012, McAlpine et al. 2012, Fleuren et al. 2012, Kim et al. 2012). Here we talk only about the single component sources, as the multi-component sources were matched manually, as described in the last section. The LR of each possible match is defined via the probability ratio between the source being a true counterpart and it being an unrelated background object. If we assume that the positional offsets between sources are independent of their optical properties (Sutherland & Saunders 1992, Ciliegi et al. 2003), this probability can be expressed as:

$$LR = \frac{f(r)q(m)}{n(m)}, \quad (3.5)$$

Factor $f(r)$ denotes the probability distribution of the positional offsets between the surveys. The expected magnitude distribution of true counterparts is denoted by $q(m)$. The factor $n(m)$ in the denominator denotes the surface density of the unrelated background objects, as a func-

tion of magnitude. The magnitudes in the above expression refer to the IRAC 3.6 μm magnitudes, i.e. the magnitudes of the possible counterparts of the radio sources. In the following sections we describe the methods used to determine each one of these three factors.

3.5.1 Deriving $f(r)$

The radial probability distribution of the positional offsets was parametrised by a Gaussian function (Ciliegi et al. 2003, Smith et al. 2011, Bonzini et al. 2012, McAlpine et al. 2012, Fleuren et al. 2012, Kim et al. 2012)

$$f(r) = \frac{1}{\sqrt{2\pi\sigma^2}} \exp\left(-\frac{r^2}{2\sigma^2}\right), \quad (3.6)$$

The separation between the source positions of the two surveys, GMRT 610 MHz and the IRAC 3.6 μm , is denoted by r . Factor σ denotes the standard deviation of the Gaussian distribution. We determined this factor from the positional uncertainties of both surveys σ_{GMRT} and σ_{IRAC} . Following Ciliegi et al. (2003) we defined it as

$$\sigma = \sqrt{\sigma_{IRAC}^2 + \sigma_{GMRT}^2}. \quad (3.7)$$

The uncertainties of the GMRT field were determined by using positional errors listed in the radio catalogue, that were provided by PyBDSF. The mean value of these errors was around 0.2 arcsec for both parts of the XXL-North field, and both the RA and DEC coordinates. The positional uncertainties of the IRAC field were calculated following Ivison et al. (2007) and Furlanetto et al. (2018), from the full width at half maximum (FWHM) of the IRAC 3.6 μm beam and the signal-to-noise ratio of each corresponding source (S/N) as

$$\sigma = 0.6 \frac{FWHM}{S/N}. \quad (3.8)$$

Furthermore, as discussed in Smith et al. (2011) we took into account the existence of a minimum positional uncertainty. The errors were therefore not allowed to be smaller than 0.2 arcsec, or roughly one-third of the mean positional error which was about 0.6 arcsec. The anisotropies in the positional errors were also taken into account by calculating σ separately in the RA and DEC directions. The final value of the uncertainty was taken to be the mean value between the two. Lastly, although $f(r)$ is normalized to unity for radii spanning to infinity, in practice a fixed value of maximum radius must be set during the cross-correlation. In this work, the maximum allowed separation R , called the matching radius, was set to 4 arcsec.

3.5.2 Deriving $n(m)$

The surface density of the unrelated background objects $n(m)$ was estimated by using the magnitude distribution of the complete IRAC 3.6 μm catalogue and normalising it by the area of the IRAC 3.6 μm survey (Smith et al. 2011, Furlanetto et al. 2018). Here we assume that the shape of the background magnitude distribution is equal to the shape of the magnitude distribution of the complete IRAC catalog. This approximation is accurate since the number of real identifications is much smaller than the total number of IRAC sources.

Furthermore, we assume that the circles defined by the matching radius R do not overlap. This is a good approximation since the number of radio sources in the catalogue is small. Within the area defined by the matching radius R around each radio source, we therefore have an average number of unrelated background objects given by

$$false(m) = n(m) \cdot N_{Radio} \cdot \pi R^2, \quad (3.9)$$

Here N_{Radio} is the number of radio sources, corresponding only to the sources within the area covered by both GMRT XXL-North 610 MHz and IRAC surveys, or roughly 80% of the area of the radio mosaic, as described in Sect. 3.2.

3.5.3 Deriving $q(m)$

The expected distribution of true counterparts, $q(m)$ was estimated by creating the magnitude distribution of the total number of possible counterparts within the matching radius $R = 4$ arcsec, which we refer to as $total(m)$. Since this distribution also contains the false counterpart identifications arising from unrelated background sources ($false(m)$, eq. 3.9), following Ciliegi et al. (2003), we constructed a new distribution, $real(m)$, as the difference between the total and the background distributions

$$real(m) = total(m) - false(m). \quad (3.10)$$

This distribution corresponds therefore to the excess of sources compared to the background distribution, or in other words the expected real identifications. The distribution was further normalised as

$$q(m) = \frac{real(m)}{\sum_m real(m)} \cdot Q, \quad (3.11)$$

The sum in the denominator sums the $real(m)$ distribution over magnitudes. The Q factor denotes the fraction of true counterparts above the magnitude limit (Smith et al. 2011), or in other words, it is a correction for the limiting magnitude of our observations. It was determined by summing the $real(m)$ distribution and dividing it by the number of radio sources present in the intersection of the fields

$$Q = \frac{\sum_m real(m)}{N_{Radio}}. \quad (3.12)$$

The value of Q equalled 0.62 for the outer part of the XXL-North field and 0.55 for the inner. However, the value of Q does not affect the results of the cross-matching significantly, as already noted by earlier studies (Ciliegi et al. 2003, Franceschini et al. 2006, Fadda et al. 2006, Mainieri et al. 2008).

3.6 The blocking effect

A further complication that needs to be discussed is the blocking effect, discussed by Brusa et al. (2007), Smolčić et al. (2017) and Ciliegi et al. (2018). Because of the tendency of radio sources to have bright counterparts, some of the fainter IRAC sources around these bright infrared counterparts remain undetected. In other words, the faint IRAC sources are blocked by the bright ones, which is the reason for the name of this effect. As we calculated the total number of counterparts within the matching radius around the radio positions, this effect leads to an underestimation of the $total(m)$ magnitude distribution. On the other hand, the background density distribution $n(m)$ is obtained from the complete IRAC catalogue. Since the number of bright sources in the complete catalogue is small, the background density distribution is not significantly affected by the blocking effect. Together this leads to a scenario where at faint magnitudes the $real(m)$ distribution becomes underestimated and even assumes nonphysical negative values. This can be seen in the upper panels of Fig. 3.5 which shows the magnitude distributions during the cross-correlation. The blocking effect is sketched schematically in Fig. 3.6.

In order to eliminate this effect and account for the missing sources, following Brusa et al. (2007) and Ciliegi et al. (2018) we re-estimated the magnitude distribution of the unrelated background sources. We selected a random sample of 5000 sources from the IRAC catalogue that followed the same magnitude distribution as the $total(m)$ counterparts. We used these sources as a mock radio catalogue and re-counted the remaining IRAC sources in their vicinity, within a radius of $R = 8$ arcsec. We further re-normalised this number to the number of radio

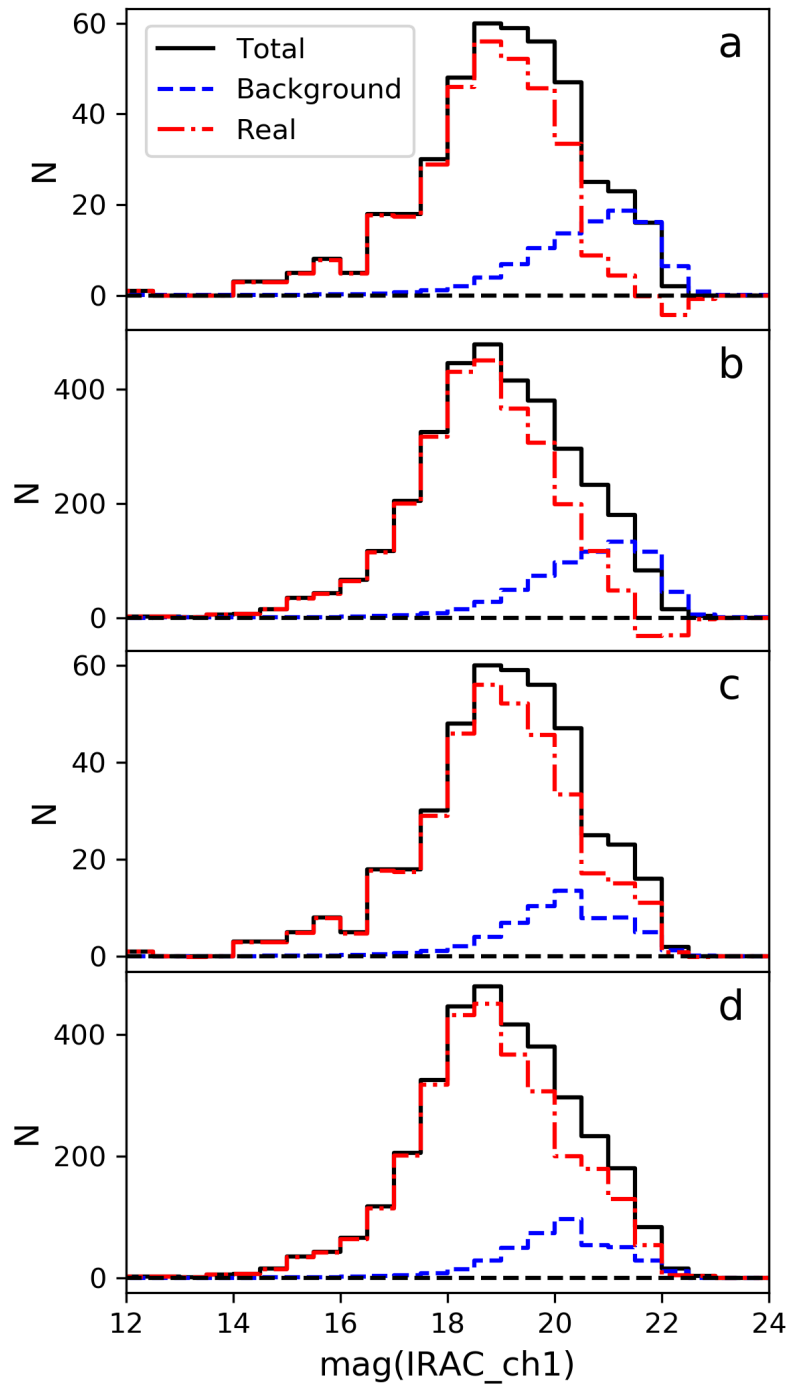


Figure 3.5: Magnitude distribution of sources during the cross-correlation. The black, blue, and red lines denote the total, background, and real sources, respectively, as described in the text. The two upper histograms (panels *a* and *b*, for the inner and outer part of the field, respectively) correspond to the match where the blocking effect is present. Correction for blocking effects mitigates the issue of negative counts. The two bottom histograms (panels *c* and *d*, for the inner and outer part of the field, respectively) are the magnitude distributions after the blocking effect has been accounted for.

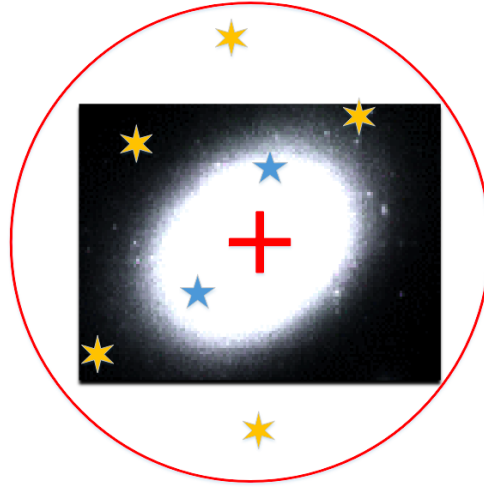


Figure 3.6: Visual representation of the blocking effect. The red circle represents the radius around the bright counterpart source (denoted as a white blob) used for calculating $total(m)$. The background sources are represented by stars. The yellow stars are detected, while the blue remain undetected due to being blocked by the bright source. The $total(m)$ magnitude distribution is therefore underestimated, as described in the text. Taken from Ciliegi et al. (2018).

sources and the correct matching radius with

$$\frac{N_{Radio} \cdot \pi \cdot (4\text{arcsec})^2}{5000 \cdot \pi \cdot (8\text{arcsec})^2}, \quad (3.13)$$

The resulting distribution was the new estimate for the background magnitude distribution. This distribution by definition included the blocking effect present within the IRAC catalog. In other words, since the new background density was also calculated around other bright IRAC sources, it is no longer overestimated compared to the number of total counterparts $total(m)$. This difference in magnitude distributions is noticeable at faint magnitudes. As seen in Figure 3.5, the new background distribution was consistent with the global one for bright magnitudes, but differed strongly for faint magnitudes. We therefore applied the correction only at faint magnitudes. At bright magnitudes, down to a fixed limit of $m_{AB} = 20.5$ in IRAC magnitudes, we used the global background distribution, while at fainter magnitudes we used the new estimation of the background distribution, which accounts for the blocking effect. The new background distribution estimation resulted in a larger number of faint identifications being considered real.

3.7 Results of the cross-correlation

Having estimated all the factors of the probability given in relation 3.5, following the literature (e.g., Mainieri et al. 2008 or Ciliegi et al. 2018), we considered only identifications with $LR > 0.2$ as correct. A further complication arises from sources with multiple identifications. Therefore we also defined the reliability of each match as (e.g., Franceschini et al. 2006, Fleuren et al. 2012, Butler et al. 2018a)

$$Rel_i = \frac{LR_i}{\sum_i LR_i + (1 - Q)}, \quad (3.14)$$

Here Q is given again by equation 3.12. In case of multiple identifications with $LR > 0.2$ we chose the counterpart with the largest reliability as being correct (Mainieri et al. 2008, Butler et al. 2018a). This process resulted in a catalogue of 3336 radio sources, with Spitzer IRAC $3.6 \mu\text{m}$ identifications. We further excluded sources lying on the noisy edges of the radio (Fig. 3.1) map as the RMS noise there was considered too high. The noisy edges were defined manually, as described by Smolčić et al. (2018) via the noise distribution presented in Fig. 5 in that paper.

The final matched catalogue, containing both the visually matched multi-component sources and the single-component sources matched via likelihood ratio, consisted of 2785 sources in total. Of these, 2467 sources were in the outer part of the XXL-North field and 318 in the inner. Altogether, this corresponds to roughly 60% of the radio sources in the intersection between the radio and IRAC fields being matched. If we compare only the sources in the area without the noisy edges, the percentage rises to 67%, which is in agreement with the literature for similar surveys (e.g., Ciliegi et al. 2018). All of the matched sources had a reliable photometric redshift estimation. The number of matched sources after each step described in the last sections is summarised in Table 4.1.

Chapter 4

XXL-North LFs

We created the LFs of the XXL-North survey via the non-parametric method of maximum volumes. In Sect. 4.1 we describe the incompleteness arising from the matching process and the required correction. In Sect. 4.2 we detail the AGN selection process. The non-parametric method of maximum volumes is described in Sect. 4.3, and the resulting LFs are presented and discussed in Sect. 4.6 and 4.7. The consistency of these results with the broader physical picture is described in Sect. 4.8. The work presented in this chapter was published in Šlaus et al. (2020).

4.1 Missing counterparts

In order to determine the LFs of the XXL-North sample correctly, we had to assess the effect of the finite depth of the IRAC data on the completeness of our sample. Since the IRAC data used in this work are of medium depth ($m_{AB} = 21.5$) a number of sources were lost during the cross-correlation. This deficit of sources is a function of redshift. In order to examine this effect, we used deeper radio data from the VLA-COSMOS 3 GHz Large Project, detected above a 5σ threshold of $11.5 \mu\text{Jy}$ (Smolčić et al. 2017). The 3 GHz data was cross-matched with the multi-wavelength COSMOS2015 catalog, containing Channel 1 IRAC sources (Laigle et al. 2016), resulting in $\approx 93\%$ of radio sources having a counterpart (see Smolčić et al. 2017 for details). In order to mimic our radio data-set before the process of cross-correlation, we imposed a threshold in flux density on the deeper COSMOS2015 data, equivalent to our radio detection limit. The detection limit of our survey ($350 \mu\text{Jy}$) was shifted to COSMOS frequencies by assuming a power law and a mean spectral index of -0.7 . Furthermore, this threshold ensures that this subsample of COSMOS sources is complete over all redshifts studied with our data ($0.1 < z < 2.1$; see Fig. 16. from Smolčić et al. 2017a or Fig. 1. from Delvecchio et al. 2017

for details). We then took this data-set and imposed another threshold in the Channel 1 IRAC fluxes, corresponding to the IRAC detection limit of our survey. This second data-set mimics our data after the cross-correlation with the IRAC data. By comparing the redshift histograms of these two data-sets, we were able to estimate the sources lost during the cross-matching.

The comparison of the histograms, shown in Figure 4.1, quantifies the redshift dependency of the sources lost during the cross-correlation. The bottom panel of the figure shows the ratio of the two histogram distributions, and should be considered the necessary correction required to be taken into account while constructing the LFs: $C_{IRAC}(z)$. For the standard deviation shown in the figure we assumed the Poissonian deviation, which scales with the number of sources as \sqrt{N} , except when the number of sources in the corresponding histogram bin was lower than $N = 10$. Then we used the deviation approximation for the upper limit error bars from Gehrels (1986), and calculated the standard deviation as $N + \sqrt{N + 0.75}$. Here we assumed that the error bars were symmetrical, which was a good enough approximation for our needs. Using the information presented in this plot we noticed that around redshift of 3 the fraction of sources drops to values of ≈ 0.5 and the uncertainties become comparable with the values of the fraction. Therefore, we used only sources with $z \leq 2.1$ for the construction of the XXL-North LFs, choosing to adopt a conservative threshold where the data sets are mostly complete.

4.2 AGN sample

Since we were interested in determining the AGN LFs of the XXL-North sample, we selected a purely AGN sub-sample of our data. In order to assess the fraction of galaxy populations that constitute our sample, we used again the VLA-COSMOS 3 GHz catalogue described in Smolčić et al. (2017). Here we neglect the effects of cosmic variance, or in other words we assume that the fraction of galaxy populations from one survey is comparable to other surveys. As they are a good tracer of AGNs in the radio regime, we concentrated on the radio-excess sources described in Smolčić et al. (2017). The sources were considered radio-excess sources when their radio luminosity $L_{1.4 \text{ GHz}}$ exceeded an extracted star formation rate luminosity given by $\log(L_{1.4 \text{ GHz}}/\text{SFR}_{\text{IR}}) = 21.984(1+z)^{0.013}$. Here the star formation rate was determined by SED fitting, from the total IR emission as described in Delvecchio et al. (2017).

In Figure 4.2 we plot the source counts of sources with and without radio-excess emission. We also show the fraction of radio-excess sources. By using the cumulative fraction given in Fig. 4.2, we determined that at $7\sigma = 350 \mu\text{Jy}$, which is the lowest detection limit of our survey, we have a sample that consists of more than 98% AGN. We therefore concluded that our sample as a whole consists mostly of AGN. The differential fraction however, showed that the fainter

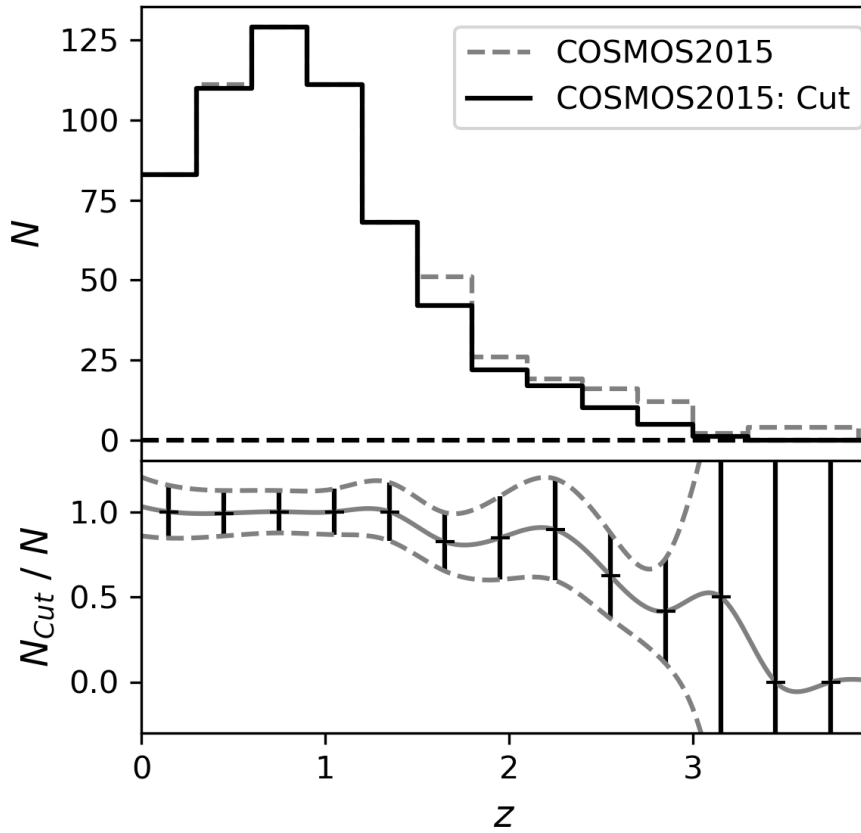


Figure 4.1: Upper panel: Redshift histograms of the COSMOS2015 catalogue with only the radio cut (dashed gray line) and the histogram with an additional cut in the infrared flux corresponding to the IRAC detection limit of our survey (black line). Bottom panel: Ratio of these two histograms and the corresponding standard deviation. A cubic interpolation has been performed on both the data points and the error bars.

bins contained a non-negligible fraction of star forming galaxies. In order to obtain a pure AGN sample at all fluxes, we imposed a threshold in flux, limiting our sample only to sources with $S_{610 \text{ MHz}} > 1 \text{ mJy}$. This threshold is a bit less conservative than the one performed for the XXL-North field in Sect. 2.5, when it was considered a part of the composite field, and the threshold was imposed at 1400 MHz. The number of sources in the catalogue thus equalled 1266 (see Table 4.1).

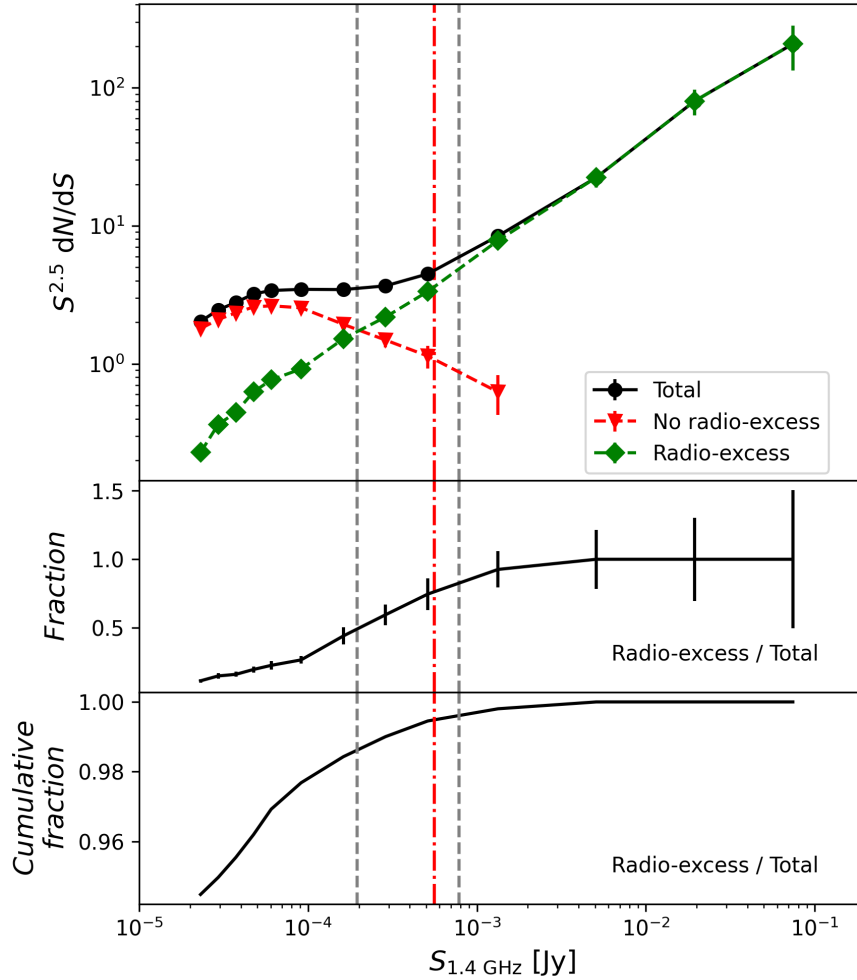


Figure 4.2: Top panel: Euclidean-normalized and completeness-corrected source counts for different galaxy populations at 1.4 GHz reproduced from Smolčić et al. (2017), as described in the text. Symbols are indicated in the legend. The vertical gray lines correspond to the 7σ detection limits of the inner and outer part of the XXL-North GMRT survey recalculated from 610 MHz by presuming a power law for the radio emission and a spectral index of -0.7 . Middle panel: Fraction of the radio-excess population. Lower panel: Cumulative fraction of the radio-excess population summed from higher fluxes towards lower. The red dot-dashed line denotes the adopted flux threshold described in the text.

Table 4.1: Number of sources, and corresponding area, after each step performed during the analysis and LF creation, as described in the text. The steps are performed progressively, or in other words, each step also includes the previous ones.

| Outer part of the XXL-North field | | | |
|---------------------------------------|-------------------------|----------|------------|
| Step | Area[deg ²] | N(Radio) | N(Matched) |
| Complete catalogue | 18.5 | 4615 | (...) |
| IRAC coverage | 16.7 | 4241 | 2954 |
| Far from edge | 14.2 | 3499 | 2467 |
| $S_{610 \text{ MHz}} > 1 \text{ mJy}$ | 14.2 | 1605 | 948 |
| $z \leq 2.1$ | 14.2 | (...) | 855 |

| Inner part of the XXL-North field | | | |
|---------------------------------------|-------------------------|----------|------------|
| Step | Area[deg ²] | N(Radio) | N(Matched) |
| Complete catalogue | 11.9 | 819 | (...) |
| IRAC coverage | 8.0 | 596 | 382 |
| Far from edge | 6.3 | 477 | 318 |
| $S_{610 \text{ MHz}} > 1 \text{ mJy}$ | 6.3 | 477 | 318 |
| $z \leq 2.1$ | 6.3 | (...) | 295 |

4.3 XXL-North LFs creation

The LFs of the radio GMRT 610 MHz observations of the XXL-North field were constructed using a non-parametric method. The method is based on calculating the maximum observable volume for each observed source (see Schmidt 1968, Felten 1976, Avni & Bahcall 1980, Page & Carrera 2000, Yuan & Wang 2013 and Novak et al. 2017). In short, since the data set is limited by the detection limit of the radio observations, the more luminous sources are detectable over larger distances (Page & Carrera 2000). This introduces a bias in the sample which needs to be taken into account. First we determined the maximum volume in which each source could have possibly been observed given the detection limit of our survey, $V_{Max,i}$. We then divide the complete sample into redshift and luminosity bins. The LF is estimated for each bin, corresponding to one data point in the final graph. For each luminosity and redshift bin, the value of the LF $\Phi(L, z)$ was calculated as a sum of the inverse maximum volumes

$$\Phi = \frac{1}{\Delta \log(L)} \sum_i \frac{1}{V_{Max,i}} \quad (4.1)$$

where $\Delta \log(L)$ is the width of each luminosity bin. The reasoning here is that for a sample of completely uniform space density, the mean value of volumes defined by the real source

positions divided by the maximum volumes of possible observation $\langle V/V_{Max} \rangle$ should equal 1/2. A difference in this value points towards a difference in source density. Therefore each source summed in the calculation of the LFs is weighted by a factor of $1/V_{Max}$.

The standard deviation of each LF data point was determined assuming Gaussian statistics (Marshall 1985, Boyle et al. 1988, Page & Carrera 2000, Novak et al. 2017) as

$$\sigma = \frac{1}{\Delta \log(L)} \sqrt{\sum_i \frac{1}{V_{Max,i}^2}} \quad (4.2)$$

This formula is not applicable to bins with very few sources. For bins with less than 10 sources, we therefore used the tabulated errors determined by Gehrels (1986).

The calculation of $V_{Max,i}$ is performed in practice by determining first the luminosity of each source. Since the luminosity is the physical property of the source itself, it does not change as the redshift of the source is varied. For each source, we therefore calculated the flux that would have been observed for different varying redshifts. The redshift at which the source would no longer be visible determined the maximum volume. In practice this was performed numerically by varying the redshift in small but discrete steps. Furthermore, if the maximum volume exceeded the volume defined by the redshift bin, then the upper limit of the bin was used to determine V_{Max} .

During the calculations the spectral index was set to a fixed value of $\alpha = -0.7$, which is consistent with the mean value for our survey (Smolčić et al. 2018). The LFs were also scaled to the area of observations A by introducing a factor of $A/41\,253 \text{ deg}^2$, where the denominator is the area of the complete celestial sphere.

4.4 Corrections

During the calculation of maximum volumes, it is necessary to take into account the biases of the survey and to correct them with appropriate corrections. Firstly, we accounted for the finite IRAC data set depth. This effect was discussed already in Section 4.1. The correction that accounts for the sources lost during the cross-matching of the radio catalogue with the IRAC data is a function of redshift. We denote it with $C_{IRAC}(z)$.

A second bias arises from the noise present in the radio map of the XXL-North field. The local value of noise is not completely uniform but varies across the observed map. Since the sources were selected, during catalogue creation, via flux compared to the mean value of noise (with $S/N > 7$), it follows that the flux densities of some true sources can fall below the detection limit. To correct this incompleteness, we again used observations from a deeper survey,

namely the VLA-COSMOS 3 GHz Large Project (Smolčić et al. 2017a) and compared the source counts of the two surveys. The procedure is described in detail in Smolčić et al. (2018). This provided us with the required correction, now a function of radio flux, which we denote as $C_{Radio}(S_{610 \text{ MHz}})$.

The total correction applied to the GMRT-XXL radio data matched to IRAC counterparts, was calculated as the product of two aforementioned corrections (Novak et al. 2017)

$$C_{Total} = C_{IRAC}(z) \times C_{Radio}(S_{610 \text{ MHz}}), \quad (4.3)$$

The values of $C_{IRAC}(z)$ are shown in Fig. 4.1, while the values of $C_{Radio}(S_{610 \text{ MHz}})$ are shown in Fig 13. from Smolčić et al. (2018). The values of maximum volumes V_{Max} were multiplied by this number and scaled to the area of observations, as described in the last section. We also imposed redshift ($z \leq 2.1$) and flux density thresholds ($S_{610 \text{ MHz}} > 1 \text{ mJy}$) described in Sects. 4.1 and 4.2.

4.5 Bin selection

In order to create the LFs via the maximum volume method it was necessary to select the bins in luminosity and redshift, corresponding to each data point. However, as pointed out by Yuan & Wang (2013), if the bins are selected arbitrarily, this can lead to potential systematic errors. The bias is caused by the detection limit of the survey. Because of this limit, there can be low-luminosity bins which enclose a very small number of sources. Apart from the problems associated with small number statistics, the factor $[V_{Max} \Delta \log L]$, present in the calculation of the LFs, leads to an underestimation of $\Phi(L, z)$. Following Yuan & Wang (2013), this effect was reduced by choosing the luminosity bins so that they start from the value determined by the detection limit. In other words, for each redshift bin, the luminosity bins are set to start from the line defined by the detection limit. This way the systematic errors were minimised. The final bins in redshift and luminosity are shown via the luminosity-redshift plot in Figure 4.3.

4.6 LFs of the XXL-North field

The resulting LFs of the XXL-North field are shown in Figure 4.4. The functions are plotted for redshifts ranging from $z = 0.1$ up to $z = 2.1$. In order to compare the LFs with the literature, we plotted the LFs at rest-frame frequency of 1.4 GHz. This was done by assuming a power-law radio flux spectrum, and a spectral index of -0.7 . The sampled luminosity range depends on the

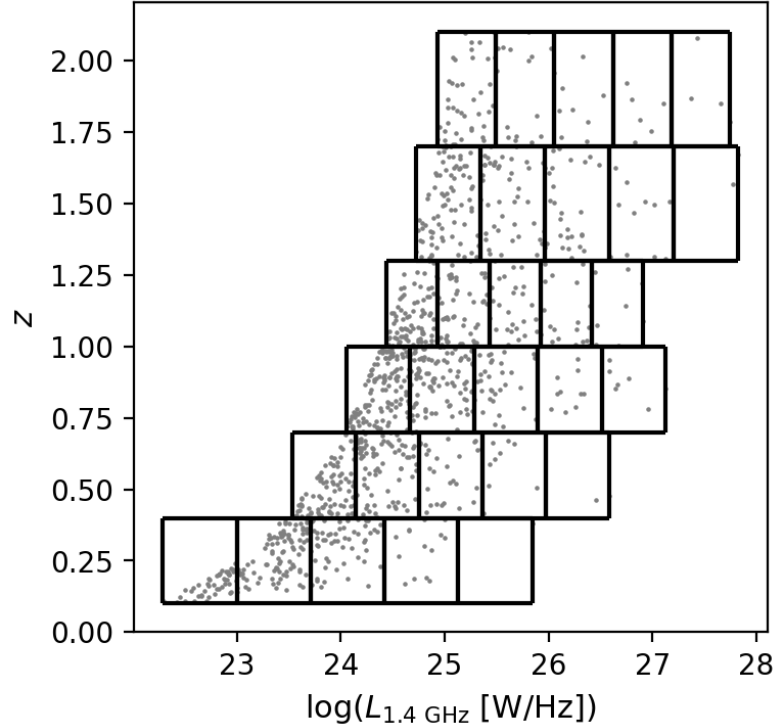


Figure 4.3: Visual representation of the bins used in the creation of the LFs. The gray dots represent the sources. The black lines correspond to the bin limits in redshift and luminosity. The absence of low-luminosity bins with only few sources is clearly visible. On the high-luminosity end the number of sources per bin decreases, but this effect is a consequence of the intrinsic lower density of high-luminosity sources and cannot be easily corrected.

corresponding redshift bin, with the maximum luminosities approaching $L_{1.4 \text{ GHz}} = 10^{28} \text{ W/Hz}$, as seen from the figure.

4.7 Comparison with the literature

Apart from the LFs created from the XXL-North radio data, in Fig. 4.4 we also show the LFs from other surveys from the literature, in order to compare them.

The radio LFs by Sadler et al. (2007) were derived from the volume-limited sample of 391 radio galaxies with the optical spectra from the 2dF-SDSS (Sloan Digital Sky Survey) LRG (Luminous Red Galaxy) and QSO (quasi-stellar object) surveys (2SLAQ; Cannon et al. 2006)

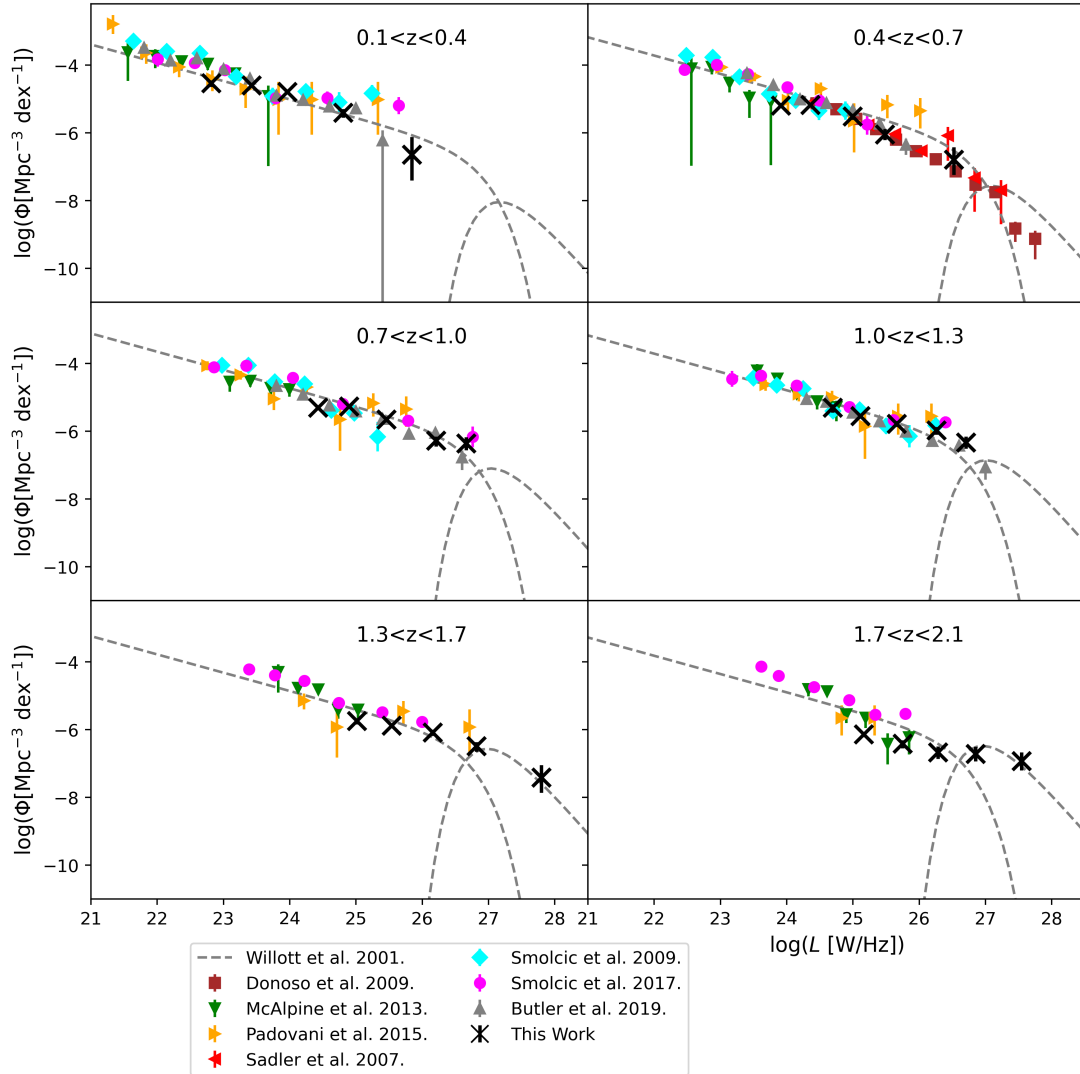


Figure 4.4: LFs of this work along with previous ones at 1.4 GHz, as denoted in the legend. The dashed lines represent the bimodal model discussed in the text. This model consists of a high- and a low-luminosity end with different functional dependencies. It can be seen that at higher luminosities, the high-luminosity end of the model traces the data points well.

with Faint Images of the Radio Sky at Twenty centimetres (FIRST; Becker et al. 1995) and the NVSS radio coverage over redshifts $0.4 < z < 0.7$. The authors found that the radio emission in these sources most likely arises from AGN activity, rather than star formation.

The radio LFs by Donoso et al. (2009) were derived from a sample of 14453 radio-loud (RL) AGN at redshifts $0.4 < z < 0.8$ detected at the frequency of 1.4 GHz with NVSS and FIRST radio surveys. The data set was previously cross-matched with the MegaZ-luminous red galaxy (MegaZ-LRG) catalogue (Collister et al. 2007), derived from the Sloan Digital Sky Survey. The large number of sources present in this survey resulted in notably smaller error bars of these LFs, compared to previous studies in this redshift range (e.g., Sadler et al. 2007).

The LFs by Butler et al. (2019) come from a sample of 6287 sources within the XXL-South field observed at 2.1 GHz, matched with the corresponding multi-wavelength catalogue (Butler et al. 2018a, Butler et al. 2019, Butler et al. 2019). In Fig. 4.4 we show the LFs of RL AGN, classified by their radio excess (see Butler et al. 2018b, for classification details). The LFs span redshifts up to $z = 1.3$, and are in good agreement with our results.

The LFs by McAlpine et al. (2013) come from a survey of VIDEO-XMM3 field at 1.4 GHz. The survey aimed to investigate the evolution of faint radio sources (up to $100 \mu\text{Jy}$), up to a redshift of $z \approx 2.5$. The radio observations were performed with the VLA, while the photometric redshifts came from the cross-matching with the Visible and Infrared Survey Telescope for Astronomy Deep Extragalactic Observations (VIDEO; Jarvis et al. 2013) and Canada–France–Hawaii Telescope Legacy Survey (CFHTLS; Ilbert et al. 2006). The sample consist of both SFGs and AGN. The agreement between the AGN-related radio LFs with our results is good. However, it should be noted that, since the LFs by McAlpine et al. (2013) mostly sample lower luminosities, the overlap between the LFs is not large.

The radio LFs by Padovani et al. (2015) were derived from the sample of 680 sources detected and identified within Extended Chandra Deep Field South (E-CDFS; Bonzini et al. 2012, Miller et al. 2013) using the 1.4 GHz radio data observed with the VLA and cross-matched with the available multi-wavelength data. The survey probed the faint radio sky down to μJy sources. The agreement of RL AGN LFs from this survey with our results, within the error bars, is good. The uncertainties of the survey, however, become large at higher luminosities, due to a somewhat smaller area of observations ($\approx 0.32 \text{ deg.}^2$) analyzed by Padovani et al. (2015).

The LFs by Smolčić et al. (2009) come from a sample of around 600 AGN detected within the 1.4 GHz VLA–COSMOS survey (Schinnerer et al. 2007). The survey consists of low-luminosity ($L_{1.4 \text{ GHz}} \leq 5 \times 10^{25} \text{ W Hz}^{-1}$) radio AGN at intermediate redshifts up to $z \approx 1.3$. The agreement with our data is good.

The LFs by Smolčić et al. (2017b) come from the VLA-COSMOS 3 GHz Large Project.

This is the same survey discussed in Sects. 4.1 and 4.2. These observations were used together with the VLA-COSMOS 1.4 GHz Large and Deep Projects (Schinnerer et al. 2004, Schinnerer et al. 2007, Schinnerer et al. 2010). The sample consists of over 1800 radio AGN, up to redshifts of $z \approx 5$. The large depth of the survey ensured the small uncertainties even at high redshifts. The agreement with our data is good, although, given the difference in observed areas and depth of the surveys, the overlap in luminosities between the LFs becomes smaller at higher redshifts.

Apart from the non-parametric LF data points, we also show the model by Willott et al. (2001) denoted by a gray dashed line. This model was obtained by the authors using the shallow but large 7C, 6CE, 3CRR and 6CE surveys. These are the same surveys described in Sect. 2.1. Following Smolčić et al. (2009), we compared our LFs to the model and the evolution parameters from Willott et al. (2001), recalculated to our cosmology and the frequency of 1.4 GHz. The radio LFs by Willott et al. (2001) were modeled using a two-population model that assumes different shapes and evolution properties for the high- and low-luminosity ends of the sample. We concentrate here on "Model C" described by Willott et al. (2001). The low-luminosity end was modeled by a Schechter function, while the high-luminosity end was modeled by a similar function (a Schechter function with inverted functional dependency for higher and lower luminosities). The evolution of the low-luminosity end was modeled as a pure density evolution up to $z \approx 0.7$ (see Table 1 from Willott et al. 2001), after which the evolution ceases. The high-luminosity evolution was modeled by an asymmetric Gaussian function in redshift. The one-tailed Gaussian rise to redshift $z \approx 2$ was allowed to have a different width than the one-tailed decline at higher redshifts. We discuss this model in more detail in Sect. 5.4.

The AGN evolution modeled by Willott et al. (2001) is consistent with the XXL-North field LFs from this study. The standard Schechter form of the local LF did not describe the data points at the high-luminosity end properly, given an excess in volume densities at high redshift and high luminosities. It can be seen, however, that the LF model, determined by Willott et al. (2001), follows our data points well, which could suggest that the high-luminosity population of AGN evolves more rapidly than the low-luminosity end. The discrepancies at lower luminosities and high redshifts are known issues with the model (as discussed in Willott et al. 2001).

4.8 Physical interpretation of the XXL-North LFs

We have derived the the rest-frame 1.4 GHz radio LFs for radio AGN in the XXL-North field, out to $z \approx 2.1$ using the 610 MHz GMRT survey comprising of intermediate luminosity AGN ($23 \lesssim \log(L_{1.4 \text{ GHz}}[\text{W/Hz}]) \lesssim 28$). Such luminosities are missed by deep radio surveys such as COSMOS/VIDEO which usually cover much smaller areas. Since the XXL-North field is

a field of intermediate depth, these LFs simultaneously reach relatively high luminosities and redshifts. In Fig. 4.4 we compared our values, and the literature 1.4 GHz LFs for radio AGN, with the model presented by Willott et al. (2001).

Even though the modeling of the LFs via analytical functions was not performed here, the fact that the LFs do not follow a simple Schechter function, but instead seem to trace the model of evolution assuming a bimodal AGN population already has physical implications. Furthermore, this result is consistent with the physical picture presented in the introduction (Ch. 1) where the need for two physically different AGN populations was introduced. These were the radiatively efficient population and the radiatively inefficient population, the main difference between the two populations being their mode of accretion (Hardcastle et al. 2007, Heckman & Best 2014, Narayan et al. 1998, Shakura & Sunyaev 1973). More details on the shape and evolution of the LFs are at this point unclear since only non-parametric methods were used. The following chapters of this thesis further investigate the radio AGN evolutionary trends by constructing the LFs via parametric methods, resulting in fits of analytical functions, using a composite survey of varying area and depth. A comparison between the fits gives further insight into radio AGN evolution.

Chapter 5

Bayesian LF modeling

In this section we describe the parametric modeling of LFs within the Bayesian framework. The theoretical background is explained in Sect. 5.1 and 5.2. In Sect. 5.3 we describe how this parametric method is used in order to compare between different LF models, that are listed in Sect. 5.4. Sect. 5.5 describes the method of maximum volumes when used on different overlapping fields. In this chapter we perform the parametric modeling only on simulated data sets in order to test the validity of our methodology. This is presented in Sect. 5.6. In the next chapter we use these same methods on real observed data. The work presented in this and the next chapter is, at the moment of writing, submitted for publication in *Astronomy & Astrophysics*.

5.1 Bayesian modeling of LFs

Broadly speaking, the aim of Bayesian modeling is to determine the posterior $P(\Theta|D, M)$, or the probability density function of the model parameters Θ , given D, M which represent the data and model respectively. The posterior is calculated using the prior π and the likelihood L as:

$$P(\Theta|D, M) = \frac{\pi(\Theta)\mathcal{L}(D|\Theta)}{E} \quad (5.1)$$

where E is the normalisation factor, also called the evidence:

$$E = \int \pi(\Theta)\mathcal{L}(D|\Theta)d\Theta \quad (5.2)$$

The prior function $\pi(\Theta)$ quantifies our knowledge of the parameters, before any measurements are taken (Thrane & Talbot 2019). In this work the priors were chosen to be uniform, reflecting

no prior assumptions about the model parameters. Priors for parameters expressed as logarithms were taken to be uniform in the logarithmic scale. The likelihood function \mathcal{L} , describes the measurements and we discuss it in detail in the next section. The numerical calculations within this work were performed via the "Dynesty" program package by Speagle (2020). Dynesty uses dynamic nested sampling (Skilling 2004, Higson et al. 2019) during the posterior estimation.

5.2 Likelihood function

An important step in the process of Bayesian parameter estimation is calculating the likelihood function. We followed here Marshall et al. (1983) (see also Christlein et al. 2009 for a more detailed derivation). First, the complete redshift-luminosity space, in which the sample of sources is situated, is divided into infinitesimal cells $dzdL$, as represented in Fig. 5.1. We assume that the number of sources in each cell follows the Poisson probability. Assuming, furthermore, that each cell is small enough to contain up to only one source, the probability of observing N sources of the complete sample is given as a product:

$$p = \prod_i^N \lambda_i e^{-\lambda_i} \cdot \prod_j e^{-\lambda_j} \quad (5.3)$$

The first product goes over the complete sample of N sources, while the second one takes into account that all the remaining cells must remain empty. Here, λ is the expected number of sources per bin. This number can be expressed via the expected volume density of sources in a given luminosity bin dL which is given by the LF $\Phi(z, L)$ as:

$$\lambda = \Phi dV dL = \Phi \frac{dV}{dz} dz dL \quad (5.4)$$

By taking the logarithm of the probability and rearranging the sums we obtain:

$$\ln(p) = \sum_i \ln \left(\Phi_i \frac{dV_i}{dz} dz dL \right) - \int \Phi \frac{dV}{dz} dz dL \quad (5.5)$$

where Φ_i and V_i are associated with a particular source of the catalogue. The first sum goes over the observed sample, while the second sum, which was turned into an integral, covers the whole available (z, L) space. The limits of the integral therefore follow the detection limit of the survey, or in other words, it numbers all the cells where in principle a source could be observed. It therefore also follows that the integral equals the total predicted number of sources above the detection limit of the survey (Christlein et al. 2009). The log-Likelihood, $\ln \mathcal{L}$, is defined as

(e.g. Marshall et al. 1983):

$$\ln \mathcal{L} = -2 \ln(p) = -2 \sum_i \ln \left(\Phi_i \frac{dV_i}{dz} dz dL \right) + 2 \int \Phi \frac{dV}{dz} dz dL \quad (5.6)$$

The expression can be further simplified by separating the terms that depend on the LF parameters. The first term of the last equation can be divided into:

$$\sum_i \ln \left(\Phi_i \frac{dV_i}{dz} dz dL \right) = \sum_i \ln \Phi_i + \sum_i \ln \left(\frac{dV_i}{dz} dz dL \right) \quad (5.7)$$

The second term of this relation does not in any way depend on the LF parameters and, as such, adds to the log-Likelihood a constant value not important in the minimisation process. It can therefore be omitted. We have finally:

$$\ln \mathcal{L} = -2 \sum_i \ln \Phi_i + 2 \int \Phi \frac{dV}{dz} dz dL \quad (5.8)$$

This expression is the one found commonly in the literature (e.g. Kelly et al. 2008, Yuan et al. 2020). The above derivation was performed for one field. Since, in this work, we use a composite set of surveys, the relation for log-Likelihood must be generalised to multiple fields j , with different detection limits, and observational areas as:

$$\ln \mathcal{L} = -2 \sum_{i,j} \ln \Phi_i + 2 \sum_j \int_j \Phi \frac{dV}{dz} dz dL \quad (5.9)$$

where the first sum covers all the sources from all the composite fields and each integral in the second sum reaches the depth of the corresponding field as denoted by the lower integration limit. Furthermore, if the completeness of the survey near the detection limit adds non-negligible incompleteness it can be included as a separate completeness function.

5.3 Model comparison within the Bayesian framework

Although it is not possible to provide an absolute goodness of fit within the Bayesian framework, it is possible to compare the fit between a set of different models. This is performed by using the odds ratio defined as (Liddle 2007, Thrane & Talbot 2019):

$$O_{21} = \frac{p(M_2|D,I)}{p(M_1|D,I)} = \frac{E(M_2)p(M_2|I)}{E(M_1)p(M_1|I)} \quad (5.10)$$

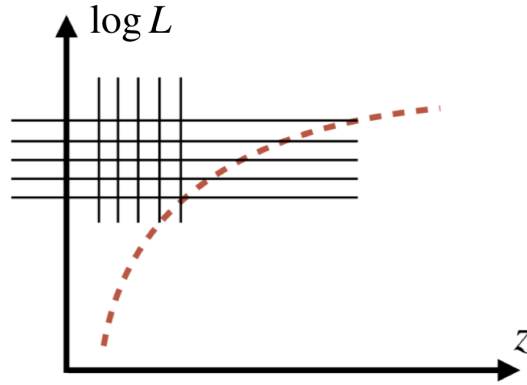


Figure 5.1: Schematic representation of the division of the $L-z$ space into sub-spaces as described in the text. The black lines denote the cells $dzdL$, while the red dashed line represents the detection limit of the survey.

Here, $E = p(D|M, I)$ is the evidence, introduced in Sect. 5.1. Factors $p(M|I)$ denote the priors. If there is no model preferred by the priors, these factor cancel out, and the odds ratio reduces to a ratio of evidences, also called the Bayes factor:

$$B_{21} = \frac{E(M_2)}{E(M_1)} \quad (5.11)$$

Throughout the literature the Bayes factor is commonly expressed as a difference in log-scale. When comparing between two models, this method selects the model with a fewer number of parameters. In other words, it naturally incorporates Occam's razor (Liddle 2007).

Apart from a direct comparison of evidences discussed above, there also exist more approximate methods of model comparison. One such method is the Akaike information criterion (AIC; Akaike 1974, Liddle 2007, Fotopoulou et al. 2016). The comparison between models is performed via AIC value defined as:

$$AIC = 2k - 2 \ln \mathcal{L} \quad (5.12)$$

where the model with the lower value of AIC is the one that corresponds to a better fit. The factor k denotes the number of parameters. It can be seen therefore, that this method also penalises a larger number of parameters, or in other words, includes also the Occam's razor.

Lastly, similar to AIC, we also have the Bayesian information criterion (BIC; Schwarz 1978,

Table 5.1: LF models used in this work, corresponding list of free parameters, and their number N_{Par} .

| Model | Parameters | N_{Par} |
|------------|---|-----------|
| Sadler+02 | $\Phi^*, L^*, \sigma, \alpha, \alpha_D, \alpha_L$ | 6 |
| PDE | $\Phi^*, L^*, \sigma, \alpha, \alpha_D$ | 5 |
| PLE | $\Phi^*, L^*, \sigma, \alpha, \alpha_L$ | 5 |
| Novak+18 | $\Phi^*, L^*, \sigma, \alpha, \alpha_D, \alpha_L, \beta_D, \beta_L$ | 8 |
| LDDE | $\Phi^*, L^*, \sigma, \alpha, z_c^*, a, L_a, p_1, p_2$ | 9 |
| Willott+01 | $\Phi_{l0}, L_l^*, \alpha_l, k_l, z_{l0}, \Phi_{h0}, L_h^*, \alpha_h, z_{h0}, z_{h1}, z_{h2}$ | 11 |

(Liddle 2007, Fotopoulou et al. 2016), defined as

$$BIC = k \ln N - 2 \ln L \quad (5.13)$$

where N is the number of data points and k denotes again the number of parameters. The value of BIC is the numerical approximation for the Bayes factor. From the above expression it is also clear that, given a sufficiently large number of data points N , the penalty for models with a large number of parameters is stronger than for AIC.

5.4 LF models

In this section we list all the LF models investigated in this work. We discuss separately the shape of the local LF, or the LF at redshift $z = 0$, and the evolution of this function with redshift. The complete summary of the models is presented in Tab. 5.1.

5.4.1 Local LF

The most common way to describe the local LF is by using a power-law with an exponential cut-off (Saunders et al. 1990, Sadler et al. 2002, Smolčić et al. 2009):

$$\Phi_0(L) = \Phi^* \left(\frac{L}{L^*} \right)^{1-\alpha} \exp \left\{ \frac{-1}{2\sigma^2} \left[\log \left(1 + \frac{L}{L^*} \right) \right]^2 \right\} \quad (5.14)$$

where L^* is the break luminosity, Φ^* the LF normalisation and σ the high-luminosity slope. Another common choice is the double power law used often for radio and X-ray AGN samples (Dunlop & Peacock 1990, Mauch & Sadler 2007, Smolčić et al. 2017b, Fotopoulou et al. 2016). There are also less common models of which we mention the bimodal model by Willott et al. (2001). The form of the LF in this model is different for the high and low luminosity end of the

sample. We discuss this model in more detail separately in Sect. 5.4.3 below.

5.4.2 LF evolution

The two main ways that the LF changes through cosmic time, as described in Ch. 1, is in the number density of sources and in their luminosity. If the LF changes purely via number density, we talk about the pure density evolution (PDE). The redshift dependence is given as:

$$\Phi(L, z) = (1+z)^{\alpha_D} \times \Phi_0[L] \quad (5.15)$$

where α_D is the parameter of evolution, chosen here to be a constant. If, on the other hand, only the luminosity changes, we have the pure luminosity evolution (PLE) given via:

$$\Phi(L, z) = \Phi_0 \left[\frac{L}{(1+z)^{\alpha_L}} \right] \quad (5.16)$$

Here α_L is the parameter of luminosity evolution. A very common model of evolution supposes that there is a mixture of these two modes of evolution:

$$\Phi(L, z) = (1+z)^{\alpha_D} \times \Phi_0 \left[\frac{L}{(1+z)^{\alpha_L}} \right] \quad (5.17)$$

In this work we refer to this model as Sadler+02. Another parametrization of LF evolution, found in Novak et al. (2017), allows for a redshift dependence of evolution parameters as:

$$\Phi(L, z) = (1+z)^{(\alpha_D+z\beta_D)} \times \Phi_0 \left[\frac{L}{(1+z)^{(\alpha_L+z\beta_L)}} \right] \quad (5.18)$$

where β parameters quantify the change of evolution with redshift. In this work, we refer to this model as Novak+18.

A more complex model, that can account for the difference in evolution between the high and low luminosity end of the sample, is the luminosity dependent density evolution (LDDE; Schmidt & Green 1983, Ueda et al. 2003). Following Fotopoulou et al. (2016) we defined it as:

$$\Phi(L, z) = \Phi_0 \times \frac{(1+z_c)^{p_1} + (1+z_c)^{p_2}}{\left(\frac{1+z_c}{1+z}\right)^{p_1} + \left(\frac{1+z_c}{1+z}\right)^{p_2}} \quad (5.19)$$

where:

$$z_c = \begin{cases} z_c^* & , \quad L > L_a \\ z_c^* \cdot \left(\frac{L}{L_a}\right)^a & , \quad L \leq L_a \end{cases} \quad (5.20)$$

Here, L_a is the luminosity where the evolution changes, and z_c redshift after which the evolution changes. Factors $p_{1,2}$ are the parameters of evolution. It is immediately clear from the above expression that there is a degeneracy between the $p_{1,2}$ parameters. This effect can be eliminated by limiting the prior space so that each parameter can obtain only a single value.

5.4.3 Bimodal evolution model

As a special case we discuss the model by Willott et al. (2001). We refer to it in this work as Willott+01. Both the shape and the evolution of the sample have a different analytical form for the high and low luminosity end of the sample. We discuss in this work, following Smolčić et al. (2009), the model "C" from Willott et al. (2001), being the most flexible one. This model was already introduced in Sect. 4.7 but only as a comparison for the non-parametric LFs, and with parameters fixed and determined from the literature. Here, we present its analytical form. The model is defined as:

$$\Phi = \Phi_l + \Phi_h \quad (5.21)$$

where Φ_l is the low luminosity end of the function:

$$\Phi_l = \begin{cases} \Phi_{l0} \left(\frac{L}{L_l^*}\right)^{-\alpha_l} \exp\left(\frac{-L}{L_l^*}\right) (1+z)^{k_l} & , \quad z < z_{l0} \\ \Phi_{l0} \left(\frac{L}{L_l^*}\right)^{-\alpha_l} \exp\left(\frac{-L}{L_l^*}\right) (1+z_{l0})^{k_l} & , \quad z > z_{l0} \end{cases} \quad (5.22)$$

and Φ_h is the high luminosity end:

$$\Phi_h = \begin{cases} \Phi_{h0} \left(\frac{L}{L_h^*}\right)^{-\alpha_h} \exp\left(\frac{L_h^*}{-L}\right) \cdot \exp\left[\frac{-1}{2} \left(\frac{z-z_{h0}}{z_{h1}}\right)\right] & , \quad z < z_{h0} \\ \Phi_{h0} \left(\frac{L}{L_h^*}\right)^{-\alpha_h} \exp\left(\frac{L_h^*}{-L}\right) \cdot \exp\left[\frac{-1}{2} \left(\frac{z-z_{h0}}{z_{h2}}\right)\right] & , \quad z > z_{h0} \end{cases} \quad (5.23)$$

The factor L^* denotes the break luminosity, Φ_0 the normalisation and α the slope of the LFs. Parameter z_0 is the redshift at which the evolution changes. These parameters are doubled for the high and low luminosity end of the sample as denoted by the extra indices h, l . Parameters k_l, z_{h1} and z_{h2} quantify the evolution.

5.5 Maximum volumes on composite fields

As a complementary method to the Bayesian modeling, we use also the non-parametric method of maximum volumes, described already in Sect. 4.3. As before, the LF data points are estimated by summing the inverse maximum volumes of possible observation $1/V_{Max,i}$. The error-bars are again Gaussian, except when the number of sources for a single data point equaled less than 10, in which case we used the values calculated by Gehrels (1986).

The main difference, as opposed to the single field survey used in Sect. 4.3, is that we now have a composite set of surveys with varying area and depth, which can overlap. We follow therefore the procedure described in Avni & Bahcall (1980) (see also Giallongo et al. 2005, Johnston 2011b, Gruppioni et al. 2013 Fotopoulou et al. 2016). The maximum volumes were calculated by taking into account all the fields where in principle this source could have been detected. In other words, for a given range of redshifts $[z_1, z_2]$ we have:

$$V_{Max, i} = \sum_j \omega_j \int_{z_1}^{z_{Up}^{(i,j)}} \frac{dV}{dz} dz \quad (5.24)$$

Here ω_j is the area of each respective field and the sum goes over all the fields j where source i could have been observed. The upper limit of the integral denotes the minimum between the upper end of the redshift bin z_2 , and the maximum redshift of possible detection given the detection limit of the corresponding survey. All in all, we thus take into account the fact that the sources from the shallow fields are detectable in all the deeper fields as well. This in turn modifies the value of their maximum volume (Gruppioni et al. 2013).

In practice, the numerical calculations were performed by dividing the redshift interval into smaller subsets, as already described in Sect. 4.3. We plotted the resulting LF data points on the same plots with the parametrically determined LFs. As these data points trace the LFs directly, without assuming any functional form, they act as a valuable comparison.

5.6 Results on simulated data sets

Before using the described methodology on real observed data, we tested it on simulated data sets. The simulated data sets were obtained by randomly generating sources using an assumed LF, which acted as a probability distribution. The resulting catalogue of mock sources was then used to model the LFs. The consistency between the assumed and the retrieved LF gave insight into the validity and robustness of the fitting process. During the creation of the simulated catalogue we selected the area and detection limit of the mock-observations, as well as the

Table 5.2: Assumed and retrieved parameters resulting from the modeling of LFs on simulated data. As described in the text, a mock catalogue was created using assumed LF models. This catalogue was then used to model the LFs in order to test the validity of the modeling methodology.

| Parameter | Assumed | Retrieved | +2 σ | -2 σ |
|---------------|---------|-----------|-------------|-------------|
| $\log \Phi^*$ | -5.10 | -4.99 | 0.77 | 0.50 |
| $\log L^*$ | 23.0 | 22.82 | 0.83 | 2.40 |
| α | 1.50 | 1.50 | 0.08 | 0.40 |
| σ | 1.50 | 1.53 | 0.22 | 0.16 |
| α_D | 1.00 | 0.92 | 0.64 | 0.56 |
| α_L | 0.50 | 0.68 | 0.80 | 0.86 |

frequencies of observations and LF modelling. We selected the value of the source spectral indices, and allowed for a non-negligible uncertainties in source redshifts. We also included the possibility of catalogue incompleteness as functions of either redshift or flux. The flux-dependent incompleteness mimics the incompleteness arising during real observations due to the non-uniformity of noise in the observed field. The incompleteness as a function of redshift arises during the matching process due to different detection limits of surveys. These corrections were motivated by those used on real observed data, as seen from Sect. 4.4.

As an example, we describe here the process performed on a Schechter LF model, with a superposition of PDE and PLE evolution (named Sadler+02 within this work). The area of the field was set to 40.46 deg^2 , and the detection limit to $50 \mu\text{Jy}$. This resulted in a simulated catalogue of 6378 mock sources above the detection limit, created by randomly selecting sources via the assumed LF. The starting parameters of the LF are given in Tab. 5.2. The scatter in redshifts was set here to be negligible, but a finite uncertainty in redshifts, via hierarchical bayesian interference, was later also tested. The parameter modeling was performed on this simulated data set, using the same codes later used on observational data. The retrieved parameters are shown also in Tab. 5.2. The detection limit in this example was a step-function i.e. the completeness corrections were not present. We also assumed a mean spectral index of -0.7 .

In Fig. 5.2 we show the process visually. The starting LF is denoted by a green dashed line. This LF was used to create the simulated catalogue of sources, from which the LFs were re-estimated. The re-estimated LFs are given in grey. The lines denote the median value and the 90% quantiles. The quantiles were estimated by creating 5000 LFs by selecting parameter samples from the posterior. As a final check, we also re-created the LFs via the non-parametric method of maximum volumes. These data points are given in the figure in red. It can be seen that the re-estimation of the LFs was successful via both the parametric and non-parametric methods. In Fig. 5.3 we show the corner plot of the posterior probabilities of the model parameters. The

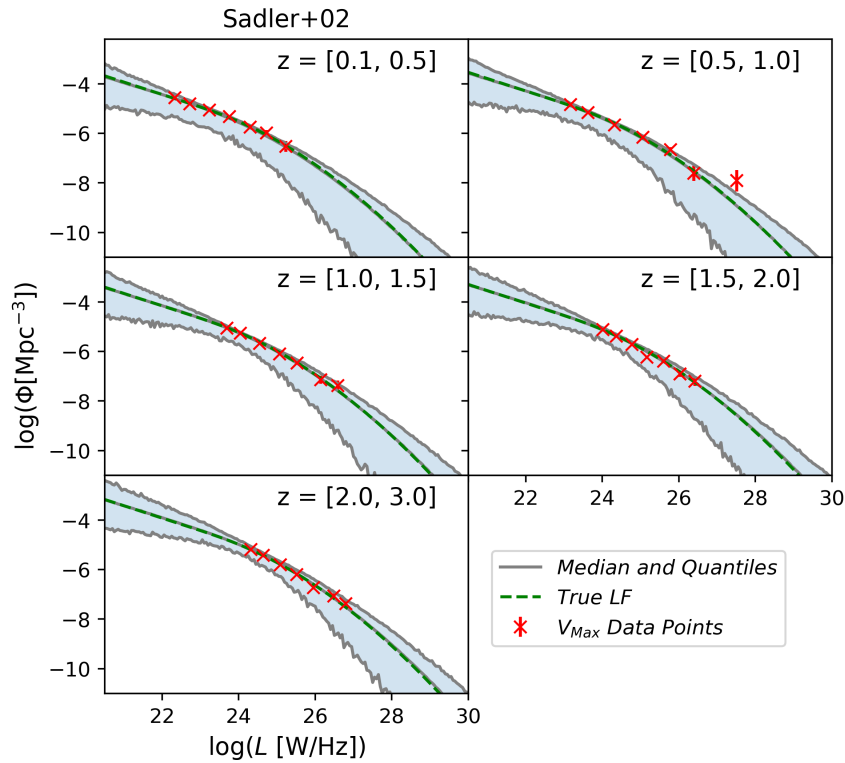


Figure 5.2: LFs created from a simulated catalogue. The green dashed line denotes the starting LF, while the grey lines denote the re-estimated LFs median and 90% quantiles. The Red crosses denote the non-parametric method of maximum volumes.

assumed values used to create the starting LF are denoted by vertical black lines. The corner plot also confirms that the LF re-estimation was successful.

Apart from the described example, the methodology was tested for all the models described in Sect. 5.4 and on different areas and depths of mock-catalogues. The codes were also tested for non-negligible completeness corrections, by introducing completeness correction as a separate function during the integration of log-Likelihood. We also tested them on data sets with a finite scatter in redshift values. The parameters of the LFs were always retrieved successfully, both for single mock fields, and sets of multiple mock fields taken together as a composite field.

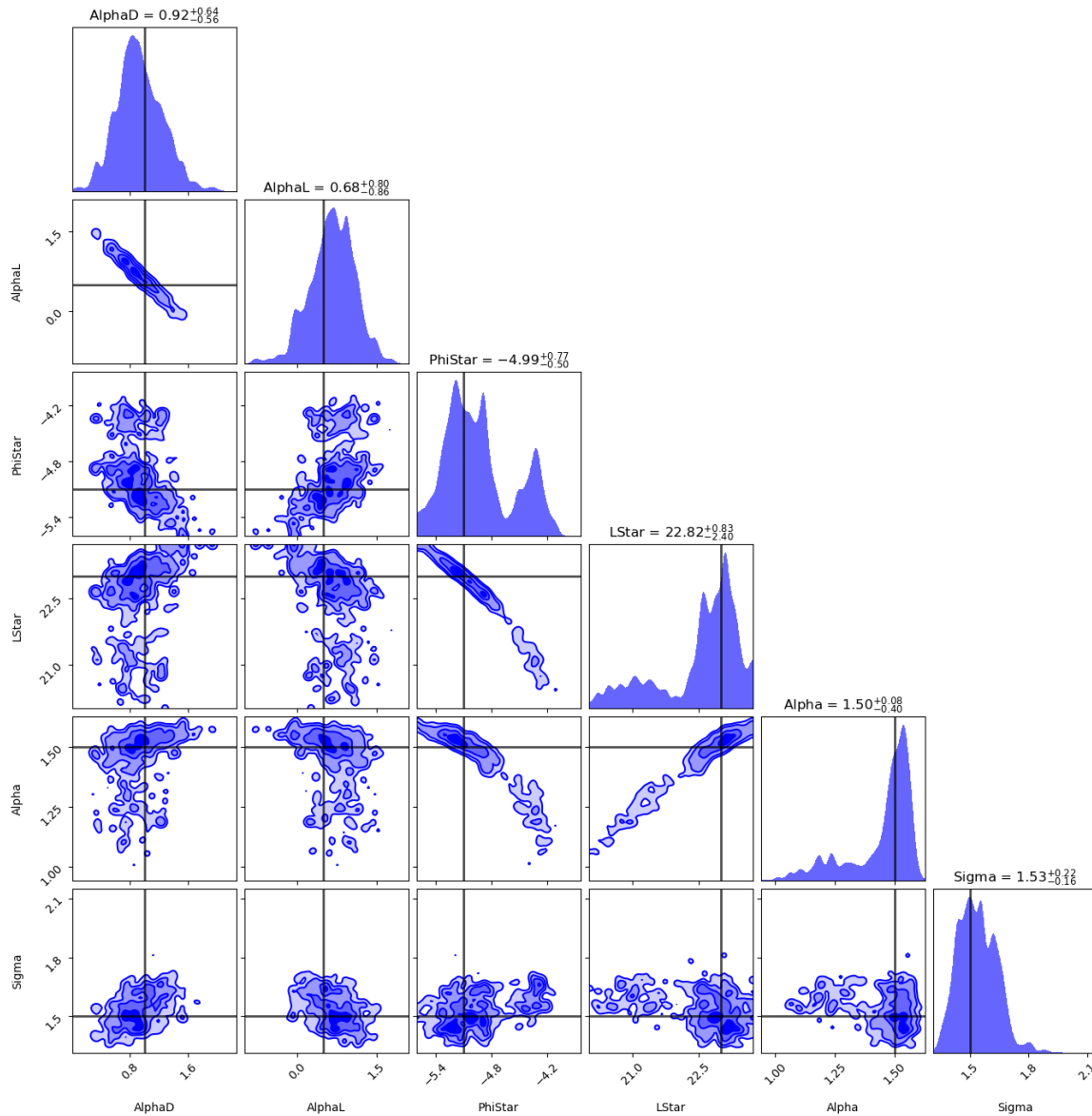


Figure 5.3: Corner plot showing the posterior distributions of the model parameters in blue. The black lines denote the assumed values used to create the starting LF from which the simulated data set was created. The numbers above the probabilities, denoting the retrieved parameter values are also given in Tab. 5.2.

Chapter 6

Luminosity functions of the composite survey

After testing the methodology on simulated data sets, we used it in order to model the LFs using real observed data sets, namely the COSMOS, XXL, 3CRR, 7C and 6CE fields, described in Sect. 2, combining all the catalogues as a single composite survey. We assumed different functional forms for the shape and the evolution of the LFs, in order to parameterise the evolution of AGN. The numerical calculations were performed again by the Dynesty program package. The LF modeling resulted in posterior probabilities of model parameters. We also estimated the marginal likelihoods for each model, important for model comparison. The model selection is described in Sect. 6.1. The models that were not optimal in describing our data are listed in Sect 6.2 together with the corresponding plots and tables of posterior parameter estimates. The best-fitting model is described in Sect. 6.3.

6.1 Model comparison

The model comparison within the Bayesian framework is performed by estimating the posterior probabilities of model parameters and calculating the marginal likelihood. Comparison of marginal likelihoods between different models determines the relative standing of each fit. The models we compared between are described in Sect. 5.4, and summarised as follows:

- PDE model (relation 5.15)
- Novak+18 model (relation 5.18)
- PLE model (relation 5.16)
- Willott+01 model (relations 5.21 - 5.23)
- Sadler+02 model (relation 5.17)
- LDDE model (relation 5.19)

Table 6.1: Comparison of the best-fitting LDDE model with other models using three different methods, comparing their marginal likelihoods, and the approximate AIC and BIC methods, as described in the text. The difference in log-marginal-likelihoods is multiplied by two for easier comparison.

| Model | $2 \cdot \log B_{21}$ | $-\Delta\text{AIC}$ | $-\Delta\text{BIC}$ |
|------------|-----------------------|---------------------|---------------------|
| Sadler+02 | 278.82 | 283.98 | 264.64 |
| PDE | 316.84 | 326.69 | 300.91 |
| PLE | 312.86 | 320.20 | 294.41 |
| Novak+18 | 67.26 | 70.75 | 64.30 |
| Willott+01 | 57.76 | 43.22 | 56.11 |

The spectral indices for each source was taken from the corresponding catalogue. We also assumed that the redshift estimates were determined correctly, so no further methods were incorporated to assess the uncertainties. These assumptions are further discussed in Sect. 6.4. The completeness corrections of each survey can be introduced naturally by using a smooth detection limit which is a function of flux, or redshift, instead of an abrupt cutoff. For the XXL-North field, we used the corrections described in 4.4. For the COSMOS field, the correction can be found in Smolčić et al. (2017a), in their Figure 16 or Table 02. The other surveys were considered complete (Willott et al. 2001, Butler et al. 2018a).

The relative goodness of each model was determined both by comparing their marginal likelihoods, and via the approximate AIC and BIC methods, as described in 5.3. According to our data set, the best fitting model was the LDDE model, given by relations 5.19 and 5.20. The resulting values of marginal likelihood, as well as AIC and BIC values, used for the model comparison, are listed in Tab. 6.1, where we show a comparison between the best-fitting LDDE model and the other models. We list the values of three different methods in separate columns for comparison. It can be seen that the three methods give consistent results, where the LDDE model is consistently the preferred one. According to the Jeffrey’s interpretation of evidence ratios (e.g. Kass & Raftery 1995), the interpretation varies from "strong" (> 10) to "decisive" (> 100) in favour of the LDDE model.

6.2 Non-optimal LF models

We now describe the non-optimal models tried in the LF modeling process. The resulting LF plots and parameter estimates are presented. We then discuss the LDDE model separately in the next section.

6.2.1 Pure density evolution

The simplest models investigated were the PDE and PLE models (relations 5.15 and 5.16 respectively). In Fig. 6.1 we first show the resulting LF for the PDE model. The shape of the local LF was chosen as a Schechter function, given in relation 5.14. The evolution of LFs is parameterised via their change in density, as described in relation 5.15. The grey lines in Fig. 6.1 represent the median and 90% quantiles obtained from the posterior by sampling randomly 5000 parameter samples. This method of representing the errors conserves the correlation between the parameters. The blue line represents the fiducial line drawn in the lowest redshift bin, in order to visualise the LF evolution. The red data points denote the LFs estimated by the non-parametric method of maximum volumes. The resulting posterior probabilities of the LF parameters were estimated, and the mean values and deviations are listed in Tab. 6.2.

Table 6.2: Parameters of the PDE model. The standard deviation, provided by the Dynesty package, is asymmetric. These numbers represent the mean values and deviations determined from the posterior distribution.

| Parameter | Mean | +2 σ | -2 σ |
|---------------|-------|-------------|-------------|
| α_D | 0.15 | 0.07 | 0.08 |
| $\log \Phi^*$ | -3.49 | 0.52 | 0.32 |
| $\log L^*$ | 21.76 | 0.64 | 1.34 |
| α | 1.44 | 0.09 | 0.15 |
| σ | 1.88 | 0.08 | 0.07 |

6.2.2 Pure luminosity evolution

The PLE model assumes the evolution of the LFs happens via change in the luminosity of AGNs. The local LF was again chosen to be the Schechter function, given in relation 5.14. The evolution of LFs is described in relation 5.16. Fig. 6.2 shows the resulting LF. The method of drawing the function follows the one described in Sect. 6.2.1. The mean values and deviation of model parameters are listed in Tab. 6.3.

6.2.3 PDE and PLE mixture

The model where the evolution of LFs is a superposition of evolution in density and luminosity was denoted within this work as Sadler+02. The local LF was again the Schechter function, given in relation 5.14, while the evolution of LFs is described via relation 5.17. Fig. 6.3 shows

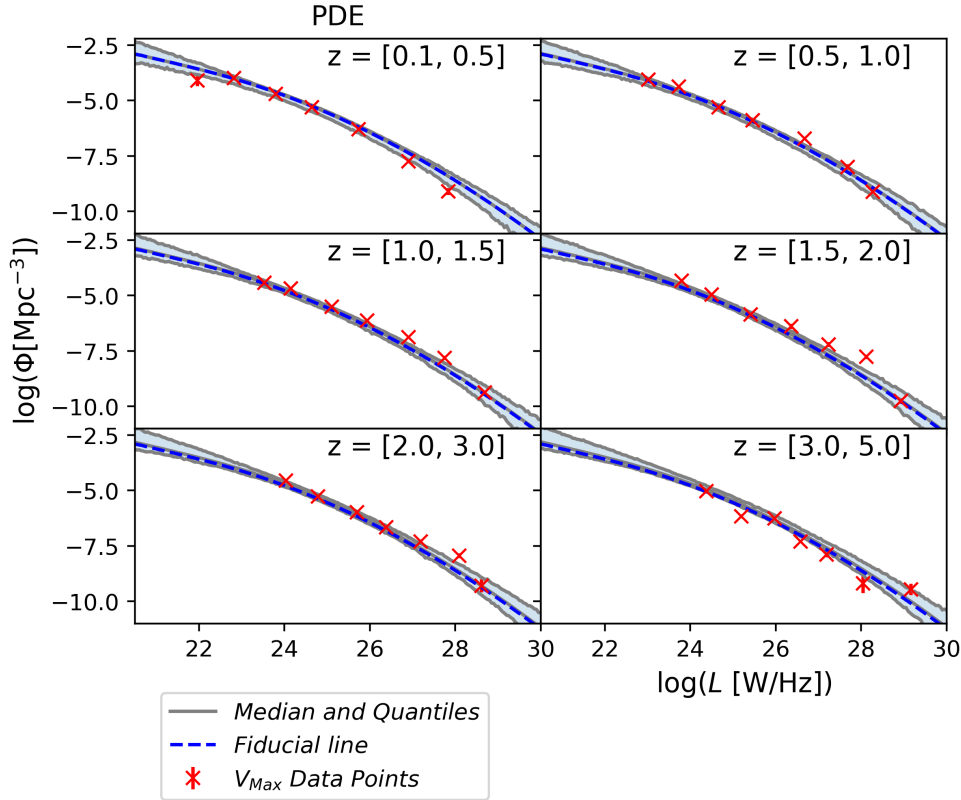


Figure 6.1: The PDE model of evolution (relation 5.15), using a Schechter local LF (5.14), modeled using the COSMOS, XXL, 3CRR, 7C and 6CE surveys, obtained by two complementary methods: Bayesian modeling and the method of maximum volumes. Grey lines denote the median and 90% quantiles of the parametric Bayesian inference. The crosses denote the non-parametric method of maximum volumes, together with the corresponding error-bars. The uncertainties were derived assuming a Poisson errors. The blue dashed fiducial line denotes the LF determined in the first redshift bin.

the resulting LFs. The mean values and deviations of the resulting parameters are listed in Tab. 6.4.

6.2.4 Redshift dependent evolution

The model of LFs where the evolution depends on redshift, as described in 5.18, is denoted in this work as Novak+18. The local LF was again the Schechter function, given in relation 5.14. Fig. 6.4 shows the resulting LF, while the mean values of the parameters are given in Tab. 6.5.

Table 6.3: Parameters of the PLE model. The mean values and deviations were determined from the posterior distribution.

| Parameter | Mean | +2 σ | -2 σ |
|---------------|-------|-------------|-------------|
| α_L | 0.21 | 0.08 | 0.09 |
| $\log \Phi^*$ | -3.46 | 0.51 | 0.31 |
| $\log L^*$ | 21.70 | 0.63 | 1.38 |
| α | 1.43 | 0.08 | 0.17 |
| σ | 1.87 | 0.07 | 0.07 |

Table 6.4: Parameters of the Sadler+02 model. The mean values and deviations were determined from the posterior distribution.

| Parameter | Mean | +2 σ | -2 σ |
|---------------|-------|-------------|-------------|
| α_D | -1.68 | 0.49 | 0.28 |
| α_L | 2.24 | 0.35 | 0.58 |
| $\log \Phi^*$ | -3.10 | 0.29 | 0.24 |
| $\log L^*$ | 21.21 | 0.52 | 0.83 |
| α | 1.39 | 0.08 | 0.12 |
| σ | 1.78 | 0.06 | 0.07 |

6.2.5 Bimodal evolution

The model with the largest number of parameters was the one denoted within this work as Willott+01, and described in Sect. 5.4.3. Both the shape and evolution of LFs within this model were different for the high luminosity and low luminosity AGNs. Fig. 6.5 shows the resulting LFs. The mean values of parameters are given in Tab. 6.6.

Table 6.5: Parameters of the Novak+18 model. The mean values and deviations were determined from the posterior distribution.

| Parameter | Mean | +2 σ | -2 σ |
|---------------|-------|-------------|-------------|
| α_D | -0.79 | 0.73 | 0.68 |
| α_L | 2.71 | 0.86 | 0.92 |
| β_D | -0.24 | 0.19 | 0.18 |
| β_L | -0.12 | 0.23 | 0.25 |
| $\log \Phi^*$ | -3.22 | 0.36 | 0.31 |
| $\log L^*$ | 21.13 | 0.64 | 0.93 |
| α | 1.42 | 0.09 | 0.13 |
| σ | 1.81 | 0.06 | 0.06 |

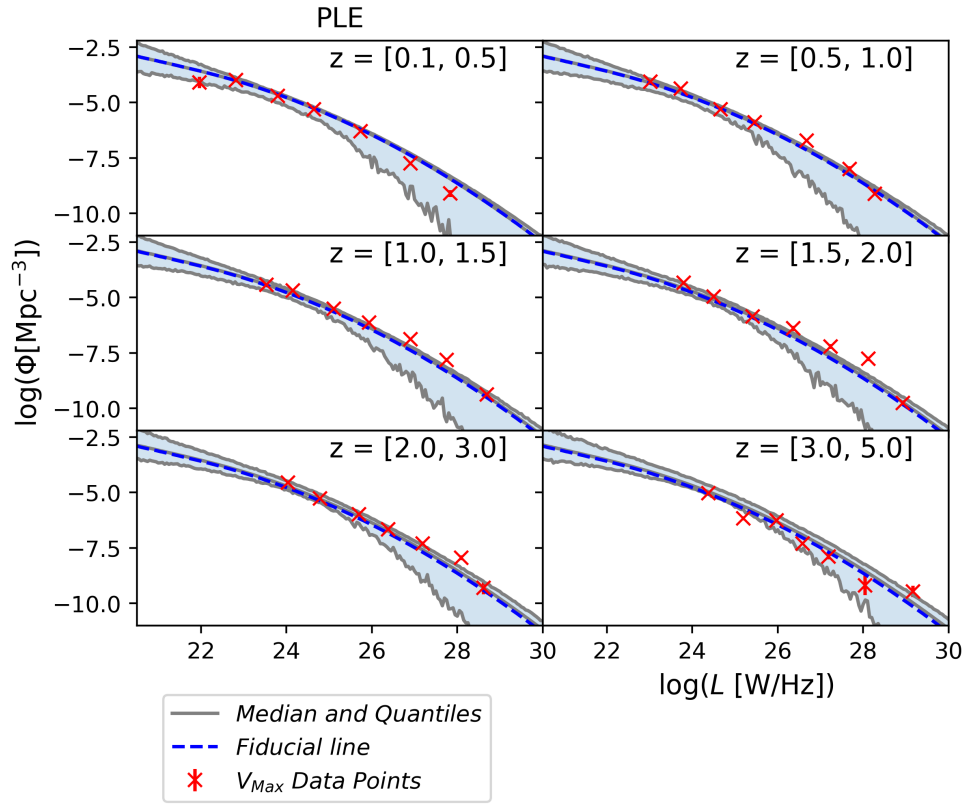


Figure 6.2: The PLE model of evolution (relation 5.16), using a Schechter local LF (5.14), modeled using the COSMOS, XXL, 3CRR, 7C and 6CE surveys. The notation follows Fig. 6.1.

Table 6.6: Parameters of the Willott+01 model. The mean values and deviations were determined from the posterior distribution.

| Parameter | Mean | +2 σ | -2 σ |
|------------------|-------|-------------|-------------|
| $\log \Phi_{l0}$ | -6.18 | 0.15 | 0.14 |
| $\log L_l^*$ | 25.83 | 0.14 | 0.12 |
| α_l | 0.68 | 0.02 | 0.03 |
| k_l | 0.76 | 0.13 | 0.32 |
| z_{0l} | 1.05 | 0.03 | 0.03 |
| $\log \Phi_{h0}$ | -6.09 | 0.07 | 0.08 |
| $\log L_h^*$ | 26.45 | 0.12 | 0.12 |
| α_h | 1.43 | 0.06 | 0.07 |
| z_{h1} | 0.44 | 0.08 | 0.06 |
| z_{h2} | 2.51 | 0.38 | 0.35 |
| z_{0h} | 1.23 | 0.13 | 0.10 |

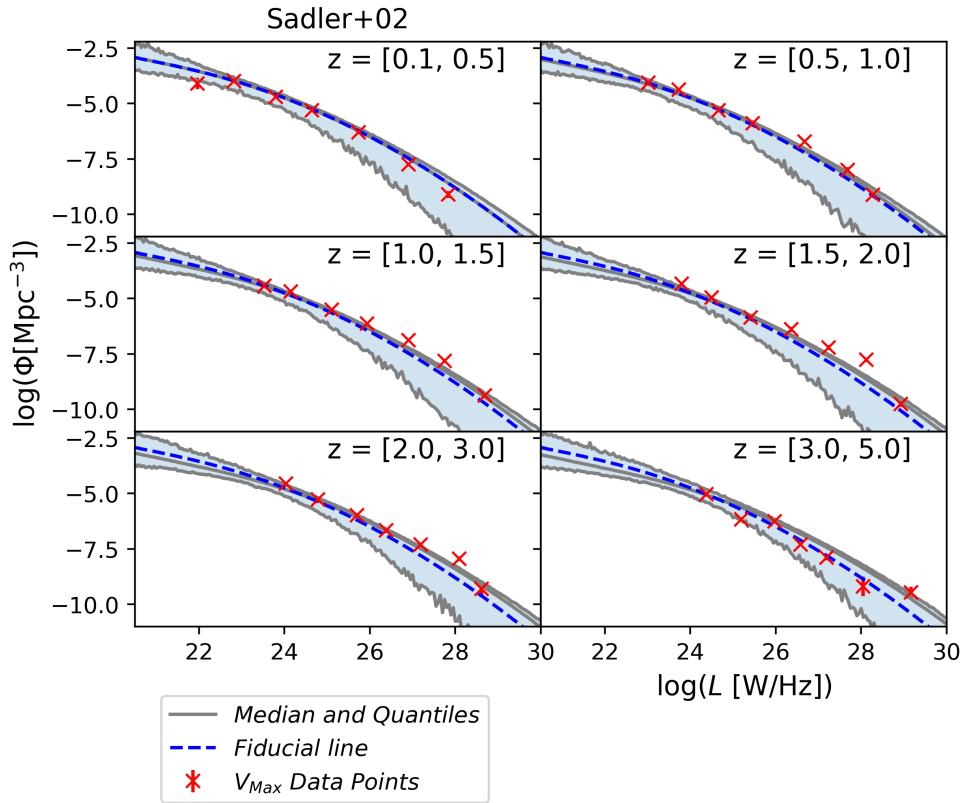


Figure 6.3: The Sad02 model of evolution (relation 5.17), using a Schechter local LF (5.14), modeled using the COSMOS, XXL, 3CRR, 7C and 6CE surveys. The notation follows Fig. 6.1.

6.3 Luminosity-dependent evolution

We now show the best-fitting luminosity-dependent evolution model, denoted within this work as LDDE, and described via relations 5.19 and 5.20. The resulting LFs are shown in Fig. 6.6. We show also the resulting corner-plot of the parameter posterior probabilities in Fig. 6.7. The corner-plot details the parameter posterior probabilities of the model. In Tab. 6.7 the mean values and deviations of the parameters are again listed. The break luminosity equaled $\log(L^*/\text{WHz}^{-1}) = 22.28^{+0.42}_{-0.55}$ and $z^* = 2.01^{+0.61}_{-0.38}$. The degeneracy in p_1 and p_2 parameters is an expected occurrence, as seen from equation 5.19, but it was eliminated by choosing the prior so that it encompasses only one peak. The modeling was also tested without this simplification, and the results were qualitatively identical.

The number of sources constraining the LFs at different redshifts and luminosities are shown in Fig. 6.6. The LF in the last redshift bin is therefore the least constrained. The LFs are considered well constrained at redshifts $z < 3$ and luminosities $\log L \in [22, 29]$. Outside these limits the results should be interpreted with caution.

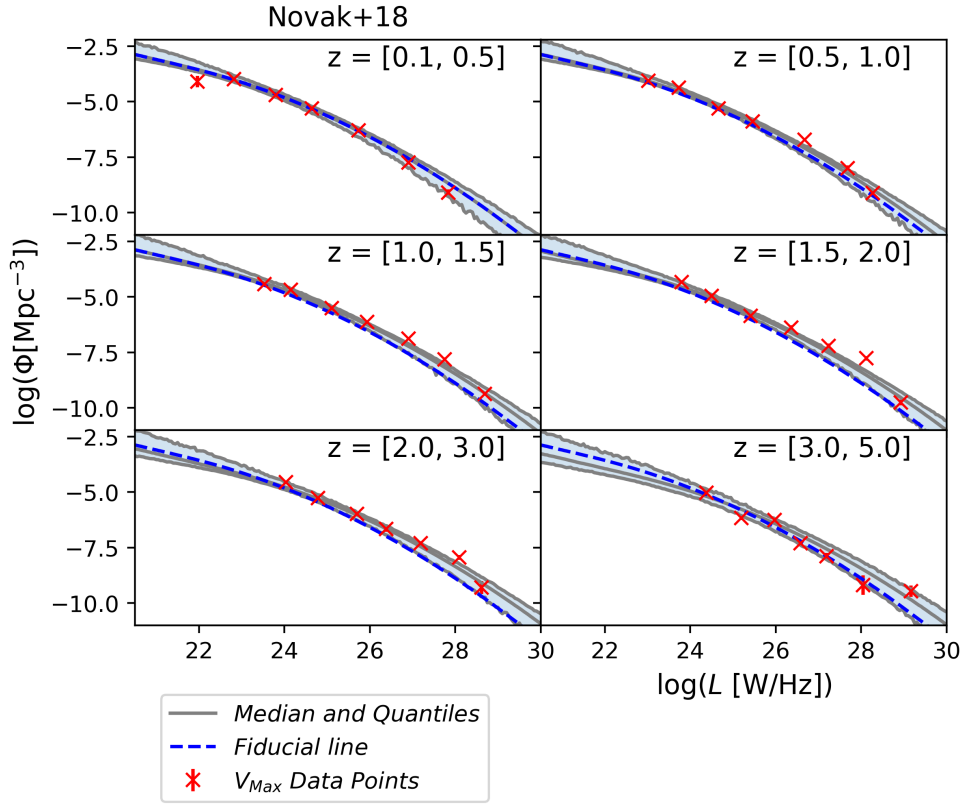


Figure 6.4: The evolution model from Novak et al. (2017) (relation 5.18), using a Schechter local LF (relation 5.14), modeled using the COSMOS, XXL, 3CRR, 7C and 6CE surveys. The notation follows Fig. 6.1.

Table 6.7: Parameters of the best fitting LDDE model. The model is provided in the text in relations (5.19 and 5.20).

| Parameter | Mean | +2 σ | -2 σ |
|---------------|-------|-------------|-------------|
| z_C^* | 2.01 | 0.61 | 0.38 |
| $\log L_a$ | 27.94 | 0.23 | 0.24 |
| a | 0.40 | 0.07 | 0.06 |
| p_1 | -0.39 | 0.11 | 0.10 |
| p_2 | 4.53 | 0.76 | 0.77 |
| $\log \Phi^*$ | -3.92 | 0.21 | 0.21 |
| $\log L^*$ | 22.28 | 0.42 | 0.55 |
| α | 1.39 | 0.09 | 0.11 |
| σ | 1.40 | 0.06 | 0.05 |

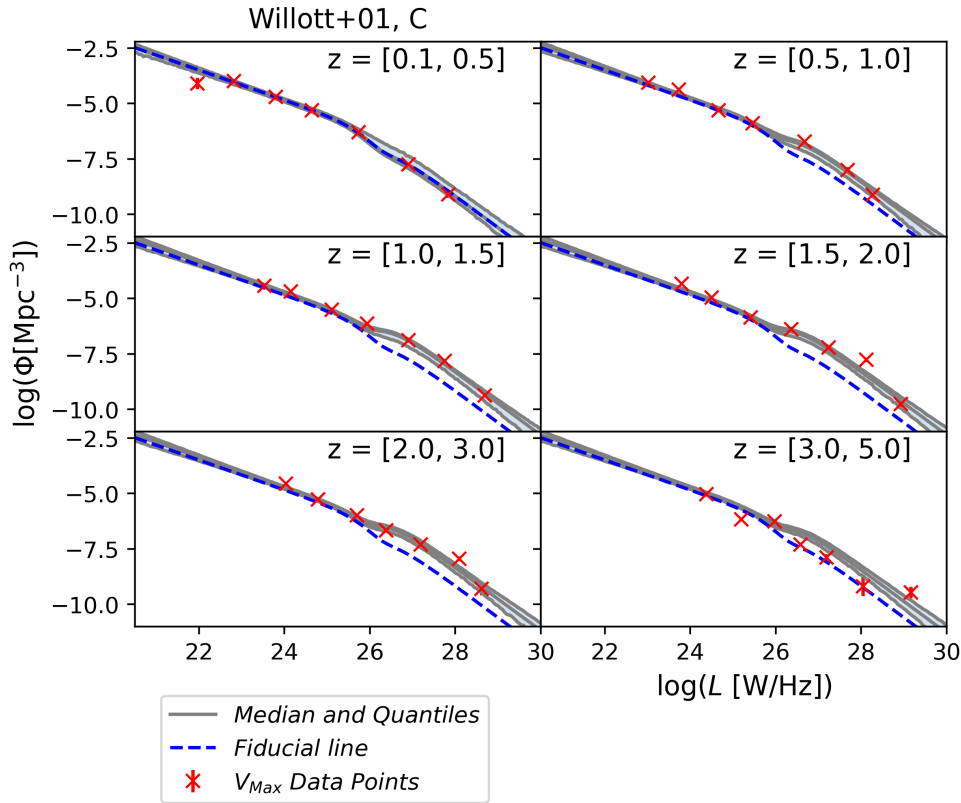


Figure 6.5: The evolution model from Willott et al. (2001), using the corresponding local LF (relations 5.21 - 5.23), modeled using the COSMOS, XXL, 3CRR, 7C and 6CE surveys. The notation follows Fig. 6.1.

6.4 Additional checks

After performing the modeling of LFs, and the model comparison, a few additional checks were performed in order to test the robustness of the results. Firstly we examined the effect of spectral indices on the results. For this, we re-modeled the LFs using different values of spectral indices. First we used the same value of spectral index for each source, setting it to -0.7 , which corresponds to the often used mean value of spectral indices found in the literature. We then repeated the modeling using for each source the mean spectral index of the corresponding survey, as listed in Tab. 2.1. The results remained consistent, with the LDDE model being the best fitting one, according to all comparison criteria.

Secondly, we investigated how uncertainties in redshift affect our results. Here we concentrated on the XXL-North field, this being the field with largest uncertainties in redshift. Redshift uncertainties could, in principle, be addressed via the hierarchical Bayes method (see Loredó 2004, Aird et al. 2010, Fotopoulou et al. 2016). This was, however, deemed too time con-

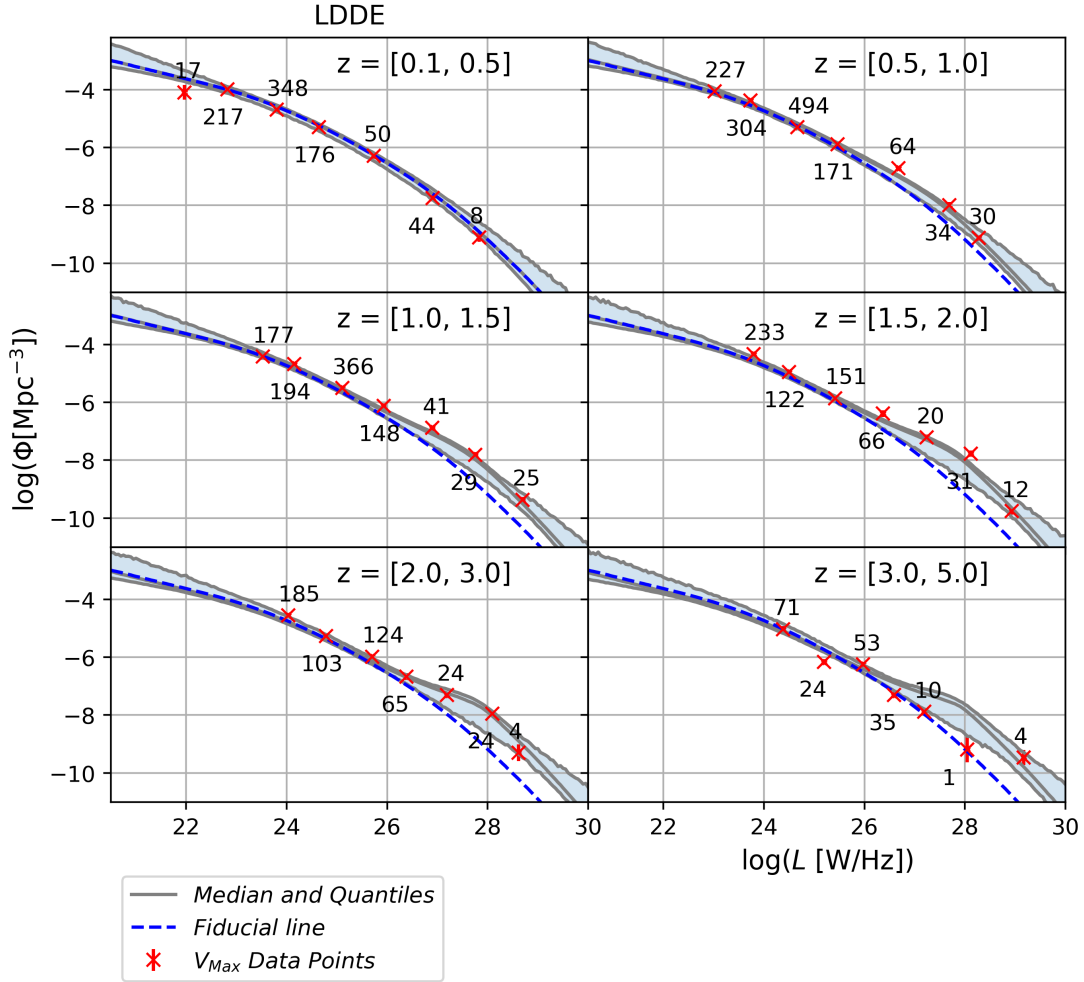


Figure 6.6: The LDDE model of evolution (relation 5.19) using a Schechter local LF (relation 5.14), modeled using the COSMOS, XXL, 3CRR, 7C and 6CE surveys, obtained by two complementary methods: Bayesian modeling and the method of maximum volumes. Grey lines denote the median and 90% quantiles of the parametric Bayesian inference. These values were obtained by randomly drawing samples from the posterior. The crosses denote the non-parametric method of maximum volumes, together with the corresponding error-bars. The uncertainties were derived assuming Poisson errors. We also show the number of sources creating each data-point. The blue dashed fiducial line denotes the LF determined in the first redshift bin.

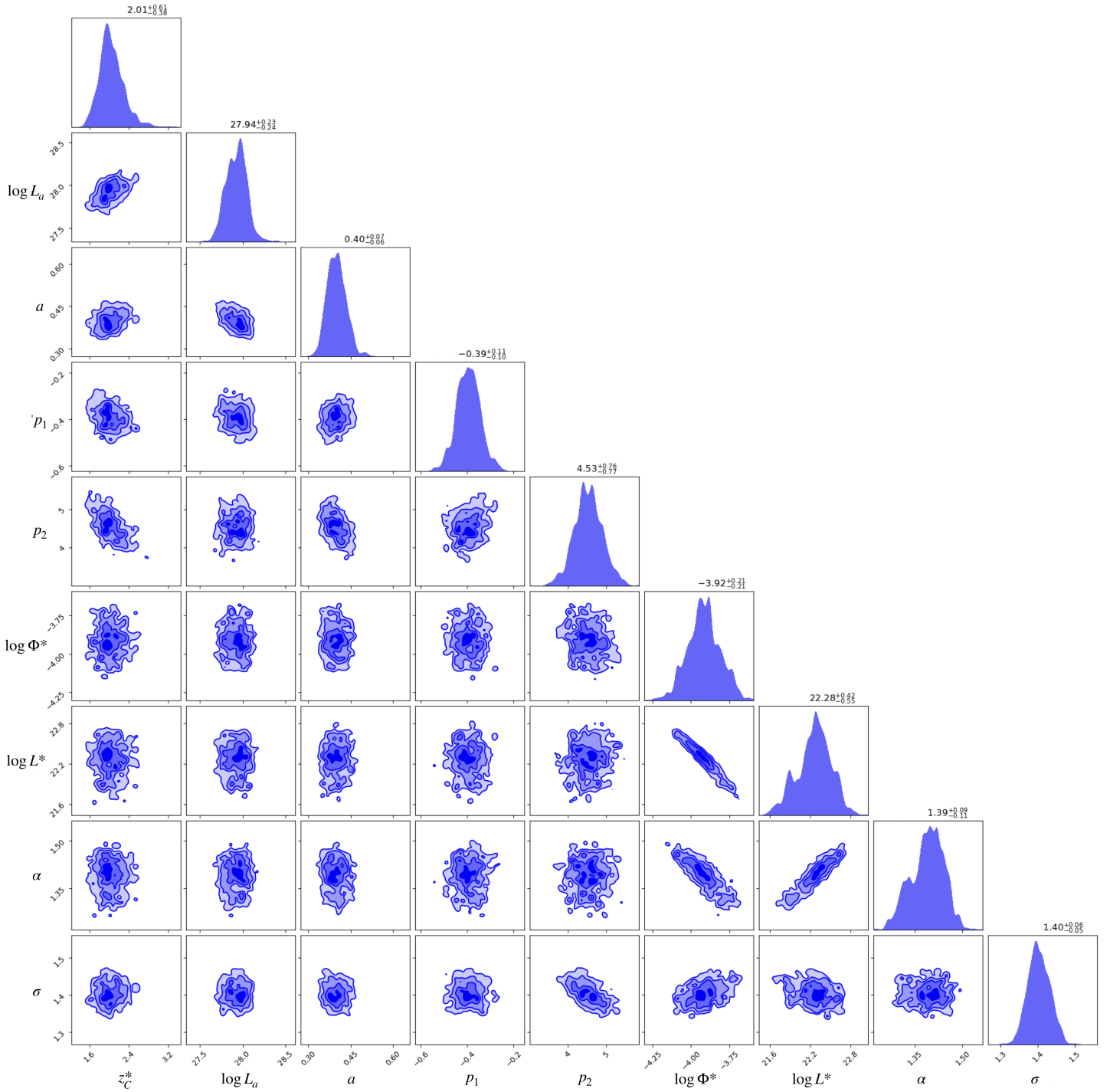


Figure 6.7: The Corner-plot showing the posterior distribution of each parameter of the LDDE model. The resulting samples and weights taken from the posterior were further smoothed as described in Speagle (2020) to obtain the plotted probability density functions.

suming and unnecessary as a simpler method presented itself. Since the fields of intermediate depth in this work are already represented by the XXL-South field, a conservative check was performed by simply omitting the XXL-North field. The re-modeling of the LFs without the XXL-North field gave consistent results. This showed that the uncertainties in the redshifts of the XXL-North field do not modify our results.

Lastly, we examined the choice of the Schechter function for the local LF. We re-modelled the LFs using the double power law function by Dunlop & Peacock (1990) and obtained the same ranking between the evolution models. Overall these checks give us confidence that the model comparison is a true consequence of the data, and not a result of unforeseen biases. Our results, pointing towards the LDDE model being the best one, are therefore robust.

6.5 Comparison with the literature

In Fig. 6.8 we compare the best fitting LDDE model from this work with the LF models, based on the method of maximum volumes, from the literature. Namely we compare them to the LFs from Willott et al. (2001), McAlpine et al. (2013), Smolčić et al. (2017b), Ceraj et al. (2018) and Ocran et al. (2021). The LFs from Willott et al. (2001) are based on the same *3CRR*, *6CE* and *7C* data sets used in this work and already described in Sect. 2.6. They were also used for comparison with the XXL-North non-parametric LFs in Sect. 4.7. The sample from McAlpine et al. (2013) contained 942 sources observed in radio frequencies with the VLA. The sample from Smolčić et al. (2017b) contained 1800 AGN sources from the COSMOS field. Ceraj et al. (2018) LFs were determined also from the COSMOS field, with a sample of 1604 sources. LFs by Ocran et al. (2021) were created from 486 AGNs from the ELAIS N1 field observed at 610 MHz. Since all of these surveys, apart from Willott et al. (2001), model the evolution of LF via PDE or PLE evolution, we show the comparison in two plots, in order to make them more intelligible. The upper plot shows comparison with the PDE evolution models, and the lower shows comparison with the PLE models. Both plots also show LFs from Willott et al. (2001).

It can be seen from the plots that our results are broadly consistent with earlier studies, although some differences are visible. Firstly, no surveys apart from Willott et al. (2001) feature a bump at higher luminosities, which is a feature of our results. On the other hand, although the model from Willott et al. (2001) shows a difference in evolution as a function of luminosity, the exact shape of the LFs is different. There is also a difference between the model from Willott et al. (2001) and all the other models at lower luminosities. This is a result of their sample not being able to constrain these values well, as discussed in their paper. The sample from Willott et al. (2001) contains 356 sources mostly from only the higher luminosity set of our sample.

Since the composite sample used in this work span both high and low luminosities, our results are not affected by this. We repeat again that, although broad consistency between the survey exists, the model selection performed within this work, based on bayesian evidence comparison, shows the LDDE model to be the preferred model (see Tab. 6.1).

6.6 Non-parametric LFs

In Fig. 6.9 we show the LFs created only via the non-parametric method of maximum volumes. These data points trace the AGN sample more directly as no assumption of functional form is required. We show the data points, connected via lines, obtained for different redshift bins, and overlaid on top of each other, in order to make the LF evolution more intelligible. As can be seen from the figure, the evolution is stronger for high luminosity sources. The last redshift bin, with median redshift $z_{Med} = 3.38$, is created using the smallest number of sources, and is therefore less constrained. However, the high redshift LF could also point towards a turnover in density at these redshifts, which is less clear from the modeled LFs.

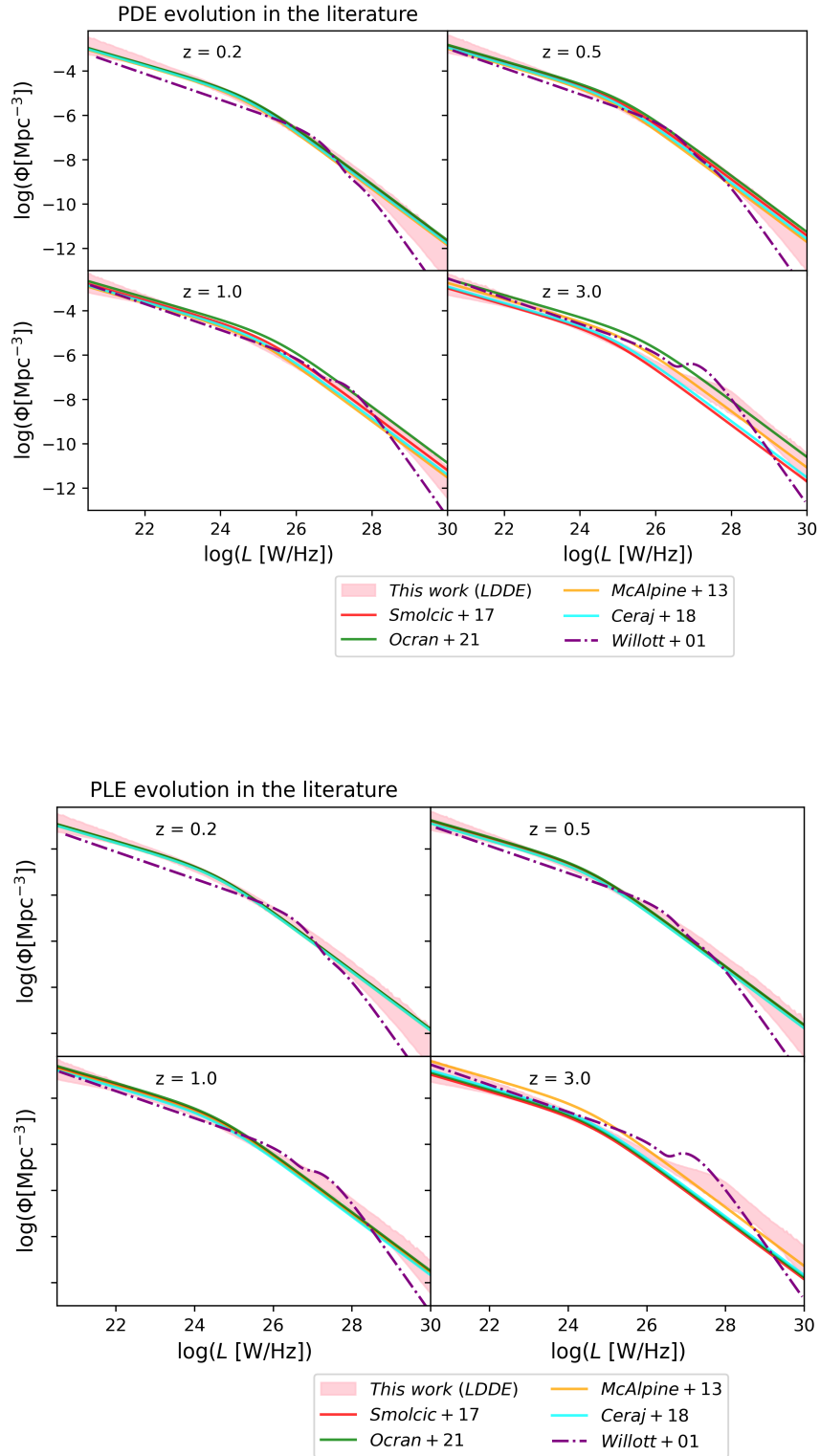


Figure 6.8: Comparison of our LDDE model with the models from literature for PDE and PLE evolution models, as denoted above the figures. The used surveys are denoted in the legend. The results of this work, represented by 90% quantiles are given in pink. The Willott LF shown is the one derived by Willott et al. (2001).

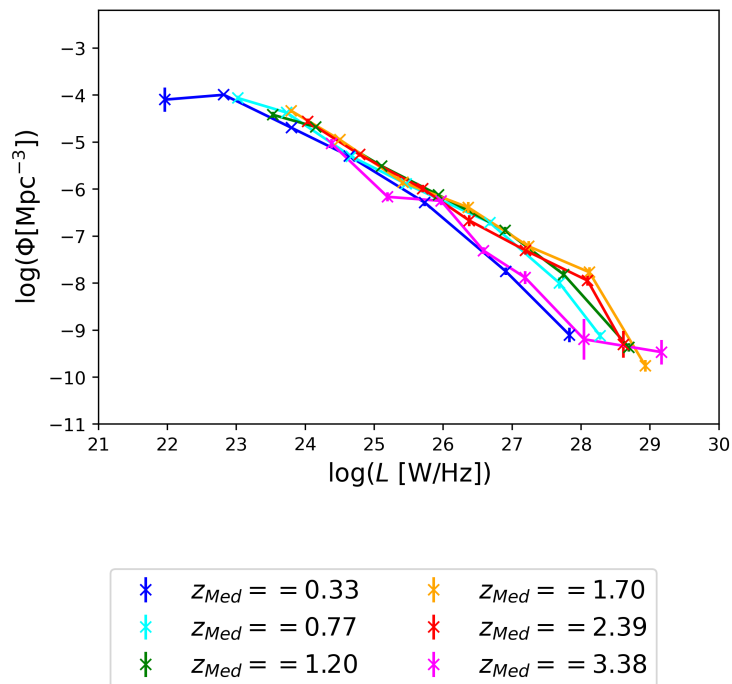


Figure 6.9: The non-parametric LFs determined in different redshift bins via method of maximum volumes, as described in the text (Sect. 5.5), shown overlaid on top of each other, in order to display their evolution. The evolution is stronger for high luminosity sources. The last redshift bin is created using a smaller subsample of sources and is, as described in the text, less credible.

Chapter 7

Discussion

We have modeled the LFs via Bayesian parametric method, using a composite sample consisting of multiple surveys of varying area and depth, which together span a large interval in both redshift and luminosity ($z < 3$ and $\log L \in [22, 29]$). We compared a set of LF models and concluded that by all used criteria, the LDDE model was the preferred one. We now discuss the impact of this result on other physical properties of the AGN sample. Namely, we discuss the number and luminosity density in Sect. 7.1, and the kinetic density of the AGN sample in Sect. 7.2. In Sect. 7.3 we present the source counts of the survey. An investigation into the evolution of AGN sub-population divided according to stellar mas is given in 7.4. The evolution of AGN in the literature, and the place of our results within the broader physical picture are presented in Sect. 7.5, 7.6 and 7.7.

7.1 Number and luminosity density

We estimated the number density and the luminosity density of our AGN sample as a function of redshift, using the best fitting LDDE model. The number density of sources was calculated as:

$$D_N(z) = \int_{L_{Min}}^{L_{Max}} \Phi(L, z) dL \quad (7.1)$$

where the luminosity range was chosen as $\log[L_{Min}, L_{Max}]/(\text{W/Hz}) = [22, 30]$. The luminosity density was calculated as:

$$D_L(z) = \int_{L_{Min}}^{L_{Max}} L \cdot \Phi(L, z) dL \quad (7.2)$$

within the same luminosity range. The resulting number and luminosity densities are shown in Figs. 7.1 and 7.2, respectively. The densities in these figures were extrapolated to a redshift of

$z = 6$, which is beyond the range where we consider the models to be robust (at $z \approx 3$). This was done in order to compare them with the high-redshift quasar studies, from the literature.

First we investigated the estimation of the quasar LF at $z = 6$ from Gloude-mans et al. (2021). Starting from their LF, we determined the number and luminosity density at $z = 6$ via relations (7.1 & 7.2). The LF from Gloude-mans et al. (2021) was estimated by combining the properties of radio quasars at $z = 2$ with the UV-LF at $z = 6$, assuming that the fraction of radio loud quasars remains constant from $z = 2$ to $z = 6$, as described in detail in their paper. Since the LF from Gloude-mans et al. (2021) spans a smaller luminosity range, the number density should be considered a lower limit. When comparing the luminosity densities, this effect is, however, not as important, as the integrated function is multiplied by the value of luminosity.

We performed another comparison with the high-redshift LF of quasars from Saxena et al. (2017). This LF was determined by semi-analytical model predictions within their work. The model used black hole mass functions and Eddington ratio distribution, taking into account the energy losses due to synchrotron, adiabatic and inverse Compton processes, in order to predict the radio LF. It also included radio jets with powers determined via black hole mass and Eddington ratios. As described by Saxena et al. (2017), the radio LF was first compared to observational data at $z = 2$, providing satisfactory results, and then extended to $z = 6$. We used this LF in order to estimate the number and luminosity densities, again via relations 7.1 & 7.2. The resulting data points are shown in the plot.

In the same plots we also show number and luminosity densities determined from LF models of Ceraj et al. (2018) and Smolčić et al. (2017b) via relations 7.1 & 7.2. Again we extrapolate the densities to $z = 6$ in order to compare them with the high-redshift quasar studies, though the LFs are not constrained well at these redshifts. These LF models assume redshift-dependent evolution, in analogy with the model by Novak et al. (2017), denoted as Novak+18 within this work, and described in relation 5.18. The uncertainties plotted in the figure are the maximum between the LFs obtained by changing the parameters of evolution, α and β , between the 1σ uncertainties. It can be seen from the plots that the densities are consistent at lower redshifts, but start to disagree at higher redshifts (of $z \approx 5$). The difference is a direct consequence of the different models used to describe the LFs. A slight difference is also visible for the number density at very low redshifts. This is a consequence of the difference in the local LF.

An interesting consequence of the LDDE model can be seen in the shape of the luminosity density at high redshifts. From the plots it is visible that a flattening occurs, not present in the densities obtained via other models. The reason for this flattening is the bump present in the LDDE model at the high-luminosity end of the sample, or in other words, precisely the luminosity dependence of AGN evolution. To further illustrate this, in Figs 7.1 and 7.2, we

also plot the number and luminosity density using different luminosity ranges, each spanning progressively higher luminosities. Since the flattening occurs only when the upper luminosity boundary is high, it follows that the high luminosity sources, responsible for the bump in the LF model, are also responsible for the flattening of the luminosity density. The maximum values of densities plotted in such luminosity intervals, also change. For luminosity density at 1.4 GHz, these values equal:

$$0.70 \pm 0.05, \quad \log L \in [22, 24] \quad (7.3)$$

$$0.98 \pm 0.04, \quad \log L \in [24, 26] \quad (7.4)$$

$$3.4 \pm 0.2, \quad \log L \in [26, 28] \quad (7.5)$$

$$4.4 \pm 0.4, \quad \log L \in [28, 30] \quad (7.6)$$

The mean values and deviations were estimated by taking 5 random samples from the posterior.

7.2 Kinetic luminosity

In order to assess the energy given to the environment kinetically via work performed by AGN jet expansion, we investigated the kinetic luminosity of our sample. This value, and its change through cosmic time, is important to gain insight into the feedback of AGNs, discussed in Sect. 1.3. Following Ceraj et al. (2018) (see also Smolčić et al. 2017b) we calculated the kinetic luminosity from the radio luminosity following the relation from Willott et al. (1999):

$$\log(L_{Kin}) = 0.86 \cdot \log(L_{1400 \text{ MHz}}) + 14.8 + 1.5 \cdot \log(f) \quad (7.7)$$

where f was introduced by Willott et al. (1999) in order to incorporate all the possible systematic errors, and was determined to be in the range 1 – 20. The uncertainties are large enough to also include the star-forming component of radio emission. Following Ceraj et al. (2018), we set it to 15. We note, however, that the value of this number shifts the kinetic luminosity systematically on the y-axis, not affecting the shape of the function. In other words, it changes only the normalisation of the function. Any trends inferred from the kinetic luminosity density therefore remain the same. The kinetic luminosity density as a function of redshift was now determined as:

$$D_{kin}(z) = \int_{L_{Min}}^{L_{Max}} L_{kin} \cdot \Phi(L, z) dL \quad (7.8)$$

We again used the parameter samples from the LDDE model posterior for the LF, $\Phi(L, z)$. The resulting plot of kinetic luminosity is shown in Fig. 7.3. Apart from our observational

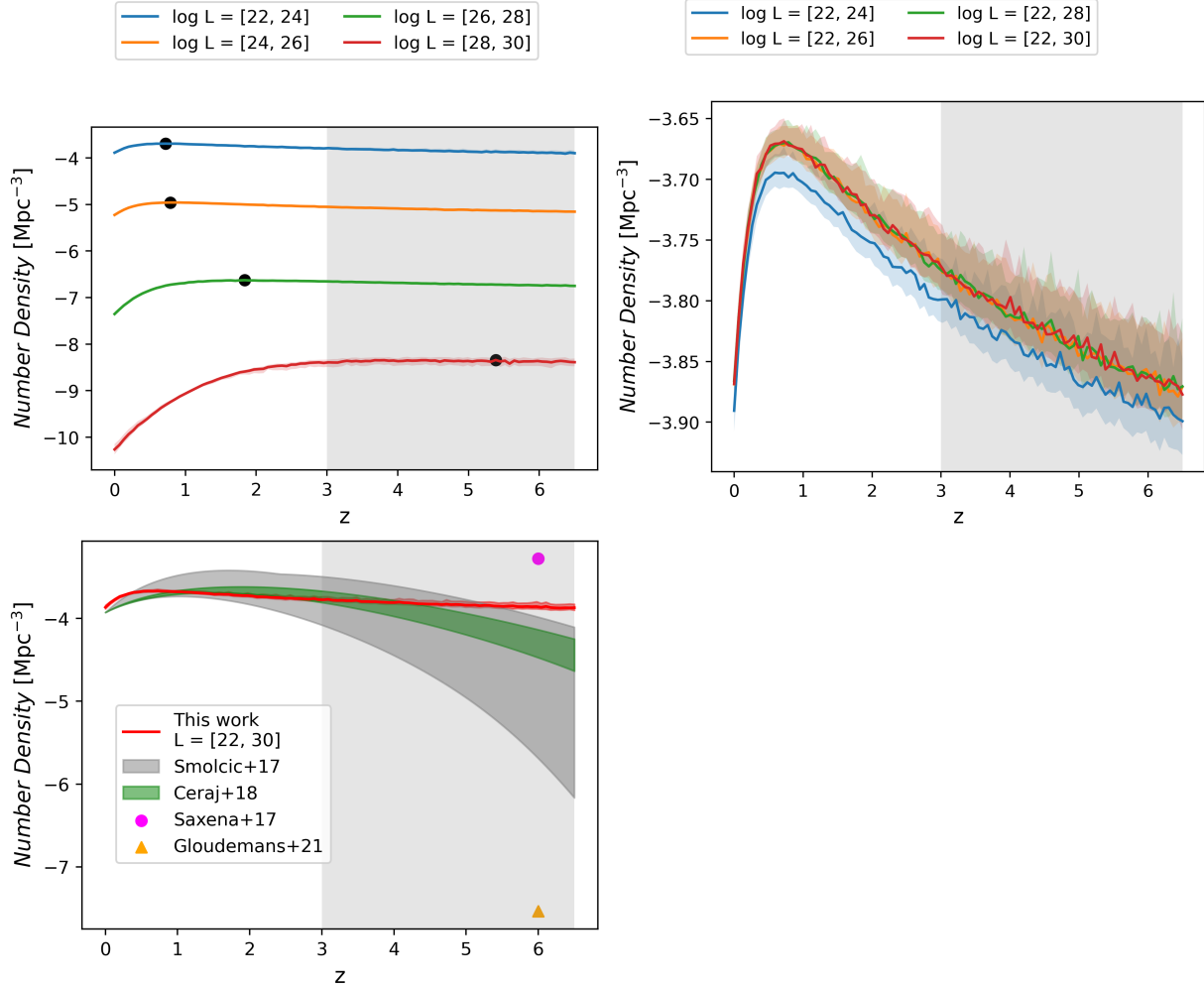


Figure 7.1: *Upper left panel:* Number density calculated at 1.4 GHz, for a set of different luminosity ranges of same width, as denoted in the legend above the figure. The black dots represent the maximum value of each line. *Upper right panel:* Number density at 1.4 GHz calculated for a set of progressively increasing luminosity ranges, as denoted in the legend above the figure. *Lower panel:* Number density at 1.4 GHz as a function of redshift for a set of different surveys, denoted in the legend. The data-points denote the high-redshift quasar surveys as described in the text. The uncertainties in this work are calculated from the resulting samples within the parametric Bayesian method as 90% quantiles. The uncertainties of the literature values are determined as maximum uncertainties obtained by shifting the LF parameters, as described in the text. The shaded area in the plots denote higher redshifts, where the LF models are less constrained. The high-redshift quasar density from Gloude-mans et al. (2021) is a lower limit as the luminosity range of the LF used in the calculation was smaller.

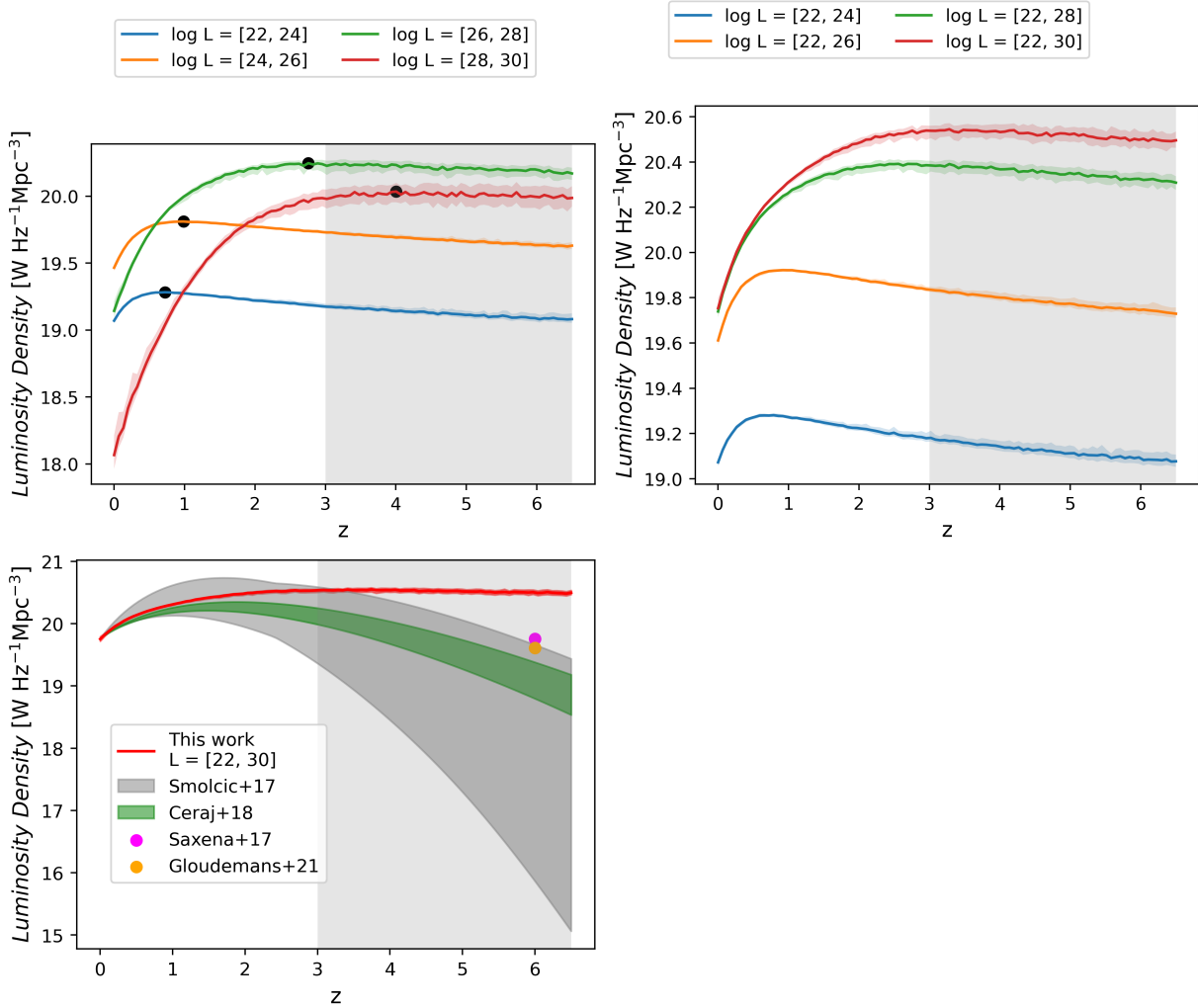


Figure 7.2: *Upper left panel:* Luminosity density at 1.4 GHz calculated for a set of different luminosity ranges of same width, as denoted in the legend above the figure. The black dots represent the maximum value of each line. *Upper right panel:* Luminosity density at 1.4 GHz calculated for a set of progressively increasing luminosity ranges, as denoted in the legend above the figure. *Lower panel:* Luminosity density at 1.4 GHz as a function of redshift for a set of different surveys, denoted in the legend. The data-points denote the high-redshift quasar surveys as described in the text. The uncertainties in the figure follow those in Fig. 7.1. The shaded area in the plots denote higher redshifts, where the LF models are less constrained.

results, we also show the estimated kinetic luminosity density obtained from two models: the GALFORM model (Fanidakis et al. 2012) and the SAGE model (Croton et al. 2006). The GALFORM model assumes two different modes of black hole accretion and subsequently two different evolution modes through cosmic time. The first mode is the starburst mode where accretion arises from galaxy mergers or instabilities within the disk. The second mode is the hot-halo mode accreting matter from the hot halo onto the central black hole. An interesting aspect of the GALFORM model, as seen from the figure, is the flattening between the observed kinetic luminosity and the total and starburst modes of the GALFORM model at redshifts $z \approx 3 - 4$, not present in the SAGE model. The SAGE model, which includes the feedback mechanism, has black hole accretion rate \dot{m} as one of its results. Following Croton et al. (2016) and Ceraj et al. (2018), we calculated the kinetic luminosity from this value as: $0.1 \cdot \dot{m} \cdot c^2$ multiplying this by 0.08 which was the radio mode efficiency parameter. The factor 0.1 is the standard value found in the literature, falling between the efficiency expected for a non-spinning and maximally spinning black hole (Croton et al. 2016). Our comparison with the SAGE model gives non-consistent results. Even if we ignore the absolute values of the functional forms, which can be explained with the uncertainty factor f given in relation (7.7), the shape, or the redshift dependence of the functions, is different between the model and observations. Furthermore, Fig. 7.3 shows that the two models themselves give different kinetic luminosity estimates. The differences between models themselves, and between the models and our observational results, are likely due to the assumptions made in the models.

7.3 Source counts

Using the best fitting LDDE model, we constructed the AGN source counts of our sample. We show the AGN source counts in Fig. 7.4, obtained from the resulting LF, by selecting 500 samples from the posterior. From the definition of the LF $\Phi(L, z)$, the number of sources ΔN in each flux bin at a certain value of redshift was obtained as:

$$\Delta N = \Phi(L, z) \frac{dV}{dz} \Delta \log L dz, \quad (7.9)$$

where dV/dz is the differential co-moving volume, $\Delta \log L$ luminosity decade and dz the redshift bin. The number of sources obtained in each flux bin was summed over all redshift bins and then normalized with counts expected in a static Euclidean Universe. For comparison, we also show source counts from an earlier study by Vernstrom et al. (2014) and the model obtained from the LF evolutionary model by Novak et al. (2018), as this is the model constrained by the

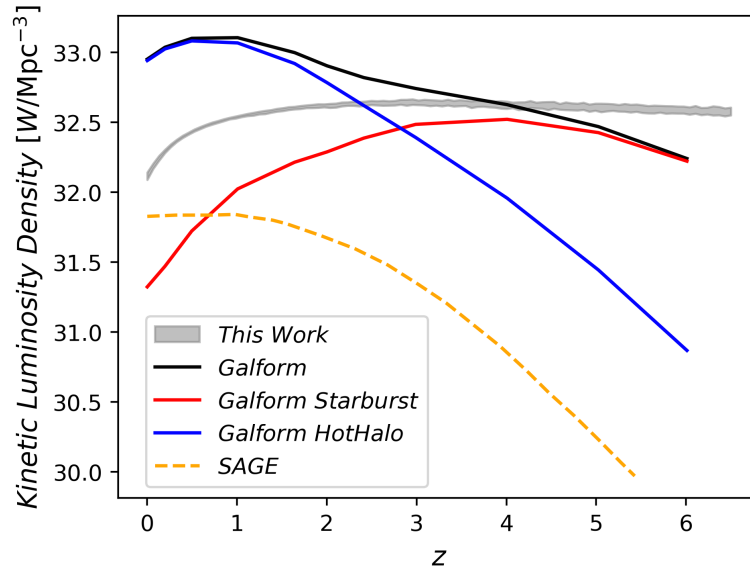


Figure 7.3: Kinetic luminosity density as a function of redshift given in grey. The uncertainties are calculated from the resulting samples of the parametric method as 90% quantiles. Black red and blue lines correspond to the predictions from GALFORM. The black line is the total density, while the red and blue lines denote the hot-halo and starburst modes, respectively. The orange dashed line represents the SAGE model.

deeper COSMOS survey, and as such constrains the low luminosity end of the sample best. The source counts by Vernstrom et al. (2014) were obtained from 3 GHz data observed by Karl G. Jansky Very Large Array, directed towards the Lockman Hole. They were constructed using the method of probability of deflection to reach deeper values of flux, as described in the paper. The model by Novak et al. (2018) was constructed from the LFs that have pure luminosity evolution, with different parameters, for SFGs and the AGN population, as described in detail in their paper. The source counts from this work are in good agreement with both these surveys. We also show data points created from the surveys with no model assumptions, as denoted in the legend. The data points are also consistent with our model, ignoring the obvious faint outliers, arising from the finite detection limits of each survey.

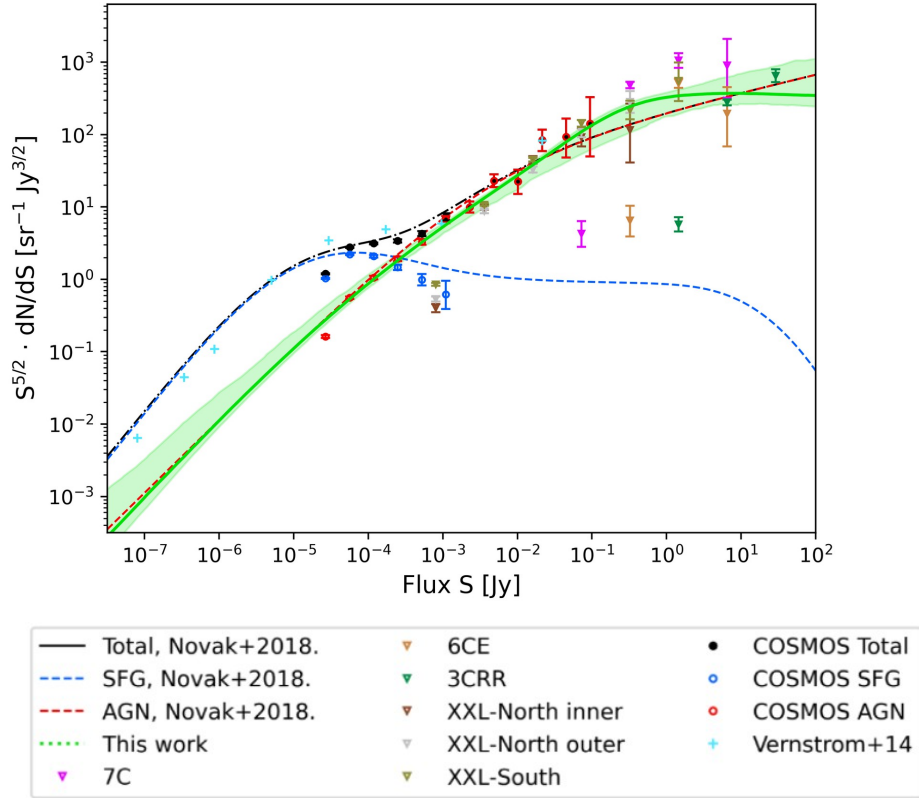


Figure 7.4: The source counts model together with data points obtained directly from the catalogues. The green dashed line denotes the model obtained from LFs constrained within this work. The errors were determined by selecting 500 samples from the posterior. The red, blue and black lines denote models from Novak et al. (2018) obtained from LFs for AGN, SFG and the total population respectively. Data-points represent the source counts obtained from the catalogues as denoted in the legend. All the catalogues are the same as described in Sect. 2.6 except the ones denoted as Vernstrom+14, which were taken from another study by Vernstrom et al. (2014). COSMOS SFG are sources from the COSMOS catalogue not selected by the radio excess threshold described in Sect. 2.6. The outlier data points are the effect of finite detection limits.

7.4 Stellar mass dependent difference in evolution

We next investigated the dependence of the LF evolution on stellar mass of the AGN host galaxies. In order to do this, we divided our sample into two sub-populations of high and low mass galaxies. Since the XXL-North survey contained no stellar mass estimates, we excluded it from these considerations. Here we reasoned that the intermediate surveys are already constrained by the XXL-South field, so this simplification should not affect the results. The stellar mass estimates for the COSMOS field are taken from the COSMOS2015 catalogue (Laigle et al. 2016) and are calculated by using the "LePhare" program package (Arnouts et al. 2002, Ilbert et al. 2006), as described in Laigle et al. (2016). The XXL-South field stellar mass estimates are determined by SED fitting as described in Butler et al. (2018b). The fields from Willott et al. (2001) lacked stellar mass estimates but contained apparent K-band magnitudes, via a publicly available catalogue¹. The complete publicly available catalogue, for all three shallow fields 7C, 6CE and 3CRR, contained 181 sources. The 7C had complete K-band magnitudes at $z > 1.2$, so a threshold was imposed on this data set, and a correction made during the calculation of likelihood. The 3CRR field had 69/96 sources with K-band magnitudes at $z > 0.05$. This incompleteness was incorporated via a correction function to the likelihood function. The 6CE field had complete K-band magnitude data. The details on the catalogues are found in Willott et al. (2003). In order to estimate the stellar masses of the radio sources in these surveys, we used the relationship between the stellar mass of the galaxy and its K-band magnitude reported in the literature (e.g. Arnouts et al. 2007). Since we are dealing with a sub-population of pure AGNs, we re-calibrated the stellar mass to K-band correlation. For this purpose, we used the COSMOS2015 catalogue that contains both the stellar masses and the K-band magnitude data. We took a subset of the catalogue containing only AGNs, based on radio excess, as previously described in Sect. 2.5, and re-plotted the dependence of stellar mass on the absolute K-band magnitude. We show this in Fig 7.5. Following Arnouts et al. (2007) we allowed for a redshift dependent correlation via two free redshift-dependent parameters as: $M^* = a(z)K + b(z)$. First we performed a linear regression fit on every redshift subset independently. The resulting parameters a and b differed across redshift bins. By performing another linear regression on these values we assessed the redshift dependence of the parameters. The resulting correlation parameters thus equalled:

$$a(z) = 0.0224 \cdot z - 0.503 \quad (7.10)$$

$$b(z) = 0.3226 \cdot z - 0.711 \quad (7.11)$$

¹<https://astroherzberg.org/people/chris-willott/research/>

Having once obtained all of the stellar mass estimates we divided the complete AGN sample into sub-samples with high and low stellar masses, and constructed the LFs from each subsample. Furthermore to eliminate any systematic error arising from the incompleteness of our sample due to a finite detection limit, we removed the lowest-mass galaxies from our sample. The two stellar mass sub-populations therefore spanned mass intervals of $\log(M^*) \in [10.2, 11]$ and $\log(M^*) > 11$, ranging in log-luminosities at 1400 MHz, for both subsets, from ≈ 22 to ≈ 28 . The difference in evolution can be seen in Fig. 7.6. We modelled the evolution as a simple PDE evolution since we were interested only in tracing the difference between the sub-populations. The difference in evolution exists and is larger than the 68.2 quantiles plotted in the figure. The parameter of PDE evolution, given via equation (5.17) equalled $\alpha_D = 0.23^{+0.13}_{-0.13}$ for the low-mass sample and $\alpha_D = -0.38^{+0.11}_{-0.12}$ for the high-mass. The differences between the sub-samples arise also as a result of the complete LF shape. As a final precaution, we repeated the LF fitting without the 7C survey, since this survey had the largest incompleteness. The results remained qualitatively the same. Overall, the difference in LFs could point towards a possible bimodality within our AGN sample which is a function of host galaxy stellar mass. The details of this bimodality, however, need to be investigated further.

7.5 Evolution of AGN sub-populations in the literature

We now discuss the resulting luminosity dependent evolution model, or the LDDE model, which in this work was argued to fit the radio AGN data set best, in comparison with the surveys from the literature. The difference in the evolution of the high and low luminosity end of the sample is reported throughout the literature (Waddington et al. 2001, Willott et al. 2001, Clewley & Jarvis 2004, Sadler et al. 2007, Smolčić et al. 2009, Donoso et al. 2009, Padovani et al. 2017). There are however differences in the adopted LF models. As already stated, Willott et al. (2001) use a bimodal model where the shape and evolution of the high and low luminosity end have a different functional form. Smolčić et al. (2009) model only the low-end of the AGN sample using a superposition of luminosity and density evolution, analogous to relation 5.17, showing a modest evolution of this sample compared to high-luminosity studies. Furthermore, studies are often performed via non-parametric methods (e.g. Waddington et al. 2001, Sadler et al. 2007, Donoso et al. 2009, Rigby et al. 2015) so no functional form is assumed for the LF. Even so, there is a difference in evolution in these surveys which seems to be a function of luminosity. This makes them consistent with our work. The comparison here is simple as all of these surveys find change in evolution with source luminosity.

Even when the classification is not identical, trends in AGN evolution can be compared.

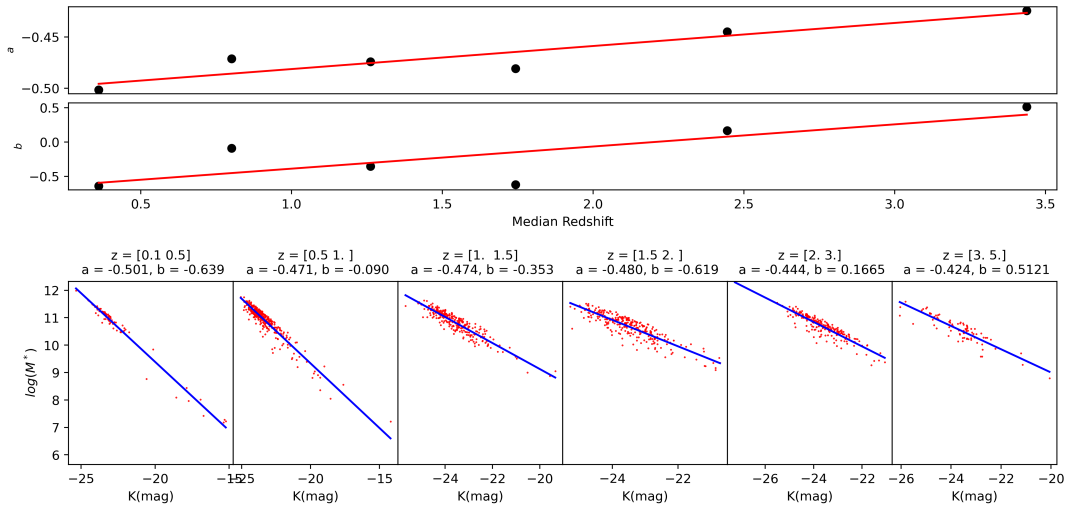


Figure 7.5: The calibration of mass-to-light correlation between the absolute K-band magnitude and stellar mass obtained from the COSMOS2015 catalogue for the subset of AGN sources. The assumed functional form of the correlation is $M^* = a(z)K + b(z)$ as described in the text. *Bottom:* The dependence of stellar mass M^* on K-band magnitude. The blue line shows the linear regression fit performed for each redshift bin independently. The range of each redshift bin is given above the corresponding plot, as well as the resulting correlation parameters. *Top:* The resulting correlation parameters as a function of redshift. The red line shows the linear regression performed on these values in order to determine the redshift dependence of the parameters.

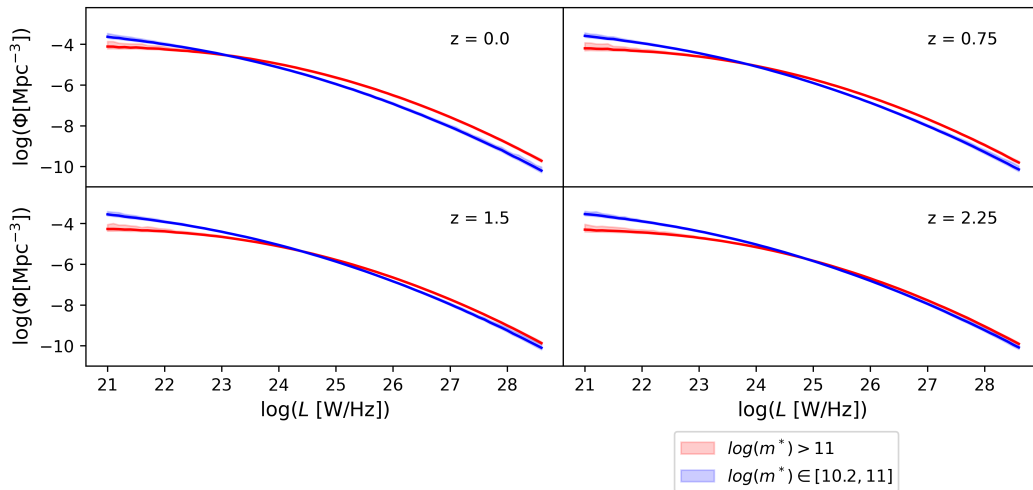


Figure 7.6: LFs for the high and low mass sub-sample. The uncertainty plotted in the figure is the 68.2 quantile. The model of evolution is the PDE model. The redshift of each subplot is given in the figure.

For instance, a difference in evolution between two subsets of AGN was observed in a study by Pracy et al. (2016) using the Faint Images of the Radio Sky at Twenty-cm survey matched with the Sloan Digital Sky Survey. The complete AGN sample, was divided into HERGs and LERGs based on optical spectra. There was an observed difference in evolution in the double power-law LF assuming alternatively both PDE or PLE evolution, where the LERG population evolved slowly as opposed to the more rapid evolution of the HERG sub-sample. Although the comparison is not exact, due to a difference in classification, this difference in evolution is consistent with our results where the evolution depends on luminosity. The reason is that different sub-populations of AGNs can have different luminosities. Here HERGs would correspond roughly to the high luminosity end of the sample, and LERGs to the low luminosity end, so a difference in evolution between these two sub-populations is consistent with a AGN evolution changing as a function of luminosity. We discuss this idea in more detail in the next section.

Padovani et al. (2015) divided their Extended Chandra Deep Field-South Very Large Array sample into RQ and RL AGN based on relative strength of radio emission at 1.4. GHz as described in the text. RL AGNs correspond mostly to jet-mode AGNs, and RQ to radiative mode. A difference in evolution between these two sub-populations was observed, where the RL sample exhibited a peak at $z = 0.5$ after which their numbers declined as opposed to the RQ sample. These findings also point towards some difference in evolution of AGN sub-populations, and are therefore again consistent with this work.

A study by Ocran et al. (2021) of the ELAIS N1 field observed with the GMRT at 610 MHz divided the complete sample into RQ and RL AGN, based on a combination of multi-wavelength criteria as described in their text. The evolution was modeled as PLE for the sub-samples and a difference in evolution was observed, where RL AGN evolved more strongly. This is again consistent with our results.

Similar conclusions concerning AGN evolution are also obtained within X-ray astronomy. An example is the study by Fotopoulou & Paltani (2018), using a composite set of fields: MAXI, HBSS, XMM-COSMOS, Lockman Hole, XMM-CDFS, AEGIS-XD, Chandra-COSMOS, and Chandra-CDFS. The LFs were modeled using an AGN sample observed within the X-ray part of the spectrum in the 5 – 10 keV band. The model comparison was done also within the Bayesian framework, comparing AIC and BIC, resulting in LDDE being the best-fitting model.

7.6 LDDE model within the picture of AGN bimodality

As described in Ch. 1, and in the last section, a trend throughout the literature is the separation of the full AGN sample into sub-samples, be it RL and RQ, based on the relative strength of

the radio emission (e.g., Padovani et al. 2015), high HERG and LERG, based on optical spectral lines (Butler et al. 2019), or any other criterion. Although the LDDE model, preferred in this work, assumes a continuous change in evolution with regards to luminosity, this does not exclude the existence of two AGN sub-populations. Firstly, the strength of the model selection criteria between the model from Willott et al. (2001) and LDDE is not as strong compared to the simple PDE and LDE models, and the difference could be a consequence of the larger number of parameters of the Willott model. More importantly, if the sub-populations are not selected with a simple luminosity threshold, but by some other criteria, different fraction of each population can be present at different luminosities. This could lead to the observed continuous change in evolution with luminosity, present in the LDDE model. Concentrating on the underlying physical processes, our results are therefore consistent with the picture outlined in the introduction, assuming two distinct modes of accretion: the radiatively efficient mode, and the radiatively inefficient mode (Hardcastle et al. 2007, Heckman & Best 2014, Narayan et al. 1998, Shakura & Sunyaev 1973). Although the analogies are not exact, the radiatively efficient mode would correspond to the high luminosity end of the AGN sample and the HERG sub-sample, while the radiatively inefficient mode to the low luminosity end and the LERG sub-sample.

Another possibility (as discussed by e.g. Waddington et al. 2001) is the physical picture where the underlying physics does not require two distinct modes of accretion but some underlying parameter determining the evolution, and causing continuous difference in evolution as a function of source luminosity. Within this work we cannot exclude such a scenario. On the other hand, it is also important to repeat that the PDE and PLE models, and their superposition, were deemed within this work to be too simple to describe the radio AGN evolution. It follows that AGN evolution is a more complex process than assumed by these models.

7.7 LDDE model, Downsizing and Feedback

We now "re-sketch" the complete physical picture of galaxy evolution, discussed in Ch. 1 and discuss our results within this picture. As stated, the described trend of different AGN evolutions and cutoffs can be explained via cosmic downsizing, where the more massive black holes form earlier than the less massive ones (e.g., Rigby et al. 2015). As described in Ch. 1, this trend is, at first glance, not consistent with the hierarchical model, where larger black holes are the product of merging, but the apparent inconsistency can be explained by a switch in the mode of accretion between the efficient cold gas accretion to inefficient hot gas accretion, via AGN feedback. The main effect of AGN feedback is thought to be the quenching of both star formation in the galaxy and the growth of the black hole, as the gas needed to fuel these processes is removed, or at least

prevented to cool. The galaxies turn to red galaxies with little star formation and the inefficient accretion starts to dominate at low redshifts (e.g., Heckman & Best 2014, Rigby et al. 2015). It follows that the accretion onto the central black hole of the galaxy is a complex process, or an interplay between gas inflow and AGN feedback. Since AGN feedback both influences the galaxy and AGN evolution, which in this physical interpretation are tightly connected, and scales with accretion onto the black hole, it is reasonable to expect that the evolution of AGNs changes with luminosity. Since in this work we argue for a luminosity dependent evolution of AGN, via the LDDE model, it is therefore consistent with a physical picture requiring AGN feedback. In summary, difference in evolution as a function of AGN luminosity shows that the physics of AGN evolution depends on the accretion rate. This is in turn consistent with the picture of AGN accretion which incorporates feedback. This also places our results in line with other publications where feedback was either deduced indirectly via scaling relations of the host galaxy and its black hole (Magorrian et al. 1998, Ferrarese & Merritt 2000, Gebhardt et al. 2000, Graham et al. 2011, Sani et al. 2011, Beifiori et al. 2012, McConnell & Ma 2013), or observed more directly via galactic winds (e.g., Nesvadba et al. 2008, Feruglio et al. 2010, Veilleux et al. 2013, Tombesi et al. 2015) or X-ray cavities in galactic groups and clusters (Clarke et al. 1997, Rafferty et al. 2006, McNamara & Nulsen 2007, Fabian 2012, Nawaz et al. 2014, Kolokythas et al. 2015). It also places our results in line with theoretical work where the need for AGN feedback was supported by simulations (Fanidakis et al. 2012, Hirschmann et al. 2012, Croton et al. 2016, Harrison et al. 2018).

Chapter 8

Thesis summary and outlook

8.1 Summary of this Thesis

In this thesis we investigated the evolution of AGN through cosmic time, by modeling their radio LFs, both via parametric and non-parametric methods. The complete data set used in this thesis contained multiple surveys of varying area and depth, namely the COSMOS, XXL-North, XXL-South, 7C, 6CE and 3CRR surveys, consisting all together of 4,655 sources. This allowed us to constrain the LFs both at high redshifts (up to $z \approx 3$) and at high luminosities ($\log L \in [22, 29]$).

8.1.1 XXL-North LFs

First we concentrated solely on the data from the XXL-North field. The radio data came from observations with the Giant Metrewave Radio Telescope (GMRT), at 610 MHz. The radio catalogue was cross-correlated with a multi-wavelength catalogue, in order to obtain a sample of sources with photometric redshifts. The matching between the catalogues was performed using the likelihood ratio method, which selected the counterparts of the radio sources using both their positions and magnitudes. This process resulted in a catalogue of 1150 sources, whose radio emission is dominated by AGN processes (at $z \leq 2.1$, $S_{610 \text{ MHz}} > 1 \text{ mJy}$), covering intermediate luminosities ($23 \lesssim \log(L_{1.4 \text{ GHz}} [\text{W/Hz}]) \lesssim 28$).

Using the matched catalogue we constructed the LFs of the XXL-North field data set, using a non-parametric method of maximum volumes. The constructed LFs were compared to the LFs from the literature created via non-parametric methods, and to a model by Willott et al. (2001). The model assumed a different evolution for the high and low luminosity end of the AGN sample. The LFs determined in this thesis from the XXL-North data, are in agreement

with a double-population model from Willott et al. (2001), or, in other words, are consistent with bimodal evolution of AGN. In summary, they are consistent with the picture of AGN evolution in which the high-luminosity end of the AGN sample evolves faster than the low-luminosity end.

8.1.2 Composite field LFs

Modeling of the LFs with parametric methods was performed for a complete set of surveys, taken together as a composite survey of varying area and depth. These were the COSMOS, XXL-North, XXL-South, 7C, 6CE and 3CRR fields. The separate fields, used as a composite survey, consisted all-together of 4,655 sources. The LF modeling was performed within the Bayesian framework by determining the likelihood and calculating the posterior probabilities of model parameters. A wide selection of models, with different shape of the local LF, and different evolution through cosmic time, were investigated. More specifically, we investigated change in AGN number density (PDE model), change in AGN luminosity (PLE model) and a superposition of both (Sadler+02 model). Furthermore, we examined a model assuming redshift dependence on evolution (Novak+17 model) and a model assuming luminosity dependence on evolution, denoted within this thesis as the LDDE model. We also examined a purely bimodal model assuming different evolution and LF shape for the high and low luminosity end of the AGN sample (Willott+01 model). Apart from determining the values of the model parameters, the parametric method allowed us to compare between models and select the best fitting one. The best fitting model according to marginal likelihood comparison, as well as the AIC and BIC methods, was the LDDE model. Using the Jeffrey's interpretation, evidence ratios varied from "strong" (> 10) to "decisive" (> 100).

8.1.3 Implications of the LDDE model

The dependence of shape and evolution of the LFs on luminosity assumed by this model was discussed in its implications on the physical picture of AGN evolution through cosmic time. We discussed the number density and luminosity density as a function of redshift. The shape of the best fitting LDDE model resulted in a flattening of luminosity density at higher redshifts that is not present in simpler models with pure density or luminosity evolution. We compared these results with high-redshift quasar surveys and found broad consistency, though the LFs from this work are not constrained well at these redshifts.

We calculated the kinetic luminosity density and compared it to model-estimated values finding some consistency with the GALFORM simulation, namely the flattening of the func-

tions at $z \approx 3 - 4$. The calculated kinetic luminosity density was not consistent with the SAGE model, either in shape or normalisation. The difference between our results and the models, and between the models themselves was attributed to the assumptions made within the models, and the observational results.

In order to assess the dependence of stellar-mass of host galaxies on AGN evolution, we divided our sample into subsets of different stellar mass and modelled the evolution using a simpler PDE model. The difference in LFs was observed that was larger than 65% quantiles estimated from posterior samples, as well as a difference in evolution parameters.

Lastly we discussed the possibility of AGN sub-populations. Although the change in evolution as a function of luminosity is continuous, this does not exclude the possibility of AGN sub-populations as different fractions of each sub-population can be found at different luminosities. Taken together, all these results point towards a physical picture of AGN evolution where a simple density evolution, luminosity evolution or a superposition of both is not enough to trace the details of AGN evolution. More complex models, either consisting of AGN sub-populations, or including a dependence on AGN luminosity, are needed.

8.1.4 Outlook

The LDDE model, argued within this work to fit the radio AGN sample best, suggest that models describing AGN LFs need to be more complex than simple density and luminosity evolution models, found often in the literature. It also suggests further need for investigating possible AGN sub-populations, selected via different physical criteria. Possible differences in evolution between the sub-populations could give insight into the physics of AGN, and galaxy evolution as a whole.

The LDDE radio AGN LF model, presented here, describes the density of radio-detected AGN, as a function of redshift. The model was constrained parametrically, using for the first time a composite set of surveys reaching simultaneously such large areas and depths. The LFs were constrained up to redshifts of $z \sim 3.5$, and spanning 1400 MHz luminosities of $\log(L/\text{WHz}^{-1}) \in [22, 29]$. Starting from this model, it is therefore possible for other studies to estimate the number of radio-detected AGNs through cosmic time.

References

- Adami C., et al., 2018, A&A, 620, A5, *The XXL Survey. XX. The 365 cluster catalogue*
- Aird J., et al., 2010, MNRAS, 401, 2531, *The evolution of the hard X-ray luminosity function of AGN*
- Akaike H., 1974, IEEE Transactions on Automatic Control, 19, 716, *A New Look at the Statistical Model Identification*
- Antonucci R., 1993, ARA&A, 31, 473, *Unified models for active galactic nuclei and quasars.*
- Arnouts S., et al., 2002, MNRAS, 329, 355, *Measuring the redshift evolution of clustering: the Hubble Deep Field South*
- Arnouts S., et al., 2007, A&A, 476, 137, *The SWIRE-VVDS-CFHTLS surveys: stellar mass assembly over the last 10 Gyr. Evidence for a major build up of the red sequence between $z = 2$ and $z = 1$*
- Avni Y., Bahcall J. N., 1980, ApJ, 235, 694, *On the simultaneous analysis of several complete samples - The V/V_{max} and V_e/V_a variables, with applications to quasars*
- Becker R. H., White R. L., Helfand D. J., 1995, ApJ, 450, 559, *The FIRST Survey: Faint Images of the Radio Sky at Twenty Centimeters*
- Beckman, V. and Shrader, C. 2012, *Active Galactic Nuclei*. WILEY-VCH Verlag GmbH & Co. KGaA, Weinheim, Germany
- Beifiori A., Courteau S., Corsini E. M., Zhu Y., 2012, MNRAS, 419, 2497, *On the correlations between galaxy properties and supermassive black hole mass*
- Best P. N., Heckman T. M., 2012, MNRAS, 421, 1569, *On the fundamental dichotomy in the local radio-AGN population: accretion, evolution and host galaxy properties*
- Bock D. C. J., Large M. I., Sadler E. M., 1999, AJ, 117, 1578, *SUMSS: A Wide-Field Radio Imaging Survey of the Southern Sky. I. Science Goals, Survey Design, and Instrumentation*
- Bondi M., et al., 2003, A&A, 403, 857, *The VLA-VIRMOS Deep Field. I. Radio observations probing the μ Jy source population*
- Bonzini M., et al., 2012, ApJS, 203, 15, *The Sub-mJy Radio Population of the E-CDFS: Optical and Infrared Counterpart Identification*
- Bouwens R. J., et al., 2012, ApJ, 754, 83, *UV-continuum Slopes at $z \sim 4-7$ from the HUDF09+ERS+CANDELS Observations: Discovery of a Well-defined UV Color-Magnitude Relationship for $z \geq 4$ Star-forming Galaxies*
- Boyle B. J., Shanks T., Peterson B. A., 1988, MNRAS, 235, 935, *The evolution of optically selected QSOs. II*
- Brusa M., et al., 2007, ApJS, 172, 353, *The XMM-Newton Wide-Field Survey in the COSMOS Field. III. Optical Identification and Multiwavelength Properties of a Large Sample of X-Ray-Selected Sources*
- Burke B., Graham-Smith F., Wilkinson P., 2019, *An introduction to radio astronomy*. Cambridge University Press, <https://books.google.hr/books?id=1OKfDwAAQBAJ>
- Butler A., et al., 2018a, A&A, 620, A3, *The XXL Survey. XVIII. ATCA 2.1 GHz radio source catalogue and source counts for the XXL-South field*
- Butler A., et al., 2018b, A&A, 620, A16, *The XXL Survey. XXXI. Classification and host galaxy properties of 2.1 GHz ATCA XXL-S radio sources*

- Butler A., Huynh M., Kapińska A., Delvecchio I., Smolčić V., Chiappetti L., Koulouridis E., Pierre M., 2019, *A&A*, 625, A111, *The XXL Survey. XXXVI. Evolution and black hole feedback of high-excitation and low-excitation radio galaxies in XXL-S*
- Cannon R., et al., 2006, *MNRAS*, 372, 425, *The 2dF-SDSS LRG and QSO (2SLAQ) Luminous Red Galaxy Survey*
- Carroll B., Ostlie D., 2014, *An introduction to modern astrophysics*. Pearson custom library, Pearson, <https://books.google.hr/books?id=RLwangEACAAJ>
- Cattaneo A., et al., 2009, *Nature*, 460, 213, *The role of black holes in galaxy formation and evolution*
- Ceraj L., et al., 2018, *A&A*, 620, A192, *The VLA-COSMOS 3 GHz Large Project: Star formation properties and radio luminosity functions of AGN with moderate-to-high radiative luminosities out to $z = 6$*
- Chartas G., Hamann F., Eracleous M., Misawa T., Cappi M., Giustini M., Charlton J. C., Marvin M., 2014, *ApJ*, 783, 57, *Magnified Views of the Ultrafast Outflow of the $z = 1.51$ Active Galactic Nucleus HS 0810+2554*
- Cheung E., et al., 2016, *Nature*, 533, 504, *Suppressing star formation in quiescent galaxies with supermassive black hole winds*
- Christlein D., Gawiser E., Marchesini D., Padilla N., 2009, *MNRAS*, 400, 429, *Introducing the photometric maximum likelihood method: galaxy luminosity functions at $z < 1.2$ in MUSYC-ECDFS*
- Cicone C., Brusa M., Ramos Almeida C., Cresci G., Husemann B., Mainieri V., 2018, *Nature Astronomy*, 2, 176, *The largely unconstrained multiphase nature of outflows in AGN host galaxies*
- Cilieggi P., Zamorani G., Hasinger G., Lehmann I., Szokoly G., Wilson G., 2003, *A&A*, 398, 901, *A deep VLA survey at 6 cm in the Lockman Hole*
- Cilieggi P., et al., 2018, *A&A*, 620, A11, *The XXL Survey. XXVI. Optical and near-infrared identifications of the ATCA 2.1 GHz radio sources in the XXL-S Field*
- Clarke D. A., Harris D. E., Carilli C. L., 1997, *MNRAS*, 284, 981, *Formation of cavities in the X-ray emitting cluster gas of Cygnus A*
- Clewley L., Jarvis M. J., 2004, *MNRAS*, 352, 909, *The cosmic evolution of low-luminosity radio sources from the Sloan Digital Sky Survey Data Release 1*
- Collister A., et al., 2007, *MNRAS*, 375, 68, *MegaZ-LRG: a photometric redshift catalogue of one million SDSS luminous red galaxies*
- Condon J., Ransom S., 2016, *Essential radio astronomy*. Princeton Series in Modern Observational Astronomy, Princeton University Press, <https://books.google.hr/books?id=vWWYDwAAQBAJ>
- Condon J. J., Cotton W. D., Greisen E. W., Yin Q. F., Perley R. A., Taylor G. B., Broderick J. J., 1998, *AJ*, 115, 1693, *The NRAO VLA Sky Survey*
- Cresci G., Maiolino R., 2018, *Nature Astronomy*, 2, 179, *Observing positive and negative AGN feedback*
- Croton D. J., et al., 2006, *MNRAS*, 365, 11, *The many lives of active galactic nuclei: cooling flows, black holes and the luminosities and colours of galaxies*
- Croton D. J., et al., 2016, *ApJS*, 222, 22, *Semi-Analytic Galaxy Evolution (SAGE): Model Calibration and Basic Results*
- Delvecchio I., et al., 2017, *A&A*, 602, A3, *The VLA-COSMOS 3 GHz Large Project: AGN and host-galaxy properties out to $z \lesssim 6$*
- Donoso E., Best P. N., Kauffmann G., 2009, *MNRAS*, 392, 617, *Evolution of the radio-loud galaxy population*
- Dunlop J. S., Peacock J. A., 1990, *MNRAS*, 247, 19, *The Redshift Cut-Off in the Luminosity Function of Radio Galaxies and Quasars*
- Fabian A. C., 2012, *ARA&A*, 50, 455, *Observational Evidence of Active Galactic Nuclei Feedback*
- Fadda D., et al., 2006, *AJ*, 131, 2859, *The Spitzer Space Telescope Extragalactic First Look Survey: 24 μ m Data Reduction, Catalog, and Source Identification*
- Fanidakis N., et al., 2012, *MNRAS*, 419, 2797, *The evolution of active galactic nuclei across cosmic time: what is downsizing?*
- Felten J. E., 1976, *ApJ*, 207, 700, *On Schmidt's V_m estimator and other estimators of luminosity functions*

- Ferrarese L., Merritt D., 2000, ApJ, 539, L9, *A Fundamental Relation between Supermassive Black Holes and Their Host Galaxies*
- Feruglio C., Maiolino R., Piconcelli E., Menci N., Aussel H., Lamastra A., Fiore F., 2010, A&A, 518, L155, *Quasar feedback revealed by giant molecular outflows*
- Fleuren S., et al., 2012, MNRAS, 423, 2407, *Herschel-ATLAS: VISTA VIKING near-infrared counterparts in the Phase 1 GAMA 9-h data*
- Fotopoulou S., Paltani S., 2018, A&A, 619, A14, *CPz: Classification-aided photometric-redshift estimation*
- Fotopoulou S., et al., 2016, A&A, 587, A142, *The 5-10 keV AGN luminosity function at $0.01 < z < 4.0$*
- Franceschini A., et al., 2006, A&A, 453, 397, *Cosmic evolution of the galaxy's mass and luminosity functions by morphological type from multi-wavelength data in the CDF-South*
- Furlanetto C., et al., 2018, MNRAS, 476, 961, *The second Herschel-ATLAS Data Release - III. Optical and near-infrared counterparts in the North Galactic Plane field*
- Gebhardt K., et al., 2000, ApJ, 539, L13, *A Relationship between Nuclear Black Hole Mass and Galaxy Velocity Dispersion*
- Gehrels N., 1986, ApJ, 303, 336, *Confidence limits for small numbers of events in astrophysical data*
- Giallongo E., Salimbeni S., Menci N., Zamorani G., Fontana A., Dickinson M., Cristiani S., Pozzetti L., 2005, ApJ, 622, 116, *The B-Band Luminosity Function of Red and Blue Galaxies up to $z = 3.5$*
- Gludemans A. J., et al., 2021, A&A, 656, A137, *Low frequency radio properties of the $z > 5$ quasar population*
- Gofford J., et al., 2014, ApJ, 784, 77, *Revealing the Location and Structure of the Accretion Disk Wind in PDS 456*
- Graham A. W., Onken C. A., Athanassoula E., Combes F., 2011, MNRAS, 412, 2211, *An expanded M_{bh} - σ diagram, and a new calibration of active galactic nuclei masses*
- Griffiths D., 2017, *Introduction to electrodynamics*. Cambridge University Press, <https://books.google.hr/books?id=Kh4xDwAAQBAJ>
- Gruppioni C., et al., 2013, MNRAS, 432, 23, *The Herschel PEP/HerMES luminosity function - I. Probing the evolution of PACS selected Galaxies to $z \approx 4$*
- Hardcastle M. J., Evans D. A., Croston J. H., 2007, MNRAS, 376, 1849, *Hot and cold gas accretion and feedback in radio-loud active galaxies*
- Harrison C. M., 2017, Nature Astronomy, 1, 0165, *Impact of supermassive black hole growth on star formation*
- Harrison C. M., Alexander D. M., Mullaney J. R., Swinbank A. M., 2014, MNRAS, 441, 3306, *Kiloparsec-scale outflows are prevalent among luminous AGN: outflows and feedback in the context of the overall AGN population*
- Harrison C. M., Costa T., Tadhunter C. N., Flütsch A., Kakkad D., Perna M., Vietri G., 2018, Nature Astronomy, 2, 198, *AGN outflows and feedback twenty years on*
- Heckman T. M., Best P. N., 2014, ARA&A, 52, 589, *The Coevolution of Galaxies and Supermassive Black Holes: Insights from Surveys of the Contemporary Universe*
- Higson E., Handley W., Hobson M., Lasenby A., 2019, Statistics and Computing, 29, 891, *Dynamic nested sampling: an improved algorithm for parameter estimation and evidence calculation*
- Hirschmann M., Somerville R. S., Naab T., Burkert A., 2012, MNRAS, 426, 237, *Origin of the antihierarchical growth of black holes*
- Hopkins A. M., 2004, ApJ, 615, 209, *On the Evolution of Star-forming Galaxies*
- Husemann B., Harrison C. M., 2018, Nature Astronomy, 2, 196, *Reality and myths of AGN feedback*
- Ilbert O., et al., 2006, A&A, 457, 841, *Accurate photometric redshifts for the CFHT legacy survey calibrated using the VIMOS VLT deep survey*
- Intema H. T., van der Tol S., Cotton W. D., Cohen A. S., van Bemmell I. M., Röttgering H. J. A., 2009, A&A, 501, 1185, *Ionospheric calibration of low frequency radio interferometric observations using the peeling scheme. I. Method description and first results*
- Intema H. T., Jagannathan P., Mooley K. P., Frail D. A., 2017, A&A, 598, A78, *The GMRT 150 MHz all-sky radio survey. First alternative data release TGSS ADR1*

- Iverson R. J., et al., 2007, MNRAS, 380, 199, *The SCUBA Half Degree Extragalactic Survey - III. Identification of radio and mid-infrared counterparts to submillimetre galaxies*
- Jarvis M. J., et al., 2013, MNRAS, 428, 1281, *The VISTA Deep Extragalactic Observations (VIDEO) survey*
- Johnston R., 2011a, A&A Rev., 19, 41, *Shedding light on the galaxy luminosity function*
- Johnston R., 2011b, A&A Rev., 19, 41, *Shedding light on the galaxy luminosity function*
- Kass R. E., Raftery A. E., 1995, Journal of the American Statistical Association, 90, 773, *Bayes factors*
- Kauffmann G., et al., 2003, MNRAS, 341, 54, *The dependence of star formation history and internal structure on stellar mass for 10^5 low-redshift galaxies*
- Kelly B. C., Fan X., Vestergaard M., 2008, ApJ, 682, 874, *A Flexible Method of Estimating Luminosity Functions*
- Kim S., et al., 2012, ApJ, 756, 28, *SPITZER-IRAC Identification of HERSCHEL-ATLAS SPIRE Sources*
- Kolokythas K., O'Sullivan E., Giacintucci S., Raychaudhury S., Ishwara-Chandra C. H., Worrall D. M., Birkinshaw M., 2015, MNRAS, 450, 1732, *New insights into the evolution of the FR I radio galaxy 3C 270 (NGC 4261) from VLA and GMRT radio observations*
- Kormendy J., Ho L. C., 2013, ARA&A, 51, 511, *Coevolution (Or Not) of Supermassive Black Holes and Host Galaxies*
- Lacy M., Rawlings S., Hill G. J., Bunker A. J., Ridgway S. E., Stern D., 1999, MNRAS, 308, 1096, *Optical spectroscopy of two overlapping, flux-density-limited samples of radio sources in the North Ecliptic Cap, selected at 38 and 151MHz*
- Laigle C., et al., 2016, ApJS, 224, 24, *The COSMOS2015 Catalog: Exploring the $1 < z < 6$ Universe with Half a Million Galaxies*
- Liddle A. R., 2007, MNRAS, 377, L74, *Information criteria for astrophysical model selection*
- Lilly S. J., Carollo C. M., Pipino A., Renzini A., Peng Y., 2013, ApJ, 772, 119, *Gas Regulation of Galaxies: The Evolution of the Cosmic Specific Star Formation Rate, the Metallicity-Mass-Star-formation Rate Relation, and the Stellar Content of Halos*
- Liu G., Zakamska N. L., Greene J. E., Nesvadba N. P. H., Liu X., 2013, MNRAS, 436, 2576, *Observations of feedback from radio-quiet quasars - II. Kinematics of ionized gas nebulae*
- Loredo T. J., 2004, in Fischer R., Preuss R., Toussaint U. V., eds, American Institute of Physics Conference Series Vol. 735, Bayesian Inference and Maximum Entropy Methods in Science and Engineering: 24th International Workshop on Bayesian Inference and Maximum Entropy Methods in Science and Engineering. pp 195–206 (arXiv:astro-ph/0409387), doi:10.1063/1.1835214
- Magorrian J., et al., 1998, AJ, 115, 2285, *The Demography of Massive Dark Objects in Galaxy Centers*
- Mainieri V., et al., 2008, ApJS, 179, 95, *The VLA Survey of the Chandra Deep Field-South. II. Identification and Host Galaxy Properties of Submillijansky Sources*
- Maiolino R., et al., 2017, Nature, 544, 202, *Star formation inside a galactic outflow*
- Marshall H. L., 1985, ApJ, 299, 109, *The evolution of optically selected quasars with Z less than 2.2 and B less than 20*
- Marshall H. L., Tananbaum H., Avni Y., Zamorani G., 1983, ApJ, 269, 35, *Analysis of complete quasar samples to obtain parameters of luminosity and evolution functions*
- Martín-Navarro I., Brodie J. P., Romanowsky A. J., Ruiz-Lara T., van de Ven G., 2018, Nature, 553, 307, *Black-hole-regulated star formation in massive galaxies*
- Mauch T., Sadler E. M., 2007, MNRAS, 375, 931, *Radio sources in the 6dFGS: local luminosity functions at 1.4 GHz for star-forming galaxies and radio-loud AGN*
- McAlpine K., Jarvis M. J., 2011, MNRAS, 413, 1054, *The evolution of radio sources in the UKIDSS-DXS-XMM-LSS field*
- McAlpine K., Smith D. J. B., Jarvis M. J., Bonfield D. G., Fleuren S., 2012, MNRAS, 423, 132, *The likelihood ratio as a tool for radio continuum surveys with Square Kilometre Array precursor telescopes*
- McAlpine K., Jarvis M. J., Bonfield D. G., 2013, MNRAS, 436, 1084, *Evolution of faint radio sources in the VIDEO-XMM3 field*

- McConnell N. J., Ma C.-P., 2013, *ApJ*, 764, 184, *Revisiting the Scaling Relations of Black Hole Masses and Host Galaxy Properties*
- McCourt M., O’Leary R. M., Madigan A.-M., Quataert E., 2015, *MNRAS*, 449, 2, *Magnetized gas clouds can survive acceleration by a hot wind*
- McNamara B. R., Nulsen P. E. J., 2007, *ARA&A*, 45, 117, *Heating Hot Atmospheres with Active Galactic Nuclei*
- Miller N. A., et al., 2013, *ApJS*, 205, 13, *The Very Large Array 1.4 GHz Survey of the Extended Chandra Deep Field South: Second Data Release*
- Mohan N., Rafferty D., 2015, *PyBDSF: Python Blob Detection and Source Finder*, Astrophysics Source Code Library (ascl:1502.007)
- Morganti R., 2017, *Nature Astronomy*, 1, 596, *Archaeology of active galaxies across the electromagnetic spectrum*
- Narayan R., Mahadevan R., Grindlay J. E., Popham R. G., Gammie C., 1998, *ApJ*, 492, 554, *Advection-dominated accretion model of Sagittarius A*: evidence for a black hole at the Galactic center.*
- Nawaz M. A., Wagner A. Y., Bicknell G. V., Sutherland R. S., McNamara B. R., 2014, *MNRAS*, 444, 1600, *Jet-intracluster medium interaction in Hydra A - I. Estimates of jet velocity from inner knots*
- Nesvadba N. P. H., Lehnert M. D., De Breuck C., Gilbert A. M., van Breugel W., 2008, *A&A*, 491, 407, *Evidence for powerful AGN winds at high redshift: dynamics of galactic outflows in radio galaxies during the “Quasar Era”*
- Netzer H., 2015, *ARA&A*, 53, 365, *Revisiting the Unified Model of Active Galactic Nuclei*
- Novak M., et al., 2017, *A&A*, 602, A5, *The VLA-COSMOS 3 GHz Large Project: Cosmic star formation history since $z = 5$*
- Novak M., Smolčić V., Schinnerer E., Zamorani G., Delvecchio I., Bondi M., Delhaize J., 2018, *A&A*, 614, A47, *Constraints on submicrojansky radio number counts based on evolving VLA-COSMOS luminosity functions*
- Ocran E. F., Taylor A. R., Vaccari M., Ishwara-Chandra C. H., Prandoni I., Prescott M., Mancuso C., 2021, *MNRAS*, 500, 4685, *The evolution of the low-frequency radio AGN population to $z = 1.5$ in the ELAIS N1 field*
- Padovani P., Bonzini M., Kellermann K. I., Miller N., Mainieri V., Tozzi P., 2015, *MNRAS*, 452, 1263, *Radio-faint AGN: a tale of two populations*
- Padovani P., et al., 2017, *A&A Rev.*, 25, 2, *Active galactic nuclei: what’s in a name?*
- Page M. J., Carrera F. J., 2000, *MNRAS*, 311, 433, *An improved method of constructing binned luminosity functions*
- Pracy M. B., et al., 2016, *MNRAS*, 460, 2, *GAMA/WiggleZ: the 1.4 GHz radio luminosity functions of high- and low-excitation radio galaxies and their redshift evolution to $z = 0.75$*
- Rafferty D. A., McNamara B. R., Nulsen P. E. J., Wise M. W., 2006, *ApJ*, 652, 216, *The Feedback-regulated Growth of Black Holes and Bulges through Gas Accretion and Starbursts in Cluster Central Dominant Galaxies*
- Rawlings S., Eales S., Lacy M., 2001, *MNRAS*, 322, 523, *A sample of 6C radio sources with virtually complete redshifts - II. Optical spectroscopy*
- Richings A. J., Faucher-Giguère C.-A., 2018, *MNRAS*, 474, 3673, *The origin of fast molecular outflows in quasars: molecule formation in AGN-driven galactic winds*
- Rigby E. E., Argyle J., Best P. N., Rosario D., Röttgering H. J. A., 2015, *A&A*, 581, A96, *Cosmic downsizing of powerful radio galaxies to low radio luminosities*
- Rose M., Tadhunter C., Ramos Almeida C., Rodríguez Zaurín J., Santoro F., Spence R., 2018, *MNRAS*, 474, 128, *Quantifying the AGN-driven outflows in ULIRGs (QUADROS) - I: VLT/Xshooter observations of nine nearby objects*
- de Ruiter H. R., Willis A. G., Arp H. C., 1977, *A&AS*, 28, 211, *A Westerbork 1415 MHz survey of background radio sources. II. Optical identifications with deep IIIa-J plates.*
- Rupke D. S. N., Gültekin K., Veilleux S., 2017, *ApJ*, 850, 40, *Quasar-mode Feedback in Nearby Type 1 Quasars: Ubiquitous Kiloparsec-scale Outflows and Correlations with Black Hole Properties*
- Rybicki G., Lightman A., 2008, *Radiative processes in astrophysics*. Physics textbook, Wiley, <https://books.google.hr/books?id=eswe2StAspsC>

- Sadler E. M., et al., 2002, MNRAS, 329, 227, *Radio sources in the 2dF Galaxy Redshift Survey - II. Local radio luminosity functions for AGN and star-forming galaxies at 1.4 GHz*
- Sadler E. M., et al., 2007, MNRAS, 381, 211, *Radio galaxies in the 2SLAQ Luminous Red Galaxy Survey - I. The evolution of low-power radio galaxies to $z \sim 0.7$*
- Sani E., Marconi A., Hunt L. K., Risaliti G., 2011, MNRAS, 413, 1479, *The Spitzer/IRAC view of black hole-bulge scaling relations*
- Saunders W., Rowan-Robinson M., Lawrence A., Efstathiou G., Kaiser N., Ellis R. S., Frenk C. S., 1990, MNRAS, 242, 318, *The 60- μ m and far-infrared luminosity functions of IRAS galaxies.*
- Saxena A., Röttgering H. J. A., Rigby E. E., 2017, MNRAS, 469, 4083, *Modelling the luminosities and sizes of radio sources: radio luminosity function at $z = 6$*
- Schinnerer E., et al., 2004, AJ, 128, 1974, *The VLA-COSMOS Survey. I. Radio Identifications from the Pilot Project*
- Schinnerer E., et al., 2007, ApJS, 172, 46, *The VLA-COSMOS Survey. II. Source Catalog of the Large Project*
- Schinnerer E., et al., 2010, ApJS, 188, 384, *The VLA-COSMOS Survey. IV. Deep Data and Joint Catalog*
- Schmidt M., 1968, ApJ, 151, 393, *Space Distribution and Luminosity Functions of Quasi-Stellar Radio Sources*
- Schmidt M., Green R. F., 1983, ApJ, 269, 352, *Quasar evolution derived from the Palomar bright quasar survey and other complete quasar surveys.*
- Schwarz G., 1978, Annals of Statistics, 6, 461, *Estimating the Dimension of a Model*
- Shakura N. I., Sunyaev R. A., 1973, A&A, 24, 337, *Black holes in binary systems. Observational appearance.*
- Skilling J., 2004, in Fischer R., Preuss R., Toussaint U. V., eds, American Institute of Physics Conference Series Vol. 735, Bayesian Inference and Maximum Entropy Methods in Science and Engineering: 24th International Workshop on Bayesian Inference and Maximum Entropy Methods in Science and Engineering, pp 395–405, doi:10.1063/1.1835238
- Šlaus B., et al., 2020, A&A, 638, A46, *The XXL Survey. XLI. Radio AGN luminosity functions based on the GMRT 610 MHz continuum observations*
- Smith D. J. B., et al., 2011, MNRAS, 416, 857, *Herschel-ATLAS: counterparts from the ultraviolet-near-infrared in the science demonstration phase catalogue*
- Smolčić V., et al., 2009, ApJ, 696, 24, *Cosmic Evolution of Radio Selected Active Galactic Nuclei in the Cosmos Field*
- Smolčić V., et al., 2017a, A&A, 602, A1, *The VLA-COSMOS 3 GHz Large Project: Continuum data and source catalog release*
- Smolčić V., et al., 2017b, A&A, 602, A6, *The VLA-COSMOS 3 GHz Large Project: Cosmic evolution of radio AGN and implications for radio-mode feedback since $z 5$*
- Smolčić V., et al., 2018, A&A, 620, A14, *The XXL Survey. XXIX. GMRT 610 MHz continuum observations*
- Smolčić V., et al., 2017, A&A, 602, A2, *The VLA-COSMOS 3 GHz Large Project: Multiwavelength counterparts and the composition of the faint radio population*
- Speagle J. S., 2020, MNRAS, 493, 3132, *DYNesty: a dynamic nested sampling package for estimating Bayesian posteriors and evidences*
- Strateva I., et al., 2001, AJ, 122, 1861, *Color Separation of Galaxy Types in the Sloan Digital Sky Survey Imaging Data*
- Sutherland W., Saunders W., 1992, MNRAS, 259, 413, *On the likelihood ratio for source identification*
- Tasse C., et al., 2006, A&A, 456, 791, *New results from the low-frequency counterpart of the XMM large scale structure survey*
- Tasse C., Röttgering H. J. A., Best P. N., Cohen A. S., Pierre M., Wilman R., 2007, A&A, 471, 1105, *GMRT observations of the XMM large scale structure survey field*
- Thrane E., Talbot C., 2019, PASA, 36, e010, *An introduction to Bayesian inference in gravitational-wave astronomy: Parameter estimation, model selection, and hierarchical models*
- Tombesi F., Meléndez M., Veilleux S., Reeves J. N., González-Alfonso E., Reynolds C. S., 2015, Nature, 519, 436, *Wind from the black-hole accretion disk driving a molecular outflow in an active galaxy*

- Ueda Y., Akiyama M., Ohta K., Miyaji T., 2003, *ApJ*, 598, 886, *Cosmological Evolution of the Hard X-Ray Active Galactic Nucleus Luminosity Function and the Origin of the Hard X-Ray Background*
- Urry C. M., Padovani P., 1995, *PASP*, 107, 803, *Unified Schemes for Radio-Loud Active Galactic Nuclei*
- Uttley P., Cackett E. M., Fabian A. C., Kara E., Wilkins D. R., 2014, *A&A Rev.*, 22, 72, *X-ray reverberation around accreting black holes*
- Veilleux S., et al., 2013, *ApJ*, 776, 27, *Fast Molecular Outflows in Luminous Galaxy Mergers: Evidence for Quasar Feedback from Herschel*
- Vernstrom T., et al., 2014, *MNRAS*, 440, 2791, *Deep 3 GHz number counts from a P(D) fluctuation analysis*
- Waddington I., Dunlop J. S., Peacock J. A., Windhorst R. A., 2001, *MNRAS*, 328, 882, *The LBDS Hercules sample of mJy radio sources at 1.4 GHz - II. Redshift distribution, radio luminosity function, and the high-redshift cut-off*
- Willott C. J., Rawlings S., Blundell K. M., Lacy M., 1999, *MNRAS*, 309, 1017, *The emission line-radio correlation for radio sources using the 7C Redshift Survey*
- Willott C. J., Rawlings S., Blundell K. M., Lacy M., Eales S. A., 2001, *MNRAS*, 322, 536, *The radio luminosity function from the low-frequency 3CRR, 6CE and 7CRS complete samples*
- Willott C. J., Rawlings S., Jarvis M. J., Blundell K. M., 2003, *MNRAS*, 339, 173, *Near-infrared imaging and the K-z relation for radio galaxies in the 7C Redshift Survey*
- Wilson T., Rohlfs K., Huettemeister S., 2008, *Tools of radio astronomy*. Astronomy and Astrophysics Library, Springer Berlin Heidelberg, <https://books.google.hr/books?id=9KHw6R8rQEMC>
- Wylezalek D., Morganti R., 2018, *Nature Astronomy*, 2, 181, *Questions and challenges of what powers galactic outflows in active galactic nuclei*
- Yuan Z., Wang J., 2013, *Ap&SS*, 345, 305, *A graphical analysis of the systematic error of classical binned methods in constructing luminosity functions*
- Yuan Z., Jarvis M. J., Wang J., 2020, *ApJS*, 248, 1, *A Flexible Method for Estimating Luminosity Functions via Kernel Density Estimation*

Curriculum vitae

Bruno Šlaus was born in Zagreb in 1993., where he attended primary and high school. He enrolled at the Faculty of Science, University of Zagreb, studying physics at the Department of Physics. After finishing the master's thesis and obtaining the title mag. phys., in 2018. he enrolled in the PhD program at the Faculty of Science, University of Zagreb under the mentorship of prof. dr. sc. Vernesa Smolčić. During his PhD he held the position of teaching assistant at the Faculty of Science, contributing to subjects such as General Physics and Galaxies. He attended many conferences and presented his work to both local and international audiences.

Refereed publications

Submitted

1. **B. Šlaus** V. Smolčić , Ž. Ivezić , S. Fotopoulou, C. J. Willott, P. Pendo , submitted to *A&A*, *The XXL survey LII : The evolution of radio AGN luminosity function determined via parametric methods from GMRT, ATCA, VLA and Cambridge interferometer observations*.

Published

1. V. Smolčić , H. Intema, **B. Šlaus**, S. Raychaudhury, M. Novak, C. Horellou, L. Chiappetti, J. Delhaize, M. Birkinshaw, M. Bondi, M. Bremer, P. Ciliegi, C. Ferrari, K. Kolokythas, C. Lidman, S. L. McGee, R. Norris, M. Pierre, H. Röttgering, C. Tasse, W. Williams, 2018, *A&A*, 620, A14, (XXL Paper XXIX), *The XXL Survey. XXIX. GMRT 610 MHz continuum observations*,
2. **B. Šlaus**, V. Smolčić , M. Novak, S. Fotopoulou, P. Ciliegi, N. Jurlin, L. Ceraj, K. Tisanić, M. Birkinshaw, M. Bremer, L. Chiappetti, C. Horellou, M. Huynh, H. Intema, K. Kolokythas, M. Pierre, S. Raychaudhury, H. Rottgering, 2020, *A&A*, 638, A46, (XXL Paper XLI), *The XXL Survey. XLI. Radio AGN luminosity functions based on the GMRT 610 MHz continuum observations*,